Dissertation submitted in fulfillment of the requirements for the degree

Master of Science in Engineering

Department of Mechanical Engineering

University of Cape Town

MICROSTRUCTURE AND TEXTURE DEVELOPMENT IN AISI430 FERRITIC STAINLESS STEEL

Rabelani Rofhiwa Masindi

13 March 2017

PLAGIARISM DECLARATION

I know the meaning of plagiarism and declare that all the work in the document, save for that which is properly acknowledged, is my own. This thesis/dissertation has been submitted to the Turnitin module (or equivalent similarity and originality checking software) and I confirm that my supervisor has seen my report and any concerns revealed by such have been resolved with my supervisor.

Signature:

Signed by candidate

Date: 13/03/2017

ETHICS FORM

EBE Faculty: Assessment of Ethics in Research Projects

Any person planning to undertake research in the Faculty of Engineering and the Built Environment at the University of Cape Town is required to complete this form before collecting or analysing data. When completed it should be submitted to the supervisor (where applicable) and from there to the Head of Department. If any of the questions below have been answered YES, and the applicant is NOT a fourth year student, the Head should forward this form for approval by the Faculty EIR committee: submit to Ms Zakiya Chikte (Zakiya.chikte@uct.ac.za); New EBE Building, Ph 021 650 5738).
Please note – It is important to keep a signed copy of this form as students must include a copy of the completed form with the dissertation/thesis when it is submitted for examination.

Name of Principal Researcher/Student: Rabelani Masindi **Department:** Mech Eng

If a Student: **Degree:** Msc Eng **Supervisor:** Prof. RD Knutsen

If a Research Contract indicate source of funding/sponsorship:

Research Project Title:

Overview of ethics issues in your research project:

Question 1: Is there a possibility that your research could cause harm to a third party (i.e. a person not involved in your project)?	YES	NO X
Question 2: Is your research making use of human subjects as sources of data? If your answer is YES, please complete Addendum 2.	YES	NO X
Question 3: Does your research involve the participation of or provision of services to communities? If your answer is YES, please complete Addendum 3.	YES	NO X
Question 4: If your research is sponsored, is there any potential for conflicts of interest? If your answer is YES, please complete Addendum 4.	YES	NO X

If you have answered YES to any of the above questions, please append a copy of your research proposal, as well as any interview schedules or questionnaires (Addendum 1) and please complete further addenda as appropriate.

I hereby undertake to carry out my research in such a way that

- there is no apparent legal objection to the nature or the method of research; and
- the research will not compromise staff or students or the other responsibilities of the University;
- the stated objective will be achieved, and the findings will have a high degree of validity;
- limitations and alternative interpretations will be considered;
- the findings could be subject to peer review and publicly available; and
- I will comply with the conventions of copyright and avoid any practice that would constitute plagiarism.

Signed by:

	Full name and signature	Date
Principal Researcher/Student:	Rabelani Rofhiwa Masindi	17/02/2016

This application is approved by:

Supervisor (if applicable):	Sarah George	17/02/2016
HOD (or delegated nominee): Final authority for all assessments with NO to all questions and for all undergraduate research.		17/02/2016
Chair : Faculty EIR Committee For applicants other than undergraduate students who have answered YES to any of the above questions.		

ACKNOWLEDGEMENTS

I would like to thank MINTEK and Advanced Metals Initiative for financially supporting this project and the following people:

- My supervisors, Prof.R.D Knutsen and Dr.S.L George for their guidance and support
- Columbus stainless steel for supplying the samples
- UCT Mechanical Engineering workshop team for machining samples
- Tyrone Newins and Chase Hyde for assisting with Gleeble testing
- UCT Electron Microscope Unit team for granting me access to use the Nanosem 230 for EBSD analysis
- Penny Park-Ross and Candice Mias for insuring that the lab is safe and stocked with supplies
- My husband for his patience, motivation and support
- My family and friends for encouragement and prayers

ABSTRACT

AISI 430 ferritic stainless steel (FSS) is the most widely used FSS alloy due to good resistance to stress corrosion cracking. Owing to the chemical composition range, AISI 430 alloys undergo a partial phase transformation of ferrite to austenite when subjected to hot rolling temperatures. Consequently, the alloys consist of ferrite and austenite during processing. The presence of austenite and ferrite influences the microstructure evolution and texture development during hot rolling and subsequent annealing heat treatments.

Two AISI 430 FSS heats of varying austenite volume fraction were used in this study. The two AISI 430 FSS heats were deformed using the first three passes of the Steckel mill hot rolling process. Post deformation heat treatments namely: continuous phase transformation and martensite tempering heat treatments were performed after three successive simulated Steckel mill passes. Microstructure analyses were performed using light microscopy and Electron Backscattered Diffraction (EBSD). The microstructure analyses were performed in order to determine microstructure evolution and texture development during hot deformation and post deformation heat treatments.

The difference in austenite volume fraction in the respective heats A and B has profound influence on the possibilities for microstructure and texture evolution. For the higher austenite volume fraction heat A, the post-deformation path for austenite decomposition can lead to two very different textures in the prior austenite regions. During continuous diffusional transformation from austenite to ferrite the final texture is influenced by expected variant selection as well as growth selection during the prolonged isothermal heat treatment. The result is relatively strong {001}<110> texture and comparably very weak γ-fiber texture. In the case of the martensite tempering process the γ-fiber texture that is inherited from the austenite to martensite diffusionless transformation is maintained in the prior austenite regions. The mode of post-deformation heat treatment does not significantly impact on texture development in heat B where the texture is dominated by recovery and growth in the primary ferrite phase.

TABLE OF CONTENTS

LIST OF FIGURES

LIST OF TABLES

1. INTRODUCTION

AISI 430 ferritic stainless steel (FSS) is the most widely used grade of the ferritic stainless steel alloys due to its combination of good corrosion resistance, attractive mechanical properties and relatively low cost. The type 430 FSS is used in the automobile, architecture and food industries.

FSS alloys develop an undesirable surface corrugation, also known as ridging (roping) during deep drawing and other sheet forming operations. FSS products must often be polished to remove the surface corrugations; this makes the production process expensive. Ridging occurs when there is an inhomogeneous plastic flow during metal forming. This inhomogeneous plastic flow is due to the spatial distribution of the texture components [1], [2], [3].

There are two major fiber textures, α and γ fiber textures [4]. The α-fiber texture is a cold rolling texture whereas the γ-fiber texture is a recrystallization texture [4], [5] . Furthermore, the α-fiber texture has a high Lankford value compared to the γ-fiber texture [5]. Therefore, the development of the γ-fiber texture components during processing promotes good formability while the α-fiber texture components results in poor formability. The most simplistic view of ridging/roping is that during tensile straining along the rolling direction of a material prone to ridging, the regions consisting of the γ-fiber texture components will deform less than average in the thickness direction resulting in the formation of ridges while the regions with α-fiber texture components deform more than average forming the depressions on the sheet surface [6], [7]. The development of these texture components occurs during cold and hot rolling of FSS alloys [2]. Therefore, it is important to investigate microstructure evolution and texture development during the rolling process of FSS alloys to assist in designing thermo-mechanical processes that increase the ridging resistance.

AISI 430 FSS undergoes partial phase transformation of ferrite to austenite during heating to the hot rolling temperatures and consequently two phases exist at hot rolling temperatures. The phase transformation of ferrite to austenite is influenced by the content of the austenite stabilizing elements such as N, Ni and C. AISI 430 FSS with relatively high contents of these

alloying elements will have a high-volume fraction of austenite during the hot rolling process and vice versa. Hot rolling of the two phases and the subsequent transformations during cooling will thus influence the microstructure evolution and texture development. Of course, the precise nature of microstructure and texture development is highly sensitive to thermo-mechanical process conditions and the total process history. Nevertheless, the commonly reported Kurdjumov-Sachs (K-S) relationship provides for a fixed set of orientations relative to the parent austenite because of austenite decomposition during post-deformation cooling. Consequently, if one assumes a consistent deformation state after a specified hot rolling sequence, then the manner and extent to which the parent austenite decomposes during subsequent cooling, and the evolution of the K-S orientations, will largely influence the resultant texture in the steel.

The ferritic microstructure in AISI430 can be developed in two principal ways after hot rolling: (1) continuous phase transformation during the austenite decomposition to ferrite by diffusion-controlled nucleation and growth, or (2) by tempering martensite which forms during rapid austenite to martensite transformation because of fast cooling from the austenite (or two-phase austenite and ferrite) condition. Since the K-S orientation relationship applies to both forms of austenite decomposition, the transformation textures in each case ((1) and (2) above) should be similar, except that it is anticipated that some variant selection will occur during the austenite to martensite transformation as a result of the influence of elastic and plastic deformation arising from the change in volume and shear associated with the martensite transformation [8]. However, the above assumes that only factors of nucleation influence transformation texture. By virtue of the rolling process, the deformed austenite may or may not recrystallise prior to decomposition depending on the post-deformation cooling conditions, and more particularly in the case of the austenite to ferrite transformation, the rate at which the transformation will occur during cooling. In the case of the austenite to martensite transformation, the rapid cooling might mean that the martensite often forms from deformed austenite. In addition to the influence of the state of the parent austenite, the austenite to ferrite transformation temperature and the transformation time could influence the selective growth of orientation components and hence influence the final transformation texture [8]. Although the same growth selection does not apply in the case of the austenite to martensite transformation, selective growth might occur during

the tempering reactions depending on the tempering conditions, i.e. temperature and duration. In summary, it may be argued that post-deformation thermal conditions (or heat treatments) may significantly influence the texture in the ferritic steel.

The purpose of this study is to determine:

1. The effect of post-deformation heat treatment (continuous cooling, and quench and temper processes) on the microstructure and texture evolution in AISI430 ferritic stainless steel after fixed hot deformation conditions, and

2. The influence of austenite volume fraction at hot rolling temperatures on microstructure and texture evolution under conditions referred to in objective 1 above.

To achieve these objectives, the first three passes of a standard Steckel mill hot rolling process were simulated using the Gleeble 3800 thermomechanical test facility. After simulating the Steckel mill hot rolling process, samples were annealed using two annealing heat treatment protocols. During the first annealing heat treatment, samples were immediately quenched from the third pass hot rolling temperature to the isothermal annealing temperatures of 800˚C or 700˚C and soaked for 15 and 30 minutes. This annealing heat treatment will be referred to continuous phase transformation annealing heat treatment in this study. During this heat treatment, it is expected that austenite will transform to ferrite via the diffusion-controlled nucleation and growth process.

The second post deformation annealing heat treatment was designed such that samples were quenched from the third pass deformation temperature to room temperature and then re-heated to the annealing (or tempering) temperatures of 800˚C or 700˚C followed by soaking for 15, 30 and 60 minutes. During quenching from the deformation temperature to room temperature the austenite transformed to α′-martensite; however, re-heating to the annealing temperature allowed the α′-martensite to transform to ferrite. These two post deformation heat treatments will be used to determine the effect of phase transformation on the microstructure evolution as well as texture development of AISI 430 FSS. The microstructure and texture

characterization was performed using light microscopy and Electron Backscattered Diffraction (EBSD).

Chapter two begins with a review of the metallurgy and processing of AISI 430 FSS, followed by a review on the occurrence of ridging as well as factors that influence ridging resistance. Chapter two also reviews the effect of hot deformation parameters on the microstructure evolution of AISI 430 FSS. The experimental procedure is described in chapter three. Results and discussions are divided into two chapters. Chapter four focuses on the effect of Steckel mill hot rolling parameters on the microstructure evolution and texture development. Chapter five focuses on the microstructure evolution and texture development during the post deformation heat treatments.

2. LITERATURE REVIEW

2.1 Introduction to AISI 430 ferritic stainless steel

AISI 430 is the most widely used ferritic FSS alloy. It has a Cr content of about 16 to 18 wt.% and Ni content of about 0.75 wt.%. FSS alloys are much cheaper than the austenitic stainless steel alloys because of their low Ni content. In addition, FSS alloys can be used to replace the more expensive austenitic stainless steel alloys in mild corrosive environments [9]. The major applications of FSS alloys are in mild corrosive environments such as domestic, catering and atmospheric [9]. These alloys are currently used for kitchenware, architectural and automobile trims [9], [10].

2.2 Metallurgy

FSS are iron based alloys containing from about 12 to 30 wt. % Cr [11]. The Fe-Cr phase diagram illustrated in **Figure 2.1** is a typical phase diagram of FSS alloy with 0.05 wt. % C. This phase diagram indicates that there are four major phase fields, namely: austenite (γ), ferrite (α), α + γ and α + carbides (K_1 or K_2). Alloying elements influence the stability of the phases and the size of the phase fields. For example, increasing the Cr content will increase the ferrite phase field while the austenite phase field is suppressed, owing to Cr being a ferrite stabilizing element. The austenite phase field extends in the temperature range from approximately 820˚C to 1400˚C, and the addition of austenite stabilizing elements, such as C and N, will extend the austenite loop to higher Cr contents, as shown in **Figure 2.1** and **Figure 2.2**, respectively. Between the austenite and ferrite phase fields is a narrow transition region where an alloy will have both ferrite and austenite phases present. This region is referred to as the α + γ two phase field and it occurs at a temperature range from approximately 720˚C and 1400˚C [11]. This phase field will extend to higher Cr contents as the C and N contents increase, as shown in **Figure 2.2**. The minimum temperature of the α + γ two phase region increases from approximately 850˚C to 1000˚C when the C and N content increase from 0.005 to 0.13 %, as shown in **Figure 2.2**.

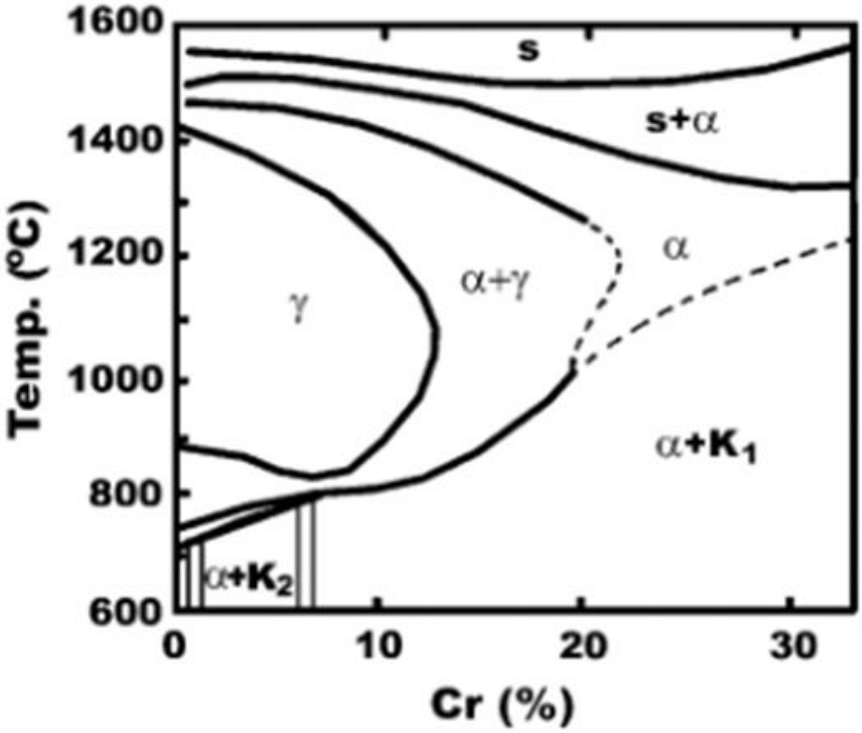

Figure 2.1: Fe-Cr phase diagram for a FSS with 0.05wt% C [12].

The Fe-Cr phase diagram illustrated in **Figure 2.1** indicates that the high temperature microstructure of AISI 430 stainless steel having a Cr content of 16 to 18 wt. % consists of two phases namely, ferrite and austenite. Therefore, during quenching from the two-phase region to room temperature, austenite will transform to α'-martensite. Consequently, the room temperature microstructure will consist of ferrite and α'-martensite, as shown in **Figure 2.3 (a)**. However, it is necessary to temper the martensite to restore the ductility [10]. The final microstructure after tempering generally consists of ferrite and $M_{23}C_6$ carbides as shown in **Figure 2.3 (b)** [13]. In addition, the solubility of C in austenite is higher than that of ferrite; therefore, heat treatment at the two phase α+ γ region will result in enrichment of C in the austenite grains. This promotes the formation of carbides during the tempering heat treatment.

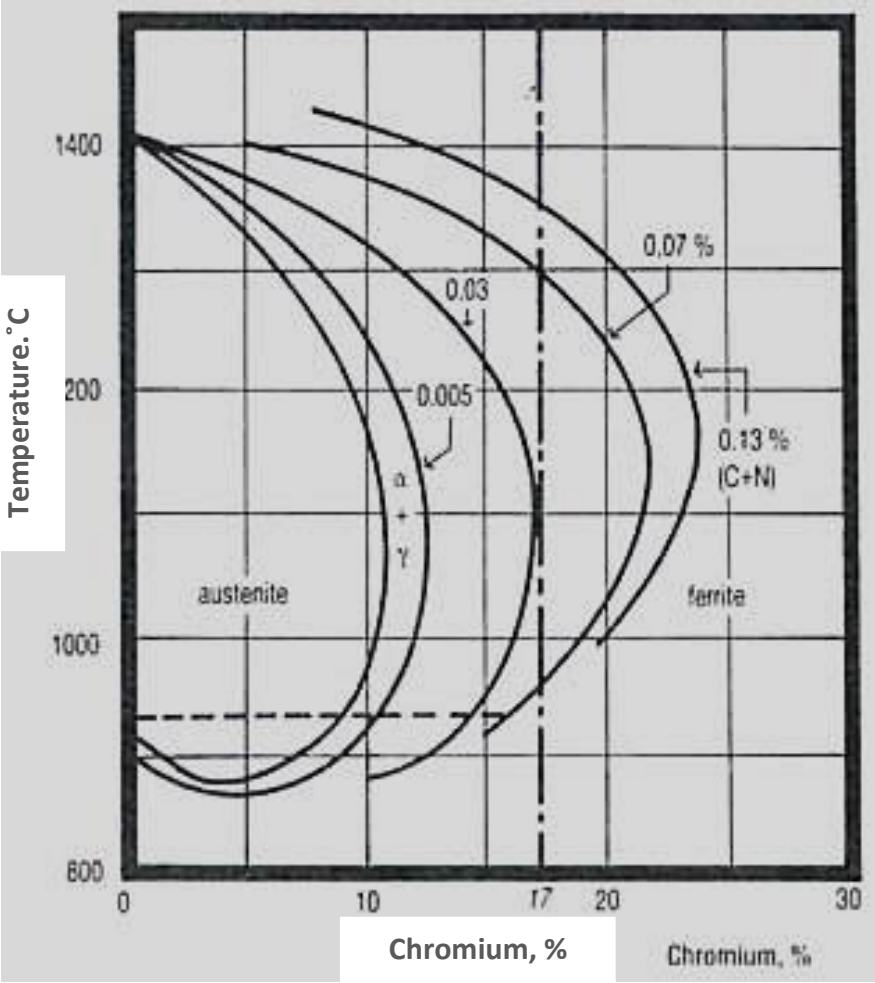

Figure 2.2: Fe-Cr phase diagram illustrating the combined effect of C and N by shifting α+γ phase field to higher Cr contents [10].

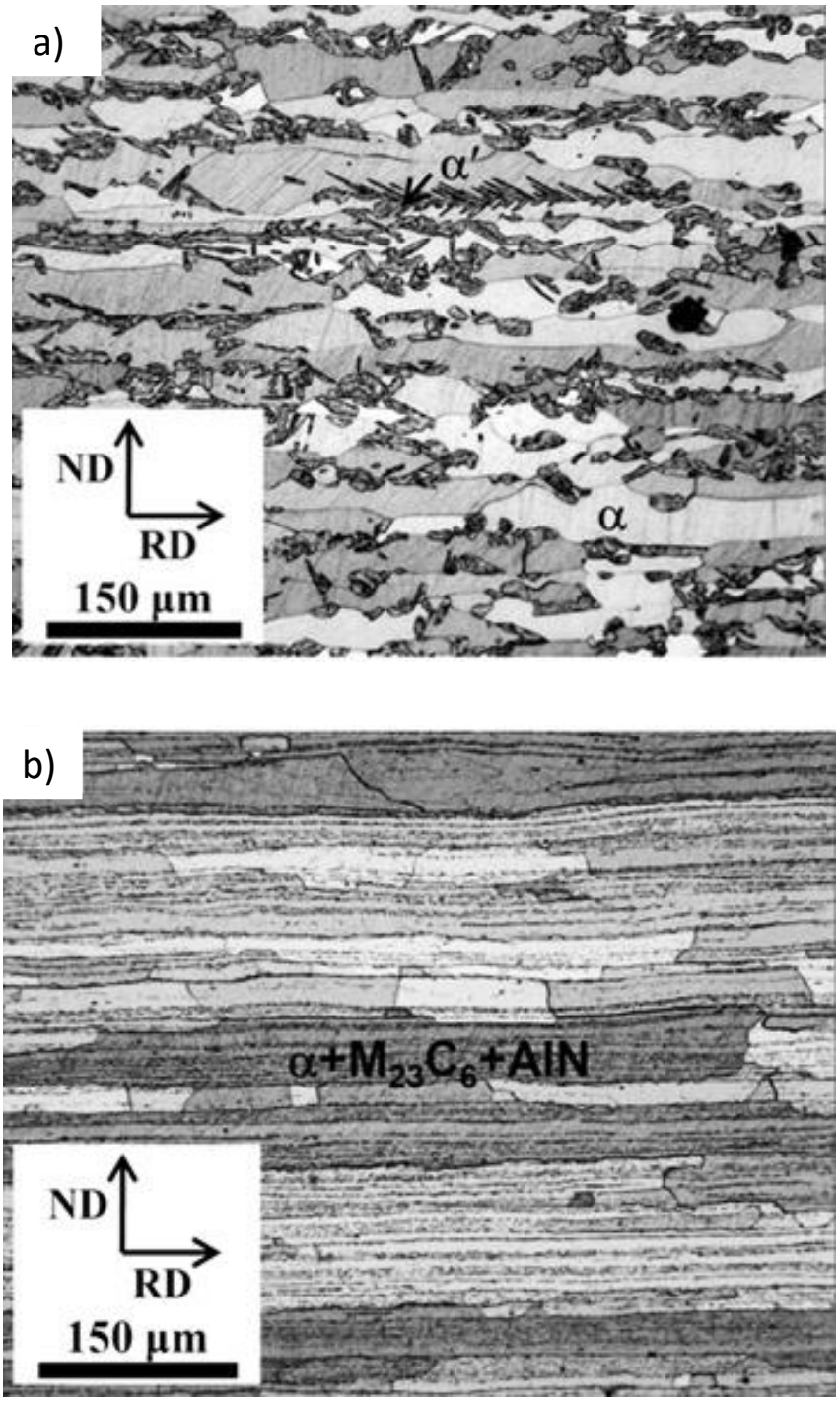

Figure 2.3: Optical micrographs of a hot rolled strip after 5 hours of annealing at 820˚C to obtain homogeneous ferritic microstructure containing precipitates followed by holding at 950˚C for 10 minutes and quenching to room temperature [3]. (a) The optical micrograph shows that the microstructure consists of ferrite and α'-martensite. (b) The optical micrograph shows that the microstructure consists of ferrite, $M_{23}C_6$ carbides and aluminium nitride (AIN) precipitates.

2.3 Processing of ferritic stainless steel

Various processing routes are used to process stainless steel alloys. The major steps of the processing routes include melting of the raw materials, continuous casting, hot rolling, cold rolling, annealing and pickling. An example of a stainless-steel processing route is illustrated in **Figure 2.4**.

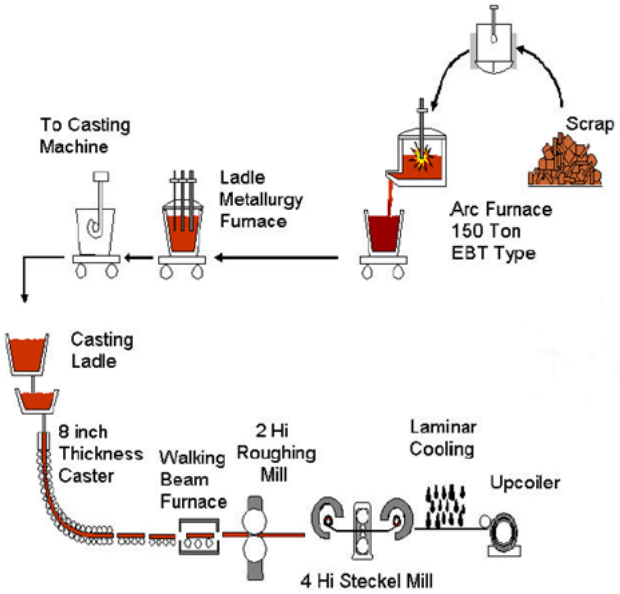

Figure 2.4: Manufacturing processes of stainless steels [14]

Although many processing variations are used, the following is a summary of the major stages used to produce stainless steel sheets. The first stage of processing of stainless steel is melting of the raw materials in an electric arc furnace. The raw materials include elements such as Fe, Cr, Ni and other alloying elements. The content of the alloying elements depends on the desired final mechanical properties of the alloy. The molten metal is further refined using Argon Oxygen Decarburisation (AOD), Vacuum Oxygen Decarburisation (VOD) and a Ladle Refining Furnace (LF). The AOD is the most commonly used refining method in industry [15]. The refined molten metal is then continuously cast into slabs and then cooled. The slab then undergoes surface grinding to remove surface defects. Hot rolling of the slabs is done in two stages, rough rolling and finish rolling. Before the hot rolling process, the slabs are reheated in the furnace to temperatures between 1100˚C and 1300˚C. During the rough rolling stage, the thickness of the slab is reduced

to gauges between 25 and 65mm. During the finishing stage of the hot rolling process the gauge is further reduced. Once the desired gauge is reached, the material can either be coiled or cut into plates. The coil mass is between 20 and 30 tons and the thickness ranges from 3 to 8mm [16]. The hot-rolled coils are then annealed and pickled. Annealing is a heat treatment in which the material is heated and cooled under controlled conditions relieve internal stresses and soften the material. During annealing, a scale develops on the surface of the material. The material is then pickled to remove the scale. The pickling process uses a nitric-hydrofluoric acid bath to descale the material.

The annealed coil is cold rolled using the Z-mill (Sendzimir mill) to produce a smooth and shiny cold rolled stainless steel. The thickness range of the cold rolled material is between 0.02 and 8mm [16]. The cold rolled material is again annealed and pickled before it is processed through the skin pass mill. Alternatively, the cold rolled material can also be processed to a bright anneal finish by annealing in a vertical furnace with an inert atmosphere at a temperature range of 820˚C to 860˚C [9].

2.4 Ridging in ferritic stainless steel

FSS sheet containing 11 to 17 wt. % Cr is known to develop an undesirable surface corrugation known as ridging (roping) when subjected to tension or deep drawing [17], [3], [18], [1], [19]. **Figure 2.5** shows a deep drawn cup of AISI 430 stainless steel with surface corrugations also known as ridging or roping. The occurrence of ridging increases the cost of manufacturing FSS products because the manufacturer must polish the products to remove the surface corrugations shown in **Figure 2.5**.

Figure 2.5: Deep drawn cup of AISI 430 FSS showing surface corrugations [10]

The ridges have a depth in the range of 20 to 50µm [17]. The surface corrugations run parallel to the rolling direction because the constituents required to cause ridging are formed during hot rolling. Ridging is a result of inhomogeneous plastic flow during cold rolling and subsequent sheet forming operations. This inhomogeneous plastic flow is a result of the uneven distribution of texture components. The {111}//ND fiber orientations have higher r-value than the {001}//ND orientated grains. Therefore, during tensile straining along the RD of a material prone to ridging, {111}-orientated regions will deform less than average along the ND and will be related to the ridges on the sheet surface and {001} grains will deform more than average, forming the depressions on the sheet surface [7]. Texture development and distribution is influenced by factors such as alloying elements, as-cast microstructure and processing routes. These factors and their effect on texture and microstructure development will be discussed in the following sections.

2.5 Factors that influence ridging in ferritic stainless steel alloys

2.5.1 Effect of alloying elements

Alloying elements, such as Mo, Ti (strong alpha-stabilizer and carbide former), Al, Si and Nb are ferrite stabilizing elements that promote the formation of ferrite [9]. Austenite stabilizing elements, such as C, N, and Ni promote the formation of austenite at high temperatures and

expand the austenite phase field to higher Cr contents [9] [11]. Consequently, the volume fraction of austenite will increase as the contents of these elements increase. Thermo-Calc calculations of the equilibrium austenite volume fraction in FSS alloys with varying C + N contents in **Figure 2.6** indicate that the volume fraction of austenite is influenced by C and N contents as well as AlN precipitates. In addition, the volume fraction of austenite increases to a maximum at a temperature range of 900˚C to 1000˚C, and then decreases above this temperature range. The dissolution of AlN at approximately 900˚C resulted in a slight increase in the austenite volume fraction at temperatures above 1000˚C, as shown in **Figure 2.6**. During AlN dissolution, the N content increases and this causes the austenite volume fraction to increase. The formation AlN precipitates lowers the peak austenite volume fraction; this is shown in **Figure 2.6** where the elimination of AlN in steel C resulted in an increased austenite volume fraction.

High volume fraction of austenite has been found to increase ridging resistance through the formation of austenite transformation products such as α'-martensite, ferrite and carbides [3]. In addition, the presence of austenite during hot rolling promotes dynamic recrystallization of the ferrite grains [3]. Austenite is harder than ferrite, therefore during hot rolling at the α+γ dual phase temperature, strain partitioning occurs in the ferrite grains. Furthermore, phase transformation of austenite to ferrite promotes the formation of random textures [3] [13]. The presence of α'-martensite during cold rolling promotes the formation of deformation zones in the ferrite phase and this influences the formation of random texture [13].

The austenite stabilizing elements have been found to increase the strength of transformable FSS alloys through increasing the volume fraction of austenite which subsequently transforms to α'-martensite during quenching from high temperature to room temperature [9]. However, ferrite stabilizing elements first decrease the strength through the phase transformation of austenite to ferrite during cooling to single phase ferrite temperature range, and then increase the strength when the microstructure is fully ferritic [9].

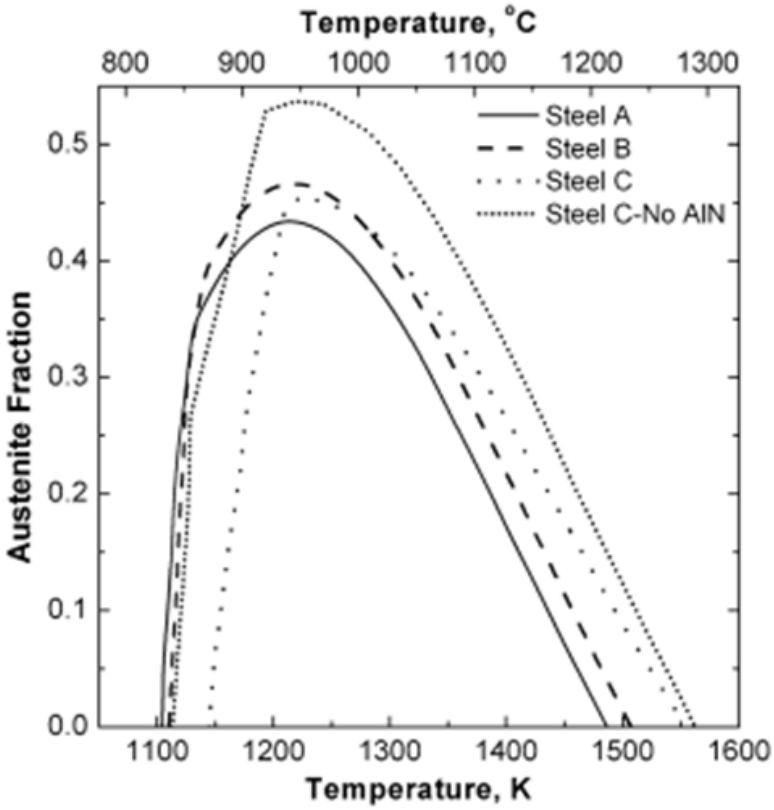

Figure 2.6: Thermo-Calc calculations of the equilibrium austenite fraction. C+N contents of steel A, B, C are 0.063, 0.076 and 0.103 wt. %, respectively [3].

2.5.2 Effect of microstructure and texture on ridging resistance

Continuous casting of FSS results in the formation of columnar grains in the outer regions of the ingots and equiaxed grains at the center of the ingots. The columnar grains are more susceptible to ridging than to the equiaxed grains. The columnar grains have a {001}<uvw> /{001}<110> texture [3] [13] [20], which persists even after numerous processing steps. In addition, grains with {001} <110> are resistant to recrystallisation during the annealing heat treatment [13]. The presence of grain colonies with α-fiber (<111>//RD) texture orientations surrounded by matrix grains with γ-fiber (<111>//ND) results in the inhomogeneous plastic flow during processing and forming of FSS [3] [13] and this influences the occurrence of ridging.

Hamada et al. [13] studied the effect of the initial orientation of the columnar grains on the ridging phenomena in AISI 430 FSS. The study showed that texture development during

processing depends on the initial grain orientation and the processing routes. Annealing of the columnar grains after hot rolling (prior to cold rolling) resulted in the formation of grain colonies with {001} <110> and {112} <110> orientations and severe ridging [13]. However, specimens without annealing prior to cold rolling exhibited random textures and high resistance to ridging [13]. When quenched to room temperature after hot deformation, austenite transformed to α'-martensite Therefore, the presence of hard α'-martensite during cold rolling will promote the development of random textures through the formation of deformation zones in the ferrite grains. Shin et al. [17] investigated the effect of texture on ridging of ferritic stainless. The study showed that the columnar grains resulted in severe ridging when compared to the equiaxed grains. The major textures associated with the columnar grains were ND// {111} and RD//<110>. This resulted in macroscopic plastic anisotropy during deformation.

2.5.3 Effect of processing routes on ridging resistance

The elimination of annealing heat treatment prior to cold rolling has been found to increase the ridging resistance, in the case of transformable FSS [3] [13]. **Figure 2.7** illustrates the profilometry results of three FSS alloys after two different processing routes. The first route comprised of hot rolling, cold rolling and annealing (HCA), while in the second route the alloys were annealed prior to cold rolling (HACA). The profilometry results indicate that the HCA process results in an increased ridging resistance, as shown by the low ridging heights (R_t) in **Figure 2.7**. The microstructure of the HACA processed samples consisted of a homogeneous ferrite matrix with embedded $M_{23}C_6$ precipitates before cold rolling, whereas the HCA route had a banded microstructure consisting of untransformed ferrite and α'-martensite [3]. Therefore, the presence of hard α'-martensite during cold rolling and subsequent recrystallization annealing heat treatment influenced microstructure and texture development and consequently increased ridging resistance.

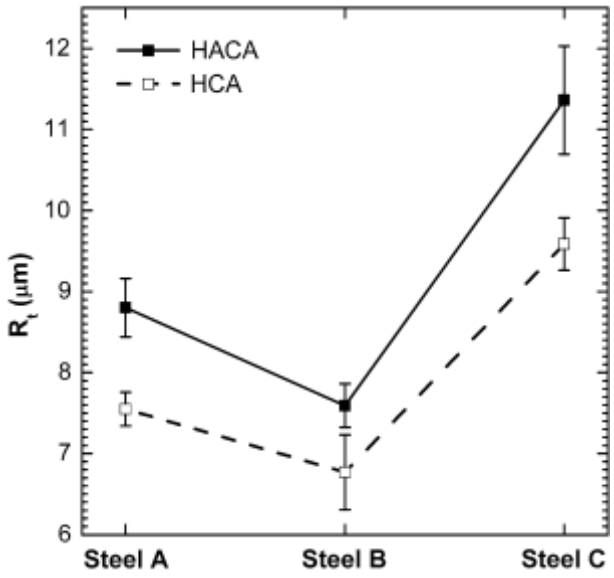

Figure 2.7: Ridging heights (R_t) as measured by profilometry, in the transverse direction of tensile specimens prestrained 15% along the RD. The error bars denote the standard deviation [3].

Table 2.1: Chemical compositions of the FSS alloys studied in **Figure 2.7** (mass percent)

Element	C+N	Cr	Al	Fe	C/N Atomic Ratio
Steel A	0.063	16	0.003	bal	0.68
Steel B	0.076	16	0.003	bal	1.31
Steel C	0.103	16	0.11	Bal	3.18

Figure 2.7 also indicates that the occurrence of ridging is influenced by chemical compositions of the alloys. The compositions of the three alloys used in **Figure 2.7** are shown in **Table 2.1**. **Figure 2.7** shows that steel C with the highest C, N and Al contents has a low ridging resistance compared steel A and B. This is because the C, N and Al contents in steel C were enough to promote the precipitation of AlN. The precipitation of AIN reduces the austenite volume fraction and this results in a decrease in ridging resistance.

2.6 Textures of ferritic stainless steels

Texture is represented using the following notations {hkl}<uvw> or (hkl)[uvw], where {hkl} is the plane that lies parallel to the rolling plane of the sheet, whereas <uvw> is the direction parallel to the rolling direction. Texture is often represented using pole figures and crystalline orientation distribution functions (CODF or ODF). The texture information contained in the pole figures is incomplete and semi quantitative [21]. Therefore, the ODF is used to solve difficulties associated with pole figures. The ODF describes the occurrence of an orientation in three dimensional Euler space. The Euler space is defined by three angles, φ_1, Φ and φ_2, where φ_1 and φ_2 are rotations about the Z-axis or the normal direction (ND) whereas Φ is the rotation about the X axis or the rolling direction (RD).

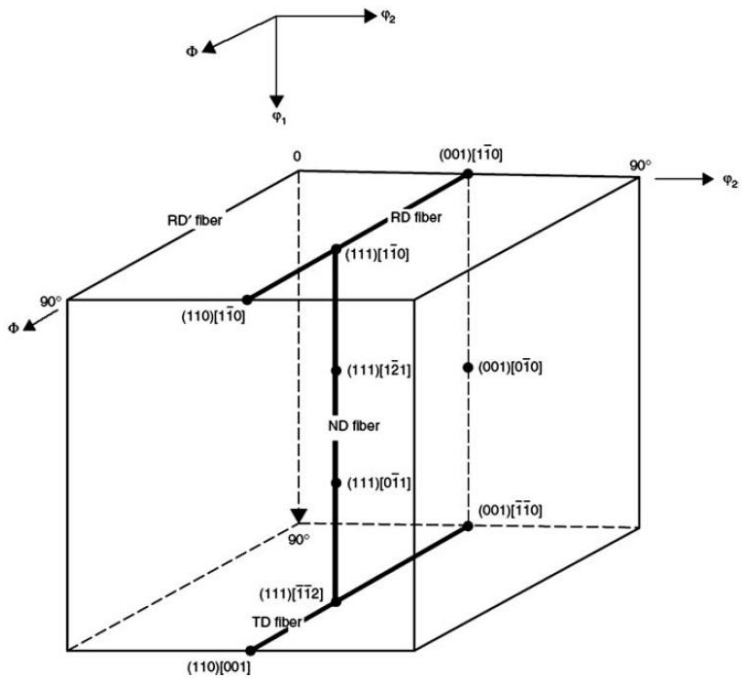

Figure 2.8: Three-dimensional view of Euler space. The horizontal H lying in the φ_2 = 45˚ is shown in bold. This cross-section is of importance in the processing of steels [22].

Figure 2.8 illustrates a three-dimensional view of the Euler space where the φ_2 cross-section, which is important in processing of steels, is shown in bold. **Figure 2.9** shows the φ_2= 45˚section which is used for texture representation in FSS alloys. The φ_2= 45˚section shows the α (RD) fiber and γ (ND) fiber textures that are the major textures associated with FSS alloys. The α fiber

texture is described by <110>//RD with {001} <110>, {112} <110> and {111} <110> texture components. The γ fiber texture is described by <111>//ND with {111} <110>, and {111} <112> texture components, as shown in **Figure 2.9**. In FSS alloys, <111>//ND fiber or γ-fiber texture is a recrystallization texture component whilst the α fiber is a cold rolling texture. The development of <111>//ND during processing of FSS results in an increased Lankford (r) value and its associated drawability [21]. The <110>//RD fiber texture has a low r-value and consequently, poor drawability with the onset of ridging (roping) during deep drawing of FSS alloys [21].

The transformation of austenite to ferrite and subsequent processing conditions influences the microstructure and texture development. Hot rolling of austenite with a cube texture denoted by {100} <001> at the austenite recrystallization temperature transforms the cube texture to a rotated cube texture in the ferrite grains [21]. However, when austenite is deformed below the recrystallisation temperature the austenite develops a sharp texture containing Bs {110} <112>, Cu {112} <111> and S {123} <634> components, as well as a weaker Goss {110} <001> component [21] [23]. During the phase transformation of austenite to ferrite the Bs {110} <112> will transform into {332} <113>, while the Cu {112} <111> will transform to {113} <110> [21]. During subsequent cold rolling the new {113} <110> transformation texture remains highly stable, as the {332} <113> transformation texture shifts towards {554} <225>, to {111} <112> and finally to {111} <110> orientations [21]. The {111} <112> and {111} <110> orientations of the ND fiber exhibit high Lankford values, therefore the {332} <113> is beneficial among the transformation texture components to achieve good drawability as well as improved strength and toughness in the final cold rolled sheet [21].

Raabe and Ylitalo [23] investigated transformation texture in hot rolled FSS by simulating two hot rolling processes with seven passes. The temperature of the respective hot rolling processes labeled as one and two ranged from 1280˚C to 750˚C and 1080˚C to 770˚C respectively. It was found that the ferrite grains showed a strong {001} <110> texture after both hot rolling processes while the α'-martensite showed {111} <112> and {112} <110> texture components in hot rolling process one and two respectively [23]. The alloy compositions indicate that at a temperature below 1200˚C the alloy will consist of austenite and ferrite, and therefore hot rolling at

temperatures below 1200˚C will result in an increased strain accumulation in the austenite grains. Consequently, during hot rolling process two, there was a high amount of strain in the austenite grains compared to hot rolling process one. This resulted in development of austenite phase with {110} <111> recrystallisation texture which then transformed to α'-martensite with {112} <110> texture component. However, hot rolling above the two-phase region in process one resulted in the development of austenite with {110} <112> texture component which then transformed to α'-martensite with {111} <112> texture component during subsequent cooling to room temperature. Knutsen *et al* [24] also found that hot rolling of FSS with high γ volume fraction influences the development of {112} <111> in the austenite phase.

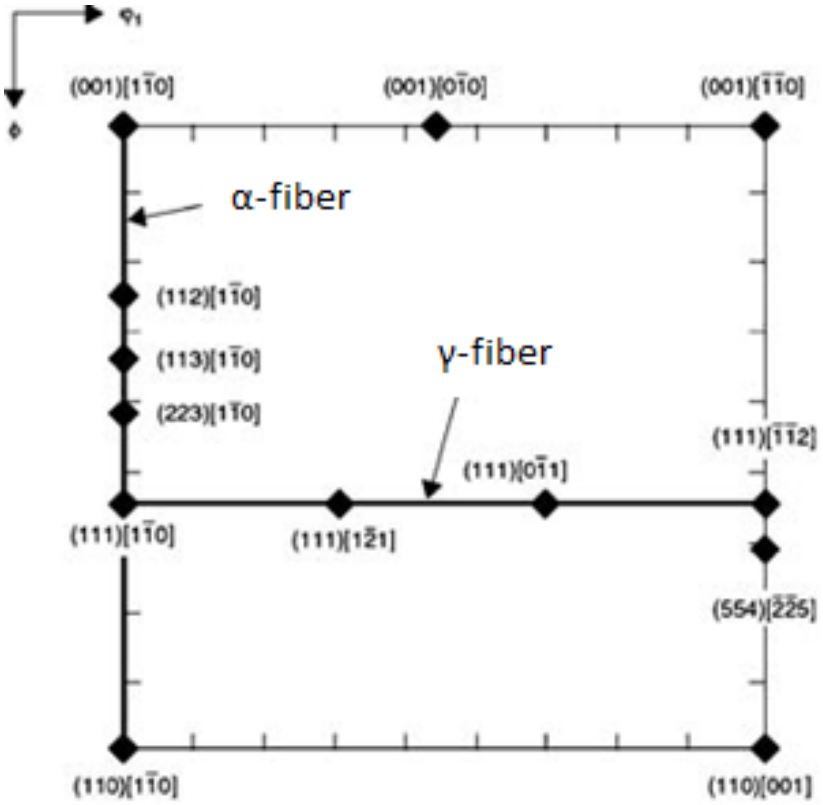

Figure 2.9: Two-dimensional view of $\varphi_2 = 45^{\circ}$crosssection showing the major texture components found in steels [22].

2.7 Variant and growth selection during austenite decomposition

The decomposition of austenite is mostly reported to occur per the Kurdjumov-Sachs (K-S) or Nishiyama-Wassermann (N-W) orientation relationships, but there is very little difference in the

orientation distribution of the product phases for the two relationships [25]. Consequently, this review concentrates mainly on the consideration of the K-S relationship.

The K-S relationship for the transformation of austenite to ferrite or martensite is as follows:

$$\{110\}_{bcc} // \{111\}_{fcc}$$

$$\langle 111\rangle_{bcc} // \langle 110\rangle_{fcc}$$

In effect the above orientation relationship arises from a 90-degree rotation about a <112> axis common to parent and product phases. Given that there are 12 possible <112> directions and the rotation is +/- 90degrees, there are 24 possible variants for the product phase. In their work, Davies *et al* [25] demonstrated that the texture measured in a hot deformed and quenched low carbon steel very closely approximates the predicted texture if the transformation proceeds per the K-S relationship. Notwithstanding the close similarities, the role of variant selection was not considered in their study. Later work has given more attention to variant selection to refine the interpretation of measured textures and the development of models that provide greater accuracy in texture prediction [8], [21]. Da Costa Viana *et al* [26] have demonstrated more specifically that not all 24 variants arising from the K-S orientation dependent transformation of a deformed parent austenite grain are present in the transformation texture. In their model, they assumed that only variants that can nucleate on the 6 or 8 active FCC slip systems are feasible which leads to the definition of up to 12 or 16 possible BCC nucleation variants. They furthermore specified that of the 12 or 16 possible nucleation variants, only those that result in satisfying a transformation work condition can grow. The transformation work condition relates to a requirement that the residual stress in the matrix must be reduced during transformation and hence only those variant nuclei whose growth will translate to positive transformation work will contribute to the transformation texture. The model proposed by da Costa Viana *et al* was evaluated by comparing the predicted transformation texture to the experimental texture of a Nb-microalloyed steel that was quenched after hot deformation. The results showed very close agreement between the measured martensitic texture and the predicted texture arising from the application of the rules described above.

The preceding discussion relates primarily to non-diffusional transformation (i.e. martensitic transformation) and hence does not consider the possibility of competitive growth during the diffusion-dependent austenite to ferrite transformation. Savoie *et al* [27] performed studies which compared transformation texture development from the recrystallized austenite state and the deformed austenite state. Their study included transformation texture simulation using the initial measured austenite texture of deformed and recrystallized Ni-30Co alloy. In this case the texture was simulated without considering variant selection. The experimental texture was obtained from hot rolled Nb-microalloyed steel which could transform to ferrite from recrystallized austenite (hot roll finish at 1020°C) and from deformed austenite (hot roll finish at 870°C). Although the simulated and experimental textures displayed reasonable correlation, the experimental textures were much sharper and marked differences occurred with respect to peak positions along the various fibre traces. In the first instance, for the initial recrystallized austenite state the sharper {100} <011> transformation component in the Nb-microalloyed steel is proposed to be explained by variant selection during transformation from the austenite cube orientations which would of course not be apparent in the simulation that does not consider variant selection. The two other components that derive from the parent cube orientation, namely {110} <110> and {110} <001>, are equally strong for the experimental case (Nb-microalloyed steel) and the simulation and hence variant selection alone cannot explain the differences between the experimental and simulation textures. One would expect the {110} <110> and {110} <001> textures to be relatively sharper in the simulation since they are not competing for selection as is proposed in the experimental case. Hence Savoie *et al* propose that selective growth of certain BCC orientations, such as {100} <011>, into the surrounding non-cube oriented austenite matrix might account for this difference. This is more likely at higher transformation temperatures since increased grain boundary mobility implies higher probability of incoherent growth which in turn means that growth can occur into austenite grains even if there is no simple coincidence (K-S) relationship.

Savoie *et al* present similar arguments for variant selection and selective growth when considering transformation from the deformed austenite state (hot roll finish at 870°C). Of course, there remains some doubt in the analysis since it is assumed that the austenite state for

the experimental condition (Nb-microalloyed steel) is fully recrystallized when finished at 1020°C and fully deformed when finished at 870°C. If partially recrystallized austenite states existed prior to transformation in either of these process steps, then the texture would of course develop differently to the simulations which do make use of fully recrystallized and deformed initial austenite states. However, their arguments are sufficiently strong to support the fact that variant selection and selective growth can play a role in texture evolution during the austenite to ferrite transformation. Similar arguments are also presented in a study involving the role of austenite grain pancaking in a Nb-microalloyed steel where attention is given to the consideration of variant selection and growth selection during austenite to ferrite transformation from the deformed and recrystallized austenite states [28].

2.8 Flow stress

Flow stress is the instantaneous true stress required to continue plastically deforming the material. It is a function of material related parameters i.e. composition, crystal structure, and microstructure and processing conditions i.e. deformation temperature, strain and strain rate [15]. The shape of the flow stress curve indicates the type of restoration mechanism taking place during deformation.

Dynamic recovery and recrystallization are the softening mechanisms that are responsible for softening during hot deformation. From a microstructural point of view, the flow stress curves can be divided into three stages [29]. The first stage is characterized by work hardening and dynamic recovery at low strains. Multiplication of dislocation density, elongation of grains and formation of subgrains within deformed grains occurs at this stage. The multiplication of dislocation makes it more difficult for the dislocations to move across each other, hence the flow stress increases and the material work hardens. The second stage is characterized by a drop in the true stress due to the occurrence of dynamic recrystallization. The third stage of the flow stress curve is characterised by a steady state regime at high strains and the final microstructure becomes equiaxed. When the restoration process is governed by dynamic recrystallisation, the flow stress passes through a peak and then drops to a steady state regime [29], as shown in **Figure 2.10**. The flow stress curve associated with dynamic recrystallization may be a single peak or

multiple peaks depending on the deformation conditions, as shown in **Figure 2.10**. At high strain rates and low temperatures, the flow stress behavior changes from a multiple to a single peak. When the restoration mechanism is governed by dynamic recovery, the flow stress increases to a steady state regime [29].

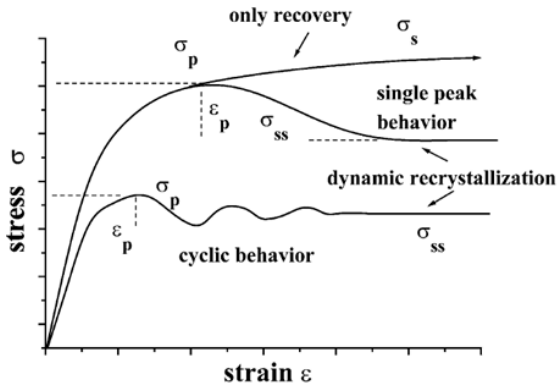

Figure 2.10: Illustration of flow stress behavior at high temperature [29].

2.9 The effect of hot rolling parameters

The Steckel mill rolling process comprises an odd number of passes, usually five, seven or nine roll passes, where the rolling temperature is within the two-phase ferrite-austenite region throughout the rolling process. The strain rates and interpass times increase with each pass. Because of the imposed processing parameters, the microstructural development that occurs because of the deformation affects the final texture distribution and microstructure evolution. The dominant mechanism for microstructural evolution in FSS alloys during this type of thermomechanical processing route is dynamic recovery [30]. The effect of the hot rolling parameters namely, temperature, interpass time, strain and strain rate, is discussed in the following sections.

2.8.1. The effect of strain

Figure 2.11 illustrates the flow stress curve as well as the microstructure evolution of AISI 430 FSS during high temperature deformation. The microstructures in **Figure 2.11 (b) – (e)** show that ferrite grain size decreases with increasing strain. The flow stress curve indicates that the work hardening rate decreases with increasing strain, meaning that softening of the ferrite grains occurs during deformation. The softening mechanism operating under these deformation

conditions is known as continuous dynamic recrystallization [31]. Dynamic recovery is the dominant restoration mechanism in FSS [31]. This is since FSS alloys have high stacking fault energy. The flow stress in **Figure 2.11** resulted from the following deformation conditions: temperature of 1000˚C, strain rate of $0.5s^{-1}$ and maximum strain of 3.0 [31]. Restoration mechanisms depend on the deformation conditions; for example, the microstructures and flow stress curve of AISI 430 FSS in **Figure 2.11** show that continuous dynamic recrystallization is the dominant restoration mechanism at high strains. On the other hand, dynamic recovery was the dominant restoration mechanism at low strains, as shown by the flow stress curves and microstructures in **Figure 2.12** and **Figure 2.13** respectively [30], where there is no decrease in the flow stress value before reaching steady state.

(a)

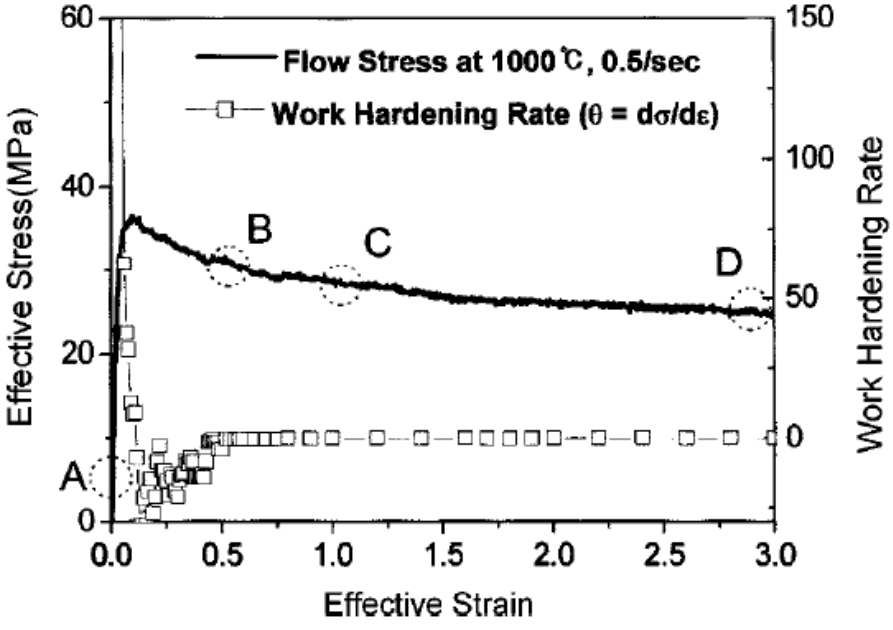

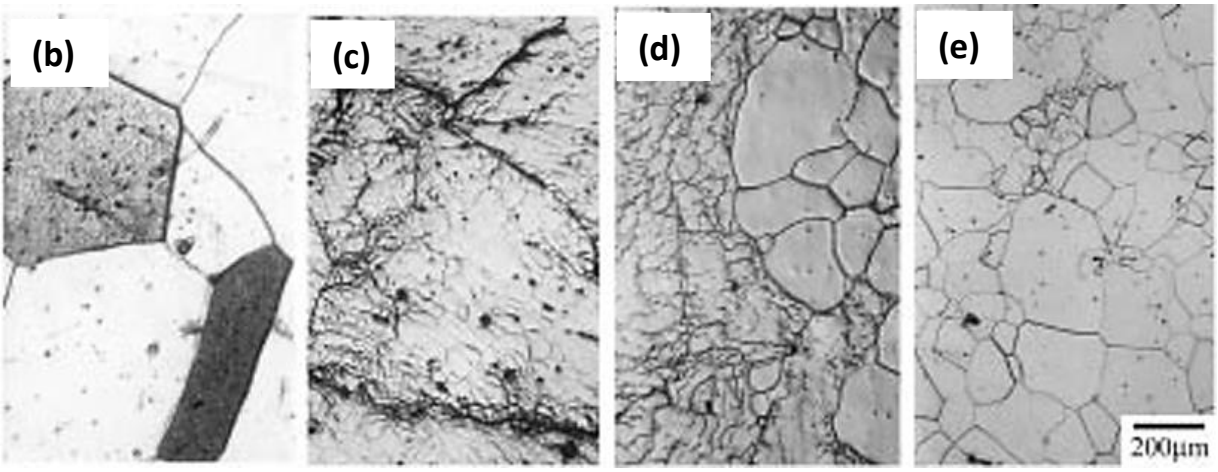

Figure 2.11: a) Flow stress curve and (b), (f) microstructures obtained under various deformation conditions. The microstructure of (b), (c), (d) and (e) were obtained from A (before deformation), B (50% strain), C (100% strain), D (300% strain) in (a), respectively **[31]**.

Figure 2.12 illustrates the flow stress curves for the first two passes of a hot rolling simulation where the deformation conditions were as follows; temperature of 960˚C, strain of 0.6 and 0.5 and the strain rates of $16s^{-1}$ and $22s^{-1}$ respectively [30]. The flow stress curve in **Figure 2.11 (a)** indicates that continuous dynamic recrystallization was taking place during deformation; whilst the flow stress curve in **Figure 2.12** indicates that dynamic recovery occurred during deformation. The difference in these flow stress curves is since the strain rates in **Figure 2.12** are higher than those of **Figure 2.11**. Continuous dynamic recrystallization occurs at strains above 1.5 [32] and at higher strains microstructure evolution is controlled by the deformation conditions. **Figure 2.11 (b)-(e)** illustrates the microstructure evolution of AISI 430 FSS. The micrographs show that the ferrite subgrain size decreases with increasing strain. In addition, the TEM bright field images in **Figure 2.14** indicate that the dislocation density in the ferrite grains increases proportionally with the increase in strain, and the dislocations tangle around the subgrains [31]. Furthermore, subgrains with low angle boundaries are evolved into high angle boundaries. This agrees with the flow stress curve in **Figure 2.11 (a),** which shows that continuous dynamic recrystallization is the dominant restoration mechanism during deformation. **Figure 2.13 (a)** shows the EBSD map of AISI 430 FSS alloy after one high temperature deformation pass. The EBSD map consists of ferrite subgrains with low levels of

misorientation (between 1˚ and 5˚) and martensite bands with high levels of misorientation (>15˚) [30]. The appearance of strain free grains surrounded by highly misorientated grains suggest that there was a static recrystallization event prior to the quench. It has been proposed by Hinton and Beynon [30] that strain free grains have been proposed to nucleate along or close to phase or grain boundaries. The microstructure after two successive high temperature deformations show similar features to that of the first pass; however, after the third successive pass the grain structure is very refined as shown in **Figure 2.13 (C)**.

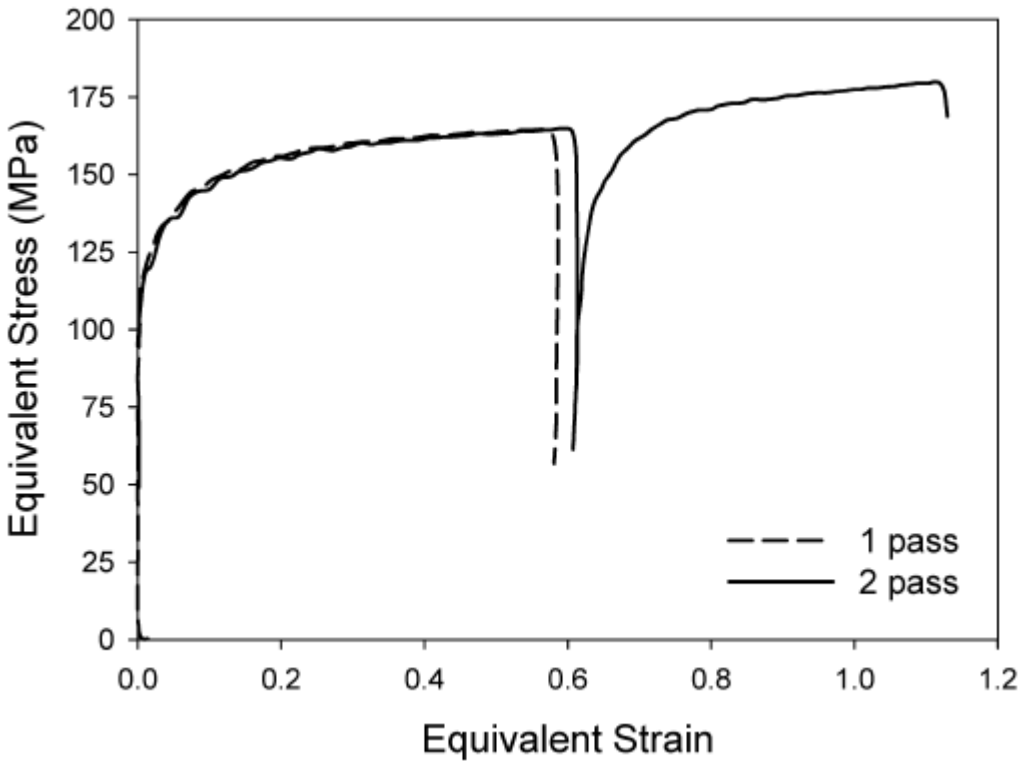

Figure 2.12: Flow stress curves for the first and second passes, carried out at strain rates of $16s^{-1}$ and $22s^{-1}$ at 960˚C. [30].

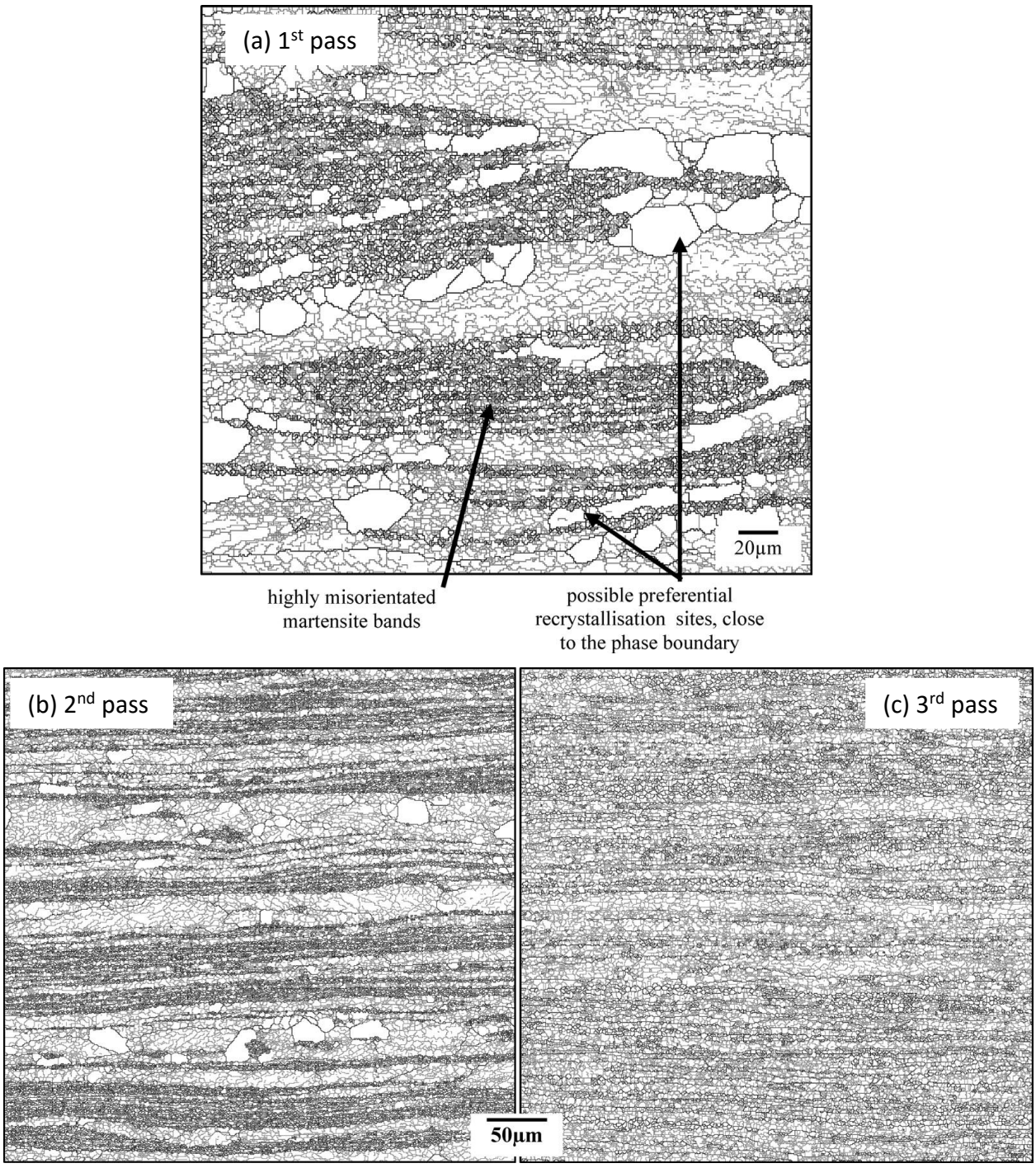

Figure 2.13: EBSD misorientation maps of the first, second and third pass microstructures were black >15˚ and grey >1˚ misorientation [30].

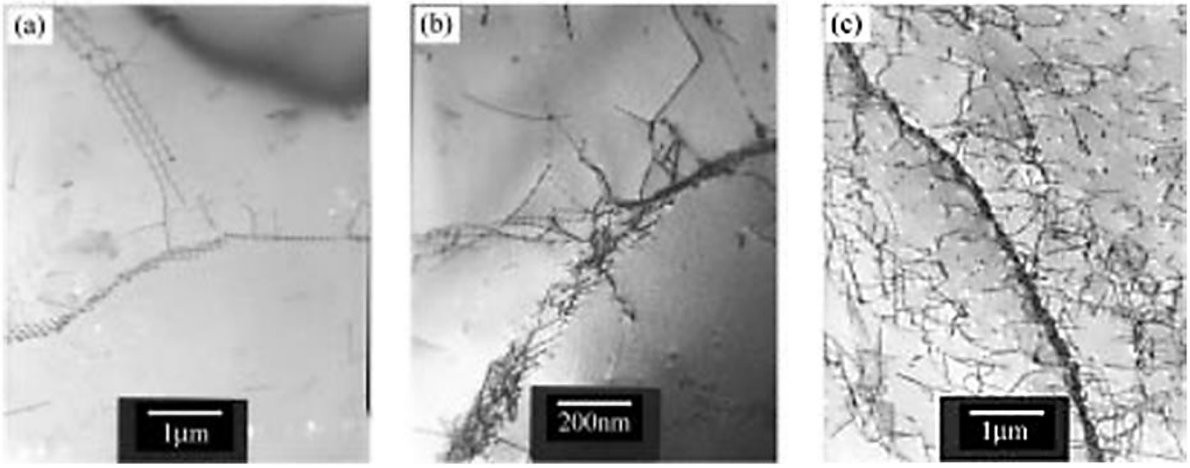

Figure 2.14: TEM bright field images of samples deformed at 1000˚C and $0.5s^{-1}$ under various strains; (a) 10%, (b) 50% and (c) 100% **[31]**

2.8.2. The effect of strain rate and temperature

Deformation temperature and strain rate influence the microstructure and texture evolution of FSS alloys. Hinton and Beynon [30] investigated restoration processes during hot deformation in the ferrite-austenite dual phase region of AISI 430 FSS. The study showed that dynamic recovery was the dominant restoration mechanism when hot deformation occurred at a strain rate greater than $5s^{-1}$. However, the microstructure evolution occurred through continuous dynamic recrystallization when deformed at strain rates of less than $5s^{-1}$. Static recrystallization occurred during the interpass time after deformation at high and low strain rates. Enough stored energy was retained in the deformed ferrite to drive the subsequent static recrystallization [30]. The study by Hinton and Beynon [30]also showed that deformation at low strain rates resulted in a well-defined subgrain structure while microstructures deformed at high strain rate were not well-defined [30]. **Figure 2.15** shows the microstructures of AISI 430 FSS alloy deformed at 0.16^{-1} and $16s^{-1}$ strain rates. The microstructure of the sample deformed at the low strain rates shows a well-defined subgrain structure, as well as a high number of boundaries with misorientation angles of between 5˚ and 12˚, while the high strain rate microstructure shows a high frequency of boundaries with < 5˚ misorientation angles. The high number of boundaries with misorientation angles of between 5˚ and 12˚ indicate that a more continuous restoration process

occurred in the ferrite grains during deformation. The microstructures in **Figure 2.15** showed similar textures.

Mehtonen et al [32] also found that dynamic recovery and continuous dynamic recrystallization were the dominant restoration mechanisms when a stabilized high Cr was deformed at strain rates of greater and less than $1s^{-1}$ respectively. Hot deformation at high strain rate and temperature results in increased flow stress when compared to deformation at low strain rate and temperature. The flow stress increases with increasing strain rate from 0.05 to $0.5s^{-1}$ as shown in **Figure 2.16 (a)** and **(b)**. The flow stress increased up to 75 MPa for a strain rate of 0.5^{-1} as shown in **Figure 2.16 (a)**. The Flow stress increased with decreasing temperature.

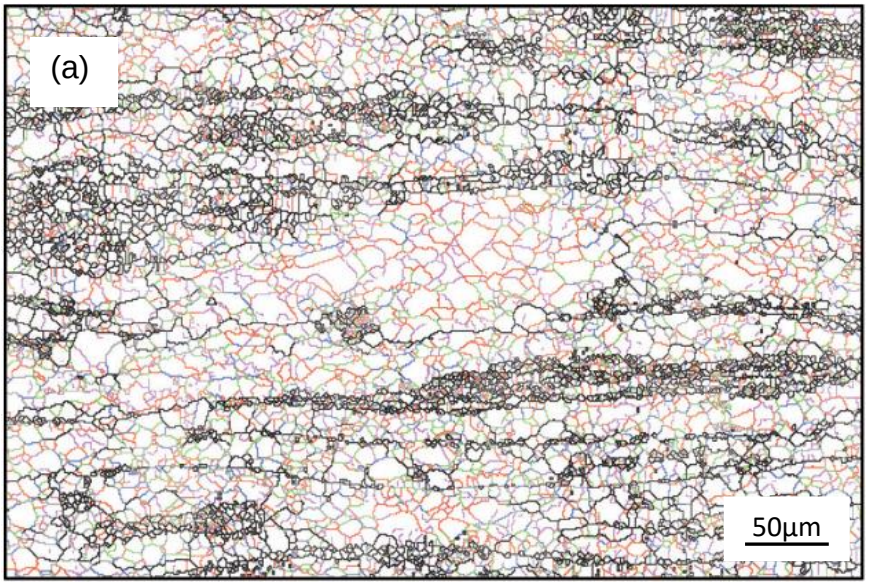

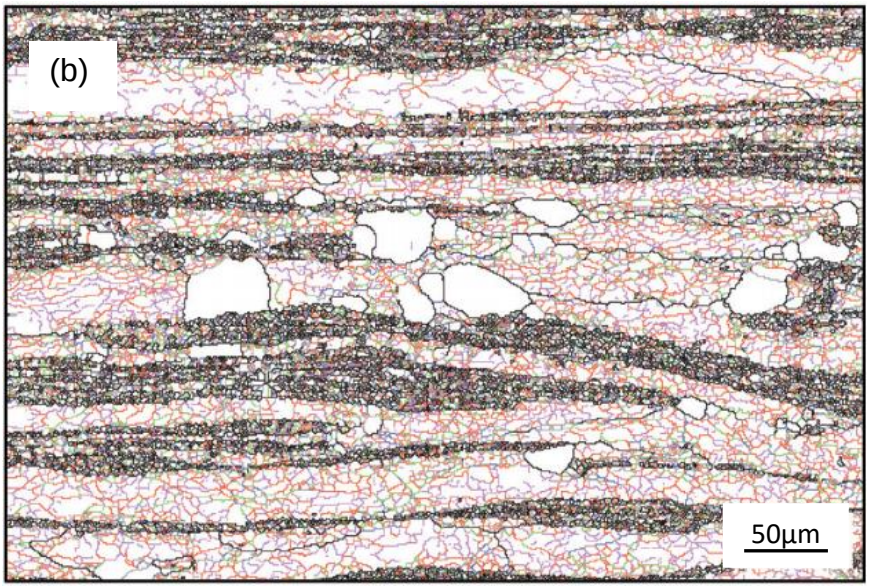

Figure 2.15: EBSD misorientation plots showing the effect of strain rate on the development of the microstructure. Deformation conditions were (a) temperature = 960 ˚C, strain= 0.62, train rate = 0.16s^{-1}, (b) temperature = 960 ˚C, strain = 0.62, strain rate = 16s^{-1} [30].

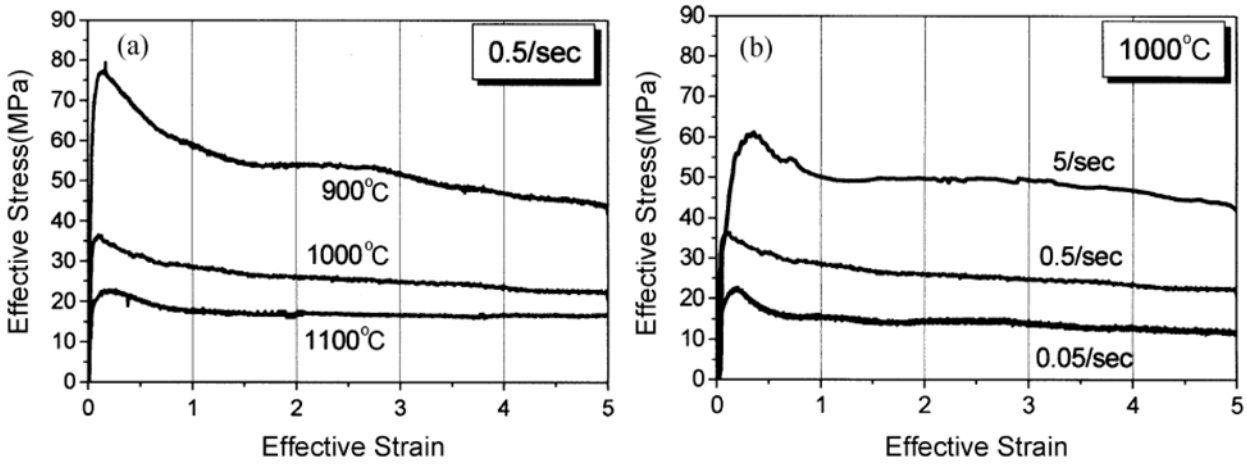

Figure 2.16: Effective stress-strain curves under (a) various temperatures at 0.5s^{-1} and (b) various strain rates at 1000^0C [31].

2.8.3. The effect of inter-pass time

The interpass time is the time between consecutive passes, where restoration can take place. During this time, the material undergoes static restoration mechanisms such as recovery and recrystallisation. The restoration mechanisms will have an impact on the evolution of microstructure and texture during processing.

Figure 2.17 illustrates the microstructure evolution of AISI 430 FSS with increasing interpass times. The microstructures show that static recrystallization was the dominant restoration mechanism during the interpass time. However, after soaking for 10 seconds at the deformation temperature, the microstructure shows coarsening of the deformed ferrite grains. This indicates that increasing the interpass time promotes growth of the ferrite grains. **Figure 2.18** shows the corresponding texture evolution at different interpass times. The $\varphi_2 = 45^\circ$ ODF sections indicate that as the interpass time increases there was very little change in the {001} <110> rotated cube. The {001} <110> texture component remained strong as the interpass time increased from 0 to 10 seconds, as shown in **Figure 2.18**. The $\varphi_2 = 45^\circ$ ODF sections in **Figure 2.18** shows that at the start of interpass time the texture consisted of α and γ fiber textures. However soaking at deformation temperature did not promote the development of the γ fiber texture.

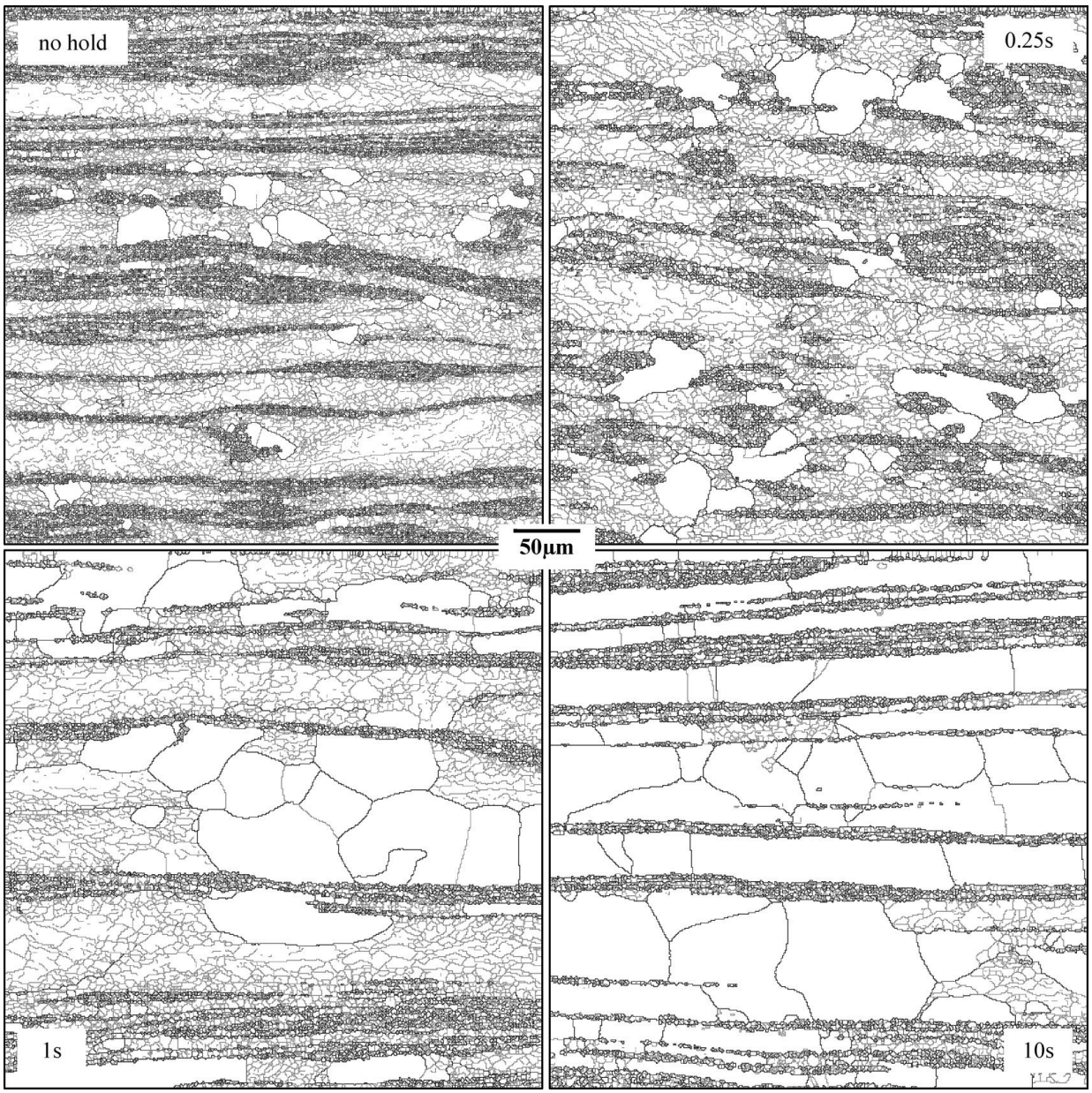

Figure 2.17: EBSD misorientation plots showing the development of microstructures with increasing interpass time, where black > 15˚ and grey >1˚ misorientation [30].

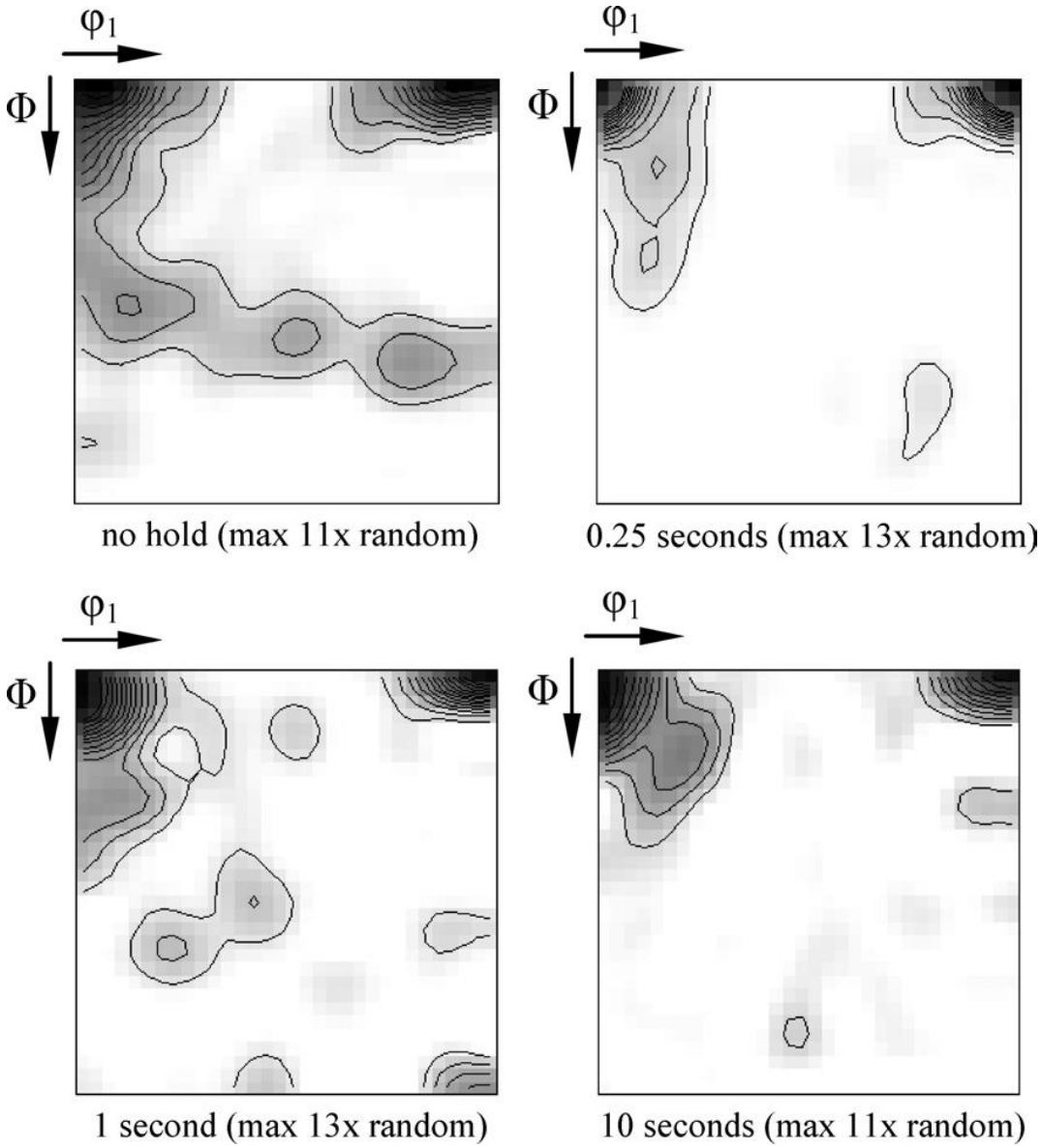

Figure 2.18: $\varphi_2 = 45^\circ$ ODF section showing the evolution of texture during interpass time [30].

3. EXPERIMENTAL PROCEDURE

3.1 Material

Two AISI 430 FSS heats were used for this investigation, heat A and B. The main difference between the two heats is that heat A has high concentration of austenite stabilizing elements, such as carbon nickel and nitrogen, as shown in **Table 3.1**. This means that heat A has a high volume fraction of austenite at high temperature compared to heat B. **Figure 3.1** show the phase diagrams of heat A and B which indicate that the volume fraction of austenite increases with increasing temperature. However, the phase diagrams in **Figure 3.1** indicate that the maximum austenite volume fraction occurs at approximately 960˚C and 940˚C in heat A and B respectively. The volume fraction of α'-martensite is associated with austenite volume fraction because austenite transforms to α'-martensite during rapid cooling to room temperature. This is illustrated in **Figure 3.1** where heat A has high volume fraction of α'-martensite compared to heat B. Transfer bars of heat A and B used in this investigation were supplied by Columbus stainless steels. Testing samples were machined into plane strain compression and tensile test configurations.

Table 3.1: Chemical compositions of heat A and B in weight percent

	Al	C	Cr	Cu	Mn	Mo	Nb	Ni	N	Si	Sn	Ti	V
A	0.01	0.042	16.21	0.06	0.4	0.007	0.01	0.25	0.052	0.4	0.014	0.001	0.1
B	0.009	0.025	16.68	0.07	0.44	0.005	0.002	0.14	0.022	0.43	0.009	0.001	0.12

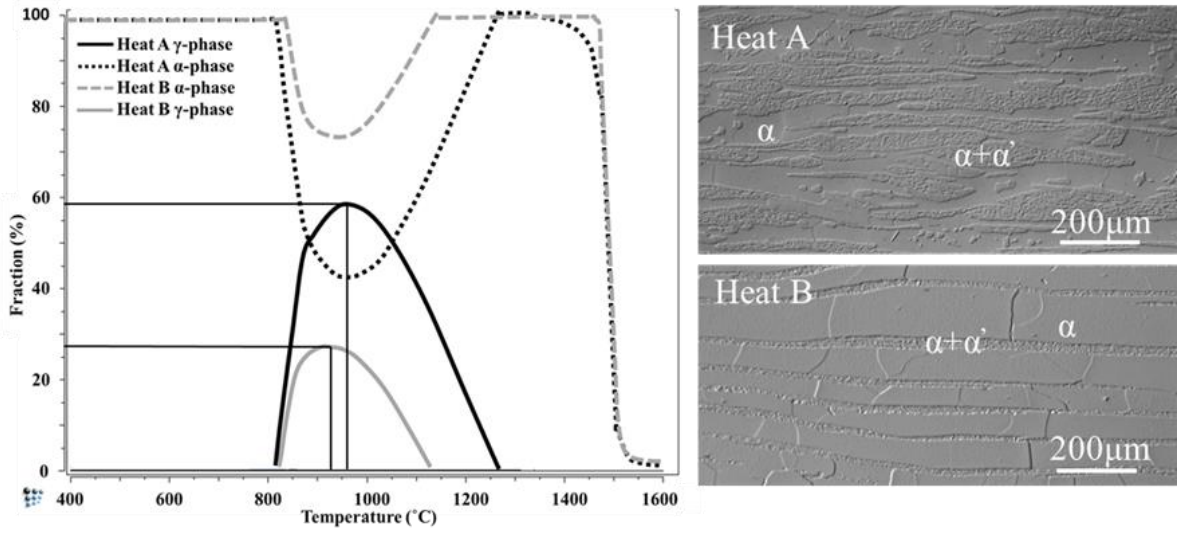

Figure 3.1: Phase diagrams and microstructures of heat A and B

3.2 Plane strain compression testing

Plane strain compression (PSC) testing was performed using the Gleeble 3800 thermomechanical facility. The parameters used during PSC testing were calculated from the Steckel mill logs supplied by Columbus stainless steel. The Steckel mill hot rolling process is comprised of an odd number of passes usually five seven and nine passes. However, for this study up to three passes were performed. This was due to limitations in sample geometry and dimensions. The dimensions of the PSC samples used in this study are as follows: length 30mm, height 20mm and thickness 10mm. After five passes the samples thickness is reduced from 10mm to 2mm. The reduction of thickness from 10mm to 2mm results in damage to the anvils due to welding of the sample onto the anvils. Therefore, the hot rolling parameters of the first three passes of the steckel mill hot rolling process were used for this study. The PSC testing protocol incorporated the pre-deformation heat treatment of the sample, followed by deformations up to three consecutive passes.

3.3.1 Calculation of Steckel mill hot rolling parameters

Table 3.2 shows the parameters obtained from the mill log. These parameters were used to calculate the hot rolling parameters such as strain, strain rate and interpass time (Note that these are average values, refer to appendix)

Table 3.2: Steckel mill hot rolling parameters obtained from the mill log data in appendix

Pass no.	Deformation T (˚C)	Entry h_0 (mm)	Exit h_i (mm)	Roll speed (m/sec)	Arc length (m)	Roll Time (seconds)
1	890	26	19	3.7	0.03	37
2	918	19	14	4.2	0.03	43
3	913	14	10	5.2	0.02	52

a) Temperature

Deformation temperatures were obtained through calculating the average of five temperature values above and below the temperature at the middle of the strip as shown in Table 3.3.

Table 3.3: Temperature values above and below the middle position of the strip

	Temperature (˚C)		
Position	**Pass 1**	**Pass 2**	**Pass 3**
1	893	914	914
2	893	917	914
3	893	917	914
4	893	917	914
5	893	917	914
6 (middle position)	893	917	917
7	892	918	911
8	890	920	911
9	890	920	911
10	887	920	911
11	887	920	911
Average Temperature	891	918	913

b) Strain

The effective nominal strain (ε_n) is calculated according to the following equation [15]:

$$\boldsymbol{\varepsilon_n = \frac{2}{\sqrt{3}} \ln\left(\frac{h_i}{h_0}\right)}$$

Equation 3.1

Where: h_i = input gauge or thickness (mm)

h_o = output gauge or thickness (mm)

c) Strain rate

Figure 3.2 shows that a metal sheet with a thickness of h_0 enters the rolls at the entrance plane XX with a velocity of V_0. The metal sheet passes through the roll gap and exits the plane YY with a reduced thickness h_f at a velocity V_f. The strain rate was calculated using the following equation:

$$\textbf{strain rate} = \frac{\boldsymbol{\varepsilon}}{\mathbf{t}}$$

Equation 3.2

Where: t = time to move through the angle of bite (α), as shown in **Figure 3.2**.

$$t = \frac{v}{L_p}$$

Where: v = roll speed

L_p = projected length of arc of contact, as shown in **Figure 3.2**

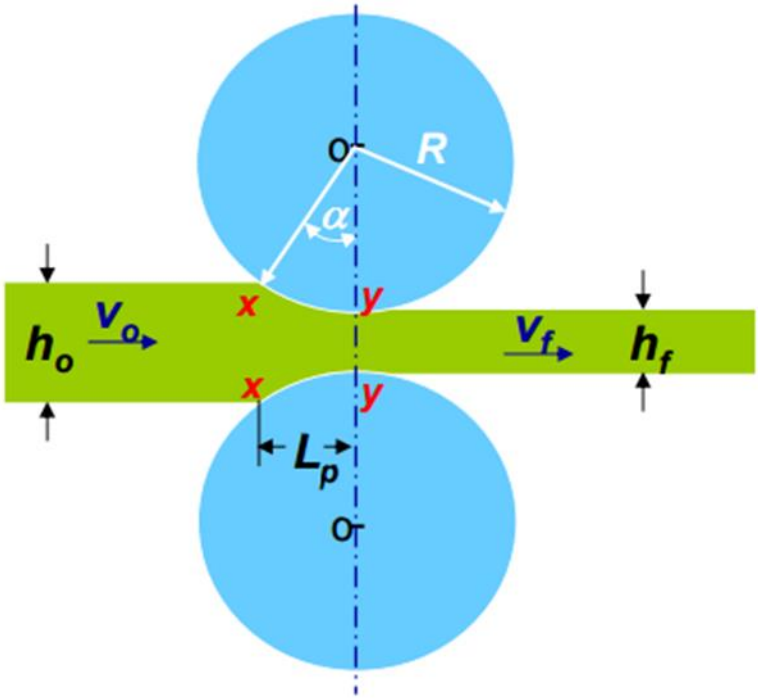

Figure 3.2: Rolling nomenclature.

d) Interpass time

The interpass time represents the restoration time between deformation events in consecutive passes. The roll time given on the mill logs represent the physical roll time of the whole strip. However the material spends about 5 to 7 seconds between the actual passes. This time is not included in the physical roll time. During this time the roll gap is adjusted in preparation for the next pass. The middle section interpass time is then calculated by taking the average of consecutive roll times and adding 6 seconds for the roll gap adjustment [15], as shown in Equation 3.3.

$$interpass\ time = \frac{t_1 + t_2}{2} + 6s$$

Equation 3.3

3.3.2 Pre-deformation heat treatment

A pre-deformation heat treatment was performed in order to increase the austenite volume fraction through the phase transformation of ferrite to austenite. The thermal profile of this

treatment was designed based on both phase information and industrial processing conditions. Firstly, the phase diagrams in **Figure 3.1** indicate that the volume fraction of austenite increases with increasing temperature, as well as that the maximum austenite volume fraction occurs at approximately 960˚C and 940˚C in heat A and B respectively. Secondly, during conventional Steckel mill hot rolling, the material is transferred directly from the rough-rolling mill to the Steckel mill while maintaining the hot rolling temperatures. Therefore, the pre-deformation heat treatment allows the sample to be at the rough-rolling temperatures for a given length of time before being cooled to the equivalent Steckel mill temperatures required for the simulation of thermomechanical processing. The pre-deformation heat treatment was designed such that the sample was heated to 1000˚C and then soaked for 10 minutes. The sample was then cooled to 890˚C, the pass 1 deformation temperature, in 10 minutes and then soaked for 2 minutes prior to deformation. After 2 minutes at 890˚C, the sample was air quenched to room temperature in order to determine the microstructure conditions before deformation.

3.3.3 Plane strain compression protocol

Table 3.4 shows the deformation parameters used to simulate the Steckel mill hot rolling process. The Steckel mill logs supplied by Columbus stainless steel were used to calculate the hot rolling parameters such as temperature, strain, strain rate and inter-pass time. These hot rolling parameters were simulated using plane strain compression tests in order to evaluate the microstructure evolution during industrial hot rolling.

The PSC testing protocol incorporated the pre-deformation heat treatment of the sample, followed by deformations up to three consecutive passes. After each pass the sample was quenched to room temperature in order to study the microstructure development during the hot rolling process. An additional PSC test was performed using the same hot rolling parameters shown in **Table 3.4**, however the strain rate of the 3rd pass was reduced from $80s^{-1}$ to $40s^{-1}$. This test was performed in order to investigate the effect of strain rate on the microstructure evolution as well as the flow stress curves.

Table 3.4: Deformation parameters calculated from the Steckel mill logs

	Temperature (˚C)	Strain	Strain rate (s^{-1})	Inter-pass time (s)
Pass 1	890	0.3	36	46
Pass 2	918	0.3	40	53
Pass 3	913	0.4	100	quench

Test conditions for 1 pass

1. Heat up to 1000˚C in 10 minutes and hold for 10 minutes
2. Cool down to 890˚C (pass deformation temperature) and hold for 2 minutes
3. Deformation event
4. Immediate quench to room temperature

Test conditions for 3 passes

1. Heat up to 1000˚C in 10 minutes and hold for 10 minutes
2. Cool down to 890˚C (pass deformation temperature) and hold for 2 minutes
3. Deformation event
4. Heat up to 918˚C (pass 2 deformation temperature) in 41 seconds and hold for 5 seconds (total inter-pass time of 46 seconds)
5. Deformation event
6. Cool down to 913˚C (pass 3 deformation temperature) in 48 seconds and hold for 5 seconds (total inter-pass time of 53 seconds)
7. Immediate quench to room temperature

3.3 Post deformation annealing heat treatments

The purpose of the post deformation heat treatments was to investigate the effect of phase transformation, austenite volume fraction, temperature and strain rate on the microstructure evolution and texture development of AISI 430 FSS.

Two post deformation heat treatments where performed at 700°C and 800°C. The first post deformation heat treatment was designed such that samples where quenched from the third pass deformation temperature to the annealing temperature of 700°C and 800°C for 15 and 30 minutes. This post deformation heat treatment will be referred to as the continuous phase transformation heat treatment in this study. During the continuous phase transformation heat treatment, the austenite will transform to secondary ferrite.

The second post deformation heat treatment was designed such that samples were quenched from the third pass temperature to room temperature, followed by re heating the sample to the annealing temperature of 700°C and 800°C. The samples were annealed in the salt bath for 15, 30 and 60 minutes. This heat treatment will be referred to as the martensite tempering heat treatment. During the martensite tempering heat treatment, α'-martensite transform to secondary ferrite.

Continuous phase transformation annealing heat treatment

1. Immediate quench to 800˚C or 700˚C after 3rd pass deformation
2. Annealing at 800˚C or 700˚C for 15 and 30 minutes and 1 hour
3. Immediate quench to room temperature

Martensite tempering heat treatment

1. Immediate quench to room temperature after 3rd pass deformation
2. Reheating the deformed specimens to 800˚C or 700˚C
3. Annealing at 800˚C or 700˚C for 15, 30 and 60 minutes
4. Immediate quench to room temperature.

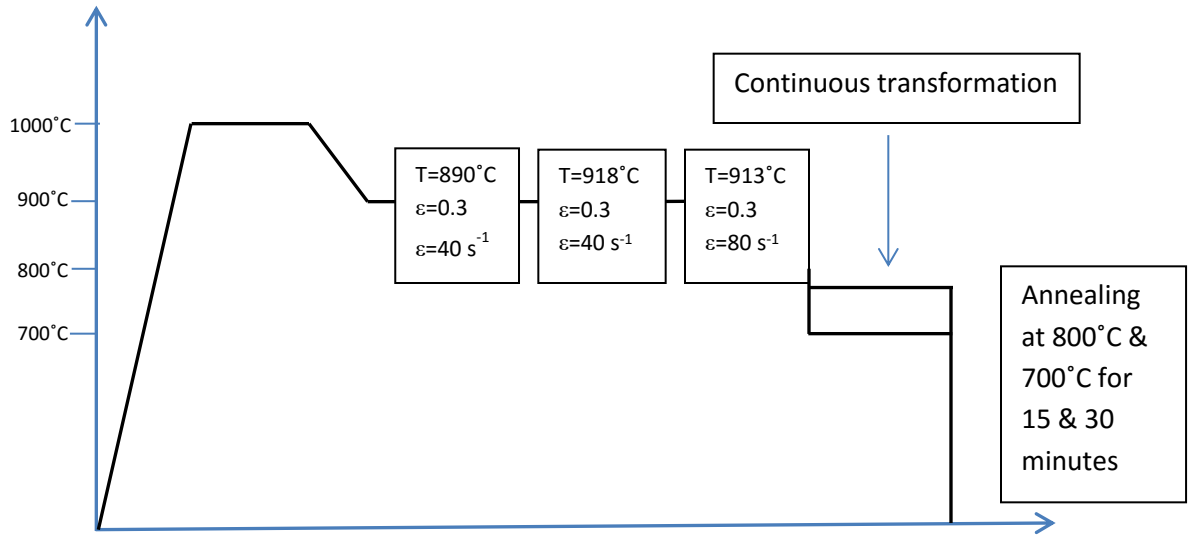

Figure 3.3: PSC testing protocol and continuous phase transformation annealing heat treatment where T, ε and ε (find correct symbol) represent temperature, strain and strain rate respectively.

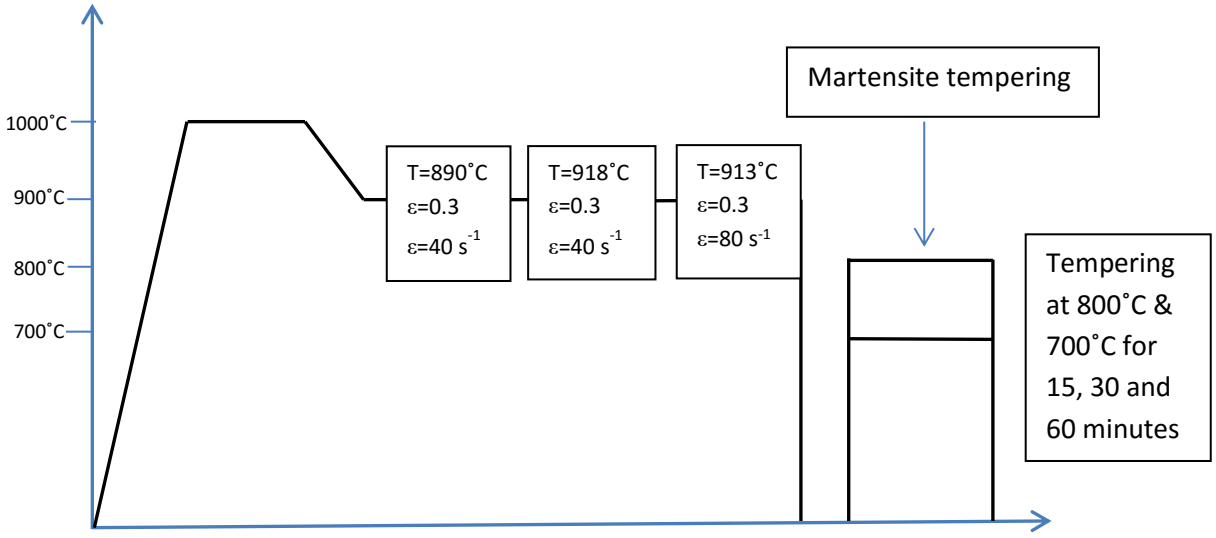

Figure 3.4: PSC testing protocol and martensite tempering heat treatment, where T, ε and ε represent temperature, strain and strain rate respectively.

3.4 Sample preparation for microstructure characterization

3.4.1 Cutting

A Buehler Isomet Low speed saw was used to section 3mm slices from the non-deformed and deformed tensile specimens shown in **Figure 3.5**. The specimens were sectioned perpendicular to the Tension Direction (TD) as shown by the dotted lines in Figure 3.5.

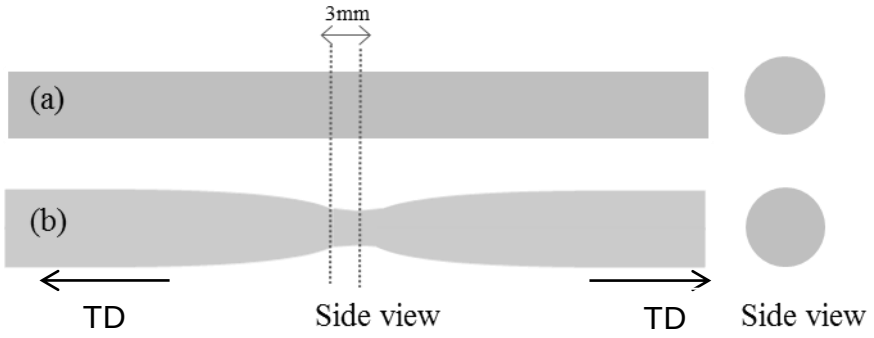

Figure 3.5: Schematics of (a) non-deformed and (b) deformed tensile specimens. The tension direction is indicated by black arrows.

Annealed PSC samples were also cut using Buehler Isomet Low speed saw. Small slices were obtained from the middle of the annealed PSC samples and prepared for microstructure analysis.

Deformed and quenched to room temperature PSC samples were wire cut into 3 mm slices as shown in **Figure 3.6**. The specimens were sectioned parallel to compression direction. The slices were used for microscopic analysis and recrystallization annealing heat treatment protocol 2.

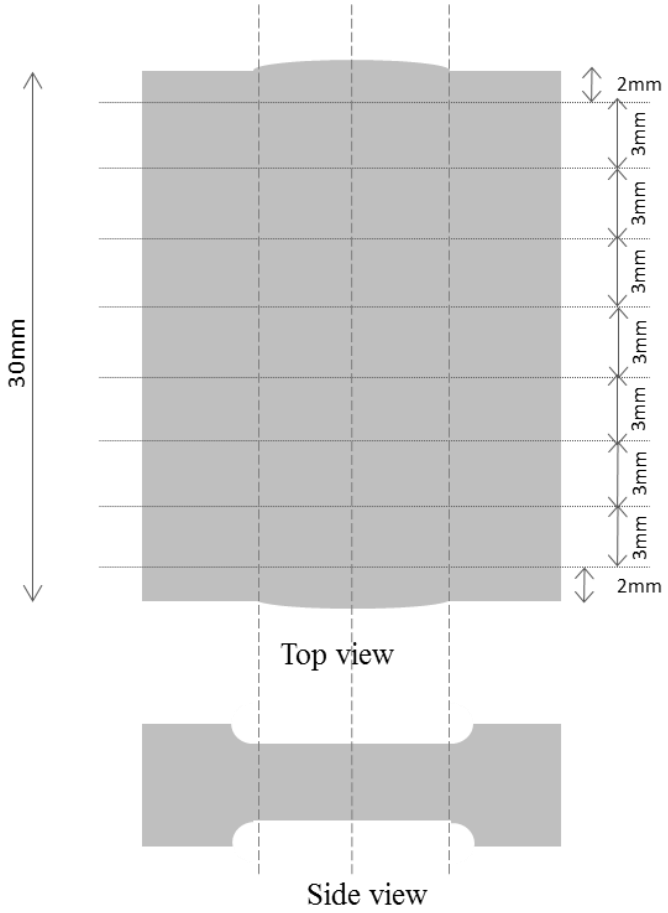

Figure 3.6: Schematic of plane strain compression test specimen.

3.4.2 Hot mounting

Mounting was performed at a 20kN force in the Struers Labopress-3 at 180˚C for 14 minutes (7 minutes heating and 7 minutes cooling) using an acrylic resin.

3.4.3 Polishing

Polishing was performed using the Tegrapol-11 coupled to a Tegradoser-5. The polishing conditions are shown in **Table 3.5**. Silicon carbide paper with 800 grit was used to grind the specimens in order to obtain a flat surface. Specimens were cleaned using ethanol in the ultrasonic bath after the grinding steps. Specimens were also washed with water and ethanol after each polishing step. Warm water was used to wash the specimens after the polishing with colloidal silica. This was done to etch the specimens.

Table 3.5: Polishing protocol

Polishing step	Polishing pad	Lubricant	Time (minutes)
Grinding	800 grit Silicon carbide	Water	2
Grinding	1200 grit Silicon carbide	Water	4
Polishing	MD DAC	3µm	10
Polishing	MD NAP	1µm	5
Polishing	MD CHEM	Colloidal silica (OP-S)	5
Washing	MD CHEM	Warm water	5

3.5 Microstructure and texture characterization

Light microscopy and electron backscattered diffraction (EBSD) were used to characterize the microstructures. Qualitative results obtained from light microscope analysis were used as precursor for the quantitative EBSD analysis.

The EBSD analysis provided information about the phases present in the microstructure as well misorientation angles. EBSD analysis also provided quantitative crystallographic orientation information of the primary ferrite grains, secondary ferrite as well as α'-martensite. The EBSD conditions are shown in **Table 3.6**.

In order to determine texture evolution in the primary ferrite grains of the deformed and annealed samples, Four EBSD maps at the centre of the samples were obtained at 200X and 500 X magnifications and the step size ranged from 0.5 to 2 µm. The four EBSD maps were stitched together and texture analysis was performed using HKL Channel 5 software. The ϕ_2 equal to 45˚ section of the Orientation distribution functions (ODFs) was used to represent the textures, because this section shows α and γ fiber textures which are important in the processing of FSS alloys. Owing to the difficulty in indexing the martensite using the above EBSD mapping conditions, additional EBSD mapping was performed at 2000X magnification using a step size of 0.1µm in order to index the martensite. These EBSD maps were used to determine the texture

evolution in the prior austenite regions. It is important to note that a maximum of two EBSD map was used for texture analysis in the prior austenite regions. This was due to the fact that the prior austenite regions consist of fine grained structure. Therefore a small EBSD map is sufficient for texture analysis in the prior austenite regions.

Table 3.6: EBSD conditions

Voltage	spot size	working distance	magnification	Step size
20KV	3.0 to 4.5	8 and 10mm	200X, 500X, 2000X	0.1 to 2µm

The texture in the prior austenite and primary ferrite regions were determined selectively by creating subsets consisting of primary ferrite or prior austenite regions only, as shown in **Figure 3.7**. **Figure 3.7 (a)** is an EBSD map of the deformed sample obtained at 2000x magnification in order to get a better resolution of the martensite bands. In **Figure 3.7 (a)** the microstructure consists of ferrite bands and martensite bands in the prior austenite regions. Whereas in **Figure 3.7 (b)** the ferrite bands are shown in white color since they are not part of the subset, while the martensite bands are shown in Euler colors. The subset was then used to determine texture in the prior austenite regions. The same procedure was followed when determining texture in the ferrite bands.This process of creating subsets consisting of ferrite or prior austenite bands only made it easier to determine the texture in the in the ferrite and prior austenite bands selectively.

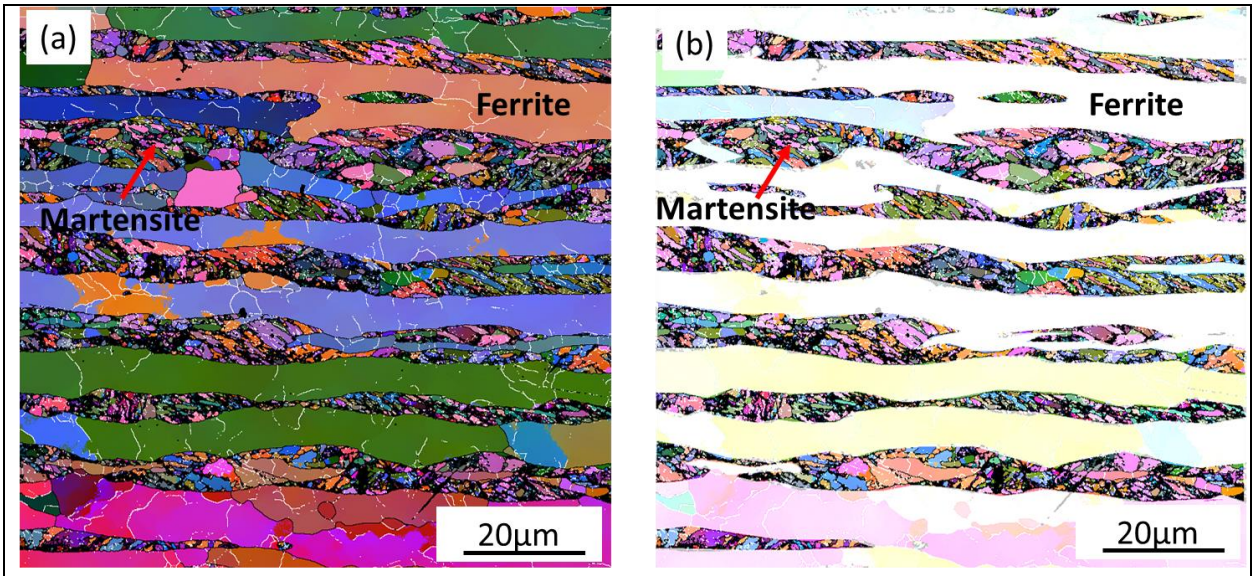

Figure 3.7: An example of subset created in order to selectively determine texture in the prior austenite regions. (a) Before selecting the maertensite bands. (b) After selecting the martensite bands (marteniste band in Euler colors and ferrite bands in white).

4. THE EFFECT OF STECKEL MILL HOT ROLLING PARAMETERS ON THE MICROSTRUCTURE EVOLUTION AND TEXTURE DEVELOPMENT

The results and discussion are divided into two chapters. The first chapter (Chapter 4) focuses on the effect of Steckel mill hot rolling parameters on the microstructure evolution and texture development. The second chapter (Chapter 5) focuses on microstructure evolution and texture development during post deformation heat treatments.

This chapter will focus on the microstructure evolution and texture development during the simulated Steckel mill hot rolling process. The chapter begins by discussing the flow stress data obtained during the simulated Steckel mill hot rolling process. This is followed by a discussion of the microstructure evolution during the pre-deformation heat treatments and during the simulated Steckel mill hot rolling process.

The results and discussion of the texture development during the simulated Steckel mill hot rolling process is divided into four sections where **Sections 4.5.1** and **4.5.2** focus on the texture development in the primary ferrite and prior austenite regions, respectively. The effect of strain rate and austenite volume fraction on the texture development is discussed in **Sections 4.5.3** and **4.5.4**.

4.1 The flow stress curves

The flow stress data was captured during the simulation of the three pass Steckel mill rolling schedule using the Gleeble 3800. **Figure 4.1** illustrates the flow stress curves of heat A and B during the three consecutive passes, using the deformation parameters shown in **Table 3.4**. The flow stress curves of both heats at a strain rate = 40s^{-1} indicate that static recovery occurs between passes which results in rising flow stress at the start of the successive passes (i.e. the yield stress decreases during the interpass period as a result of recovery and possibly recrystallisation. Consequently the flow curves for each pass are discontinuous. The situation is different when the strain rate for pass 3 is increased to 80s^{-1}. In this case there is more or less continuity between pass 2 and pass 3. The expectation is that recovery (and/or recrystallisation)

occur to the same extent during the interpass after pass 2, but that the higher strain rate ($80s^{-1}$) for pass 3 causes a rise in the yield stress which coincidentally is similar to the flow stress at the end of pass 2. The work-hardening rate (particularly for pass 3 at $80s^{-1}$) suggests substantial dynamic softening.

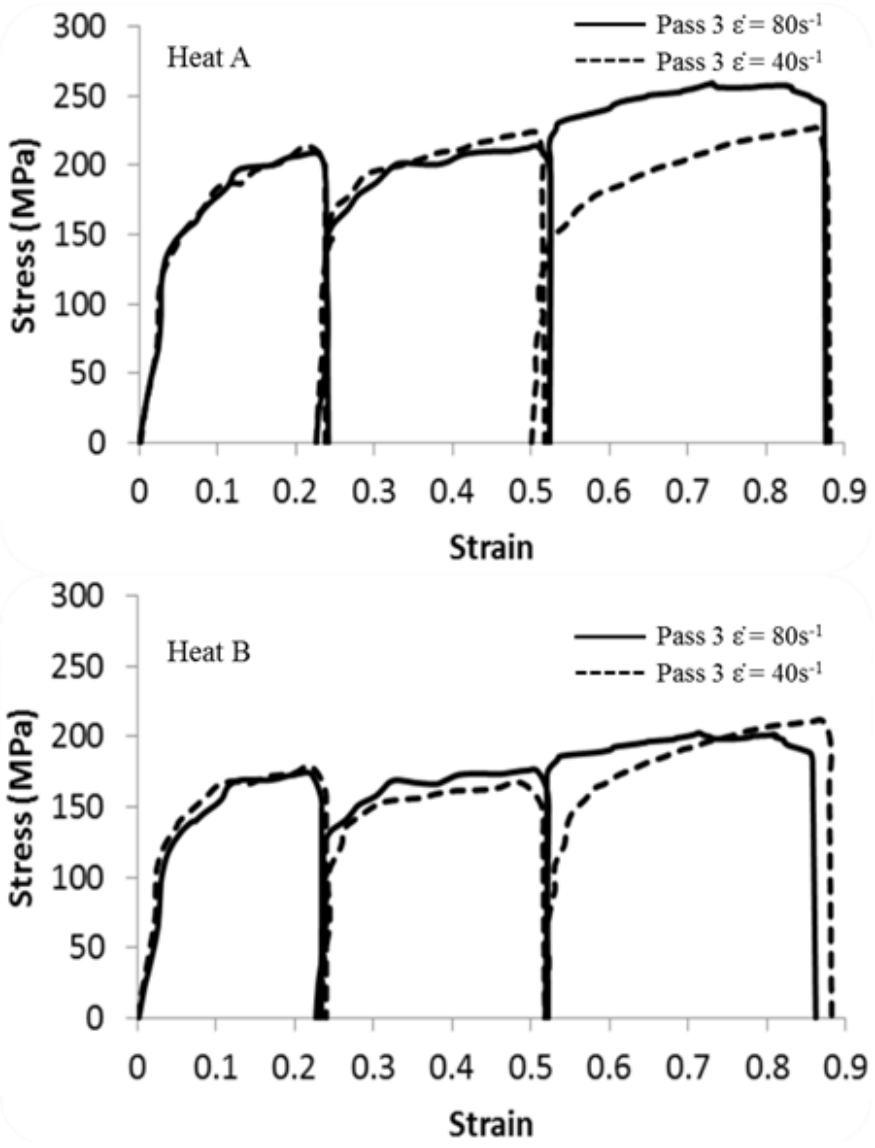

Figure 4.1: Flow stress curves of heat A and B during 3 consecutive Steckel mill deformation passes.

The yield stress values obtained during each deformation pass are shown in **Table 4.1**. It can be seen in **Table 4.1** that when the strain rate is increased from $40s^{-1}$ to $80s^{-1}$, the yield stress

increased from 150MPa to 230MPa in heat A. The same trend can be observed in heat B, where the yield stress increased from 100MPa to 180MPa when the strain rate is increased from $40s^{-1}$ to $80s^{-1}$. This behaviour is not unexpected given the general influence of increasing strain rate leading to greater difficulty in dislocation movement. The flow stress curves of heat A and B show similar trends, however the flow stress values of heat A are higher than those of heat B. This is due to the high austenite volume fraction in heat A during deformation and the fact that austenite is a higher strength phase than ferrite.

Table 4.1: Yield stress values during each deformation pass.

	Pass 1 σ_y	**Pass 2 σ_y**	**Pass $3_{(40)}$ σ_y**	**Pass $3_{(80)}$ σ_y**
Heat A	140 MPa	150 MPa	150 MPa	230 MPa
Heat B	100 MPa	100 MPa	100 MPa	180 MPa

4.2 Microstructure evolution prior to 1st pass deformation

In order to determine the starting microstructure prior to the commencement of the 3-pass deformation simulation, the respective heats A and B were heated to 1000°C, soaked for 10 mins followed by cooling to 890°C and thereafter air-quenched to room temperature (see section 3.3.2 for further details). **Figure 4.2** shows light microscope images of heat A and B after air-quenching. The microstructures consist of bands of α'-martensite and ferrite. The presence of α'-martensite indicates that austenite transformed to α'-martensite during quenching from deformation temperature to room temperature. However, the light microscope images do not show a clear indication of the phase transformation of austenite to secondary ferrite during the pre-deformation heat treatment. Therefore further analysis was performed using EBSD.

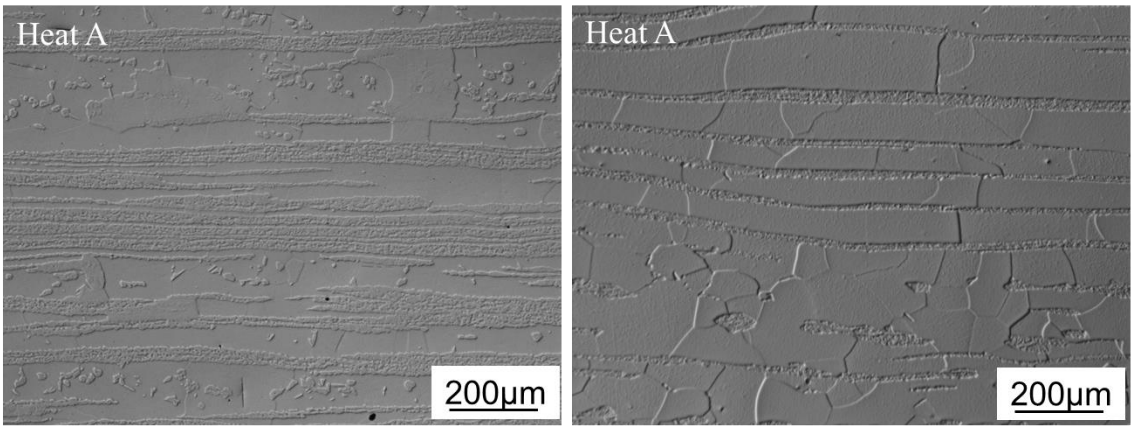

Figure 4.2: Light microscope images of heat A and B after pre-deformation heat treatment.

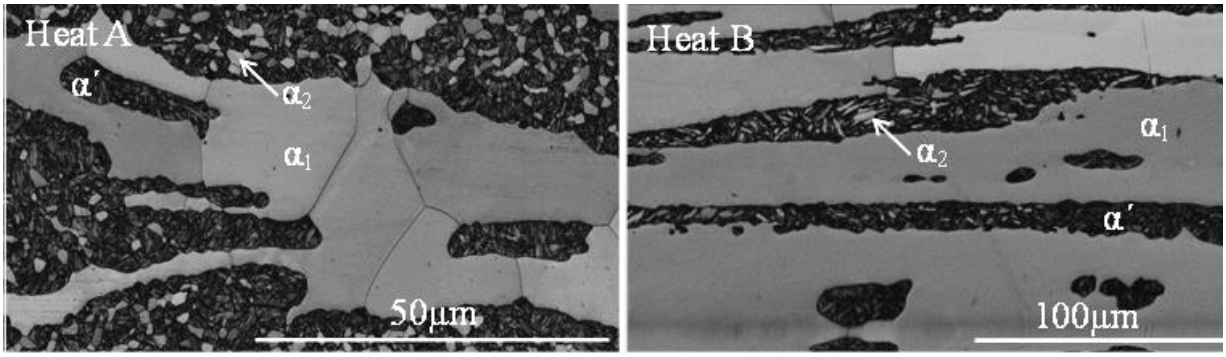

Figure 4.3: EBSD band contrast maps of heat A and B after pre-deformation heat treatment. EBSD mapping conditions; magnification 1000X, step size 0.2 µm and working distance 10mm.

$$\alpha_1 \xrightarrow[\alpha_1 \rightarrow \gamma]{\text{heat to } 960^{\circ}\text{C}} \alpha_1 + \gamma \xrightarrow[\gamma \rightarrow \alpha_2]{\text{heat to} 1000^{\circ}\text{C}} \alpha_1 + \gamma + \alpha_2 \xrightarrow[\alpha_2 \rightarrow \gamma]{\text{cool to } 960^{\circ}\text{C}} \alpha_1 + \gamma + \alpha_2 \xrightarrow[\gamma \rightarrow \alpha_2]{\text{cool to } 890^{\circ}\text{C}} \alpha_1 + \gamma + \alpha_2$$

Figure 4.4: phase transformations which occur during the pre-deformation heat treatment in heat A and B.

Figure 4.3 shows EBSD band contrast maps of heat A and B after the pre-deformation heat treatment. The microstructures consist of primary ferrite (α_1) and secondary ferrite (α_2), as well as α′-martensite. The occurrence of secondary ferrite as inclusions within the α′-martensite matrix indicates that austenite partially transformed to secondary ferrite during the pre-deformation heat treatment. The phase transformation of ferrite to austenite occurs during heating to temperatures above 800°C in heat A and B. This is indicated by an increase in austenite volume fraction, as shown in **Figure 3.1**. The shape of the austenite phase field in the phase

diagrams in **Figure 3.1** indicates that for heat A, the peak austenite volume fraction of 58% occurs at 960°C and the austenite volume fraction then decrease to 55% when the temperature is further increased to 1000°C. The same trend is seen in heat B, where the peak austenite volume fraction of 26% occurs at 940°C and decreases to 24% at 1000°C. Although the stated volume fractions might not be exact, since equilibrium is unlikely to be attained. This decrease in austenite volume fraction with an increase in temperature causes the austenite formed during heating through the peak temperature to partially transform to secondary ferrite in order to reduce the volume fraction of austenite during the pre-deformation heat treatment.

During cooling from 1000°C to 890°C, two stages of phase transformation take place. Stage 1 occurs through the phase transformation of ferrite to austenite during cooling from 1000°C to peak austenite volume fraction temperature of 960°C. Stage 2 involves the phase transformation of austenite to secondary ferrite when cooling from peak austenite volume fraction temperature to 890°C. Consequently, the secondary ferrite inclusions in the α´-martensite matrix are a result of phase transformation of austenite to secondary ferrite during heating to 1000°C and cooling to 890°C. The phase transformations that occur during the pre-deformation heat treatment are shown in **Figure 4.4.**

The light microscope images in **Figure 4.2** and EBSD maps in **Figure 4.3** indicate that the phase transformations shown in **Figure 4.4** occurred in heat A and B, however the microstructures of heat A indicate that there is higher volume fraction of α´-martensite and secondary ferrite compared to heat B. This is due to the high austenite volume fraction in heat A compared to heat B.

4.3 Microstructure evolution during hot deformation

Figure 4.5 illustrates light micrographs of heat A and B after deformation. The microstructures consist of bands of α'-martensite and ferrite. The α'-martensite and primary ferrite bands developed a pancake structure and elongate parallel to the rolling direction as the amount of strain increases. This results in the reduction of the distance between the α'-martensite and primary ferrite bands.

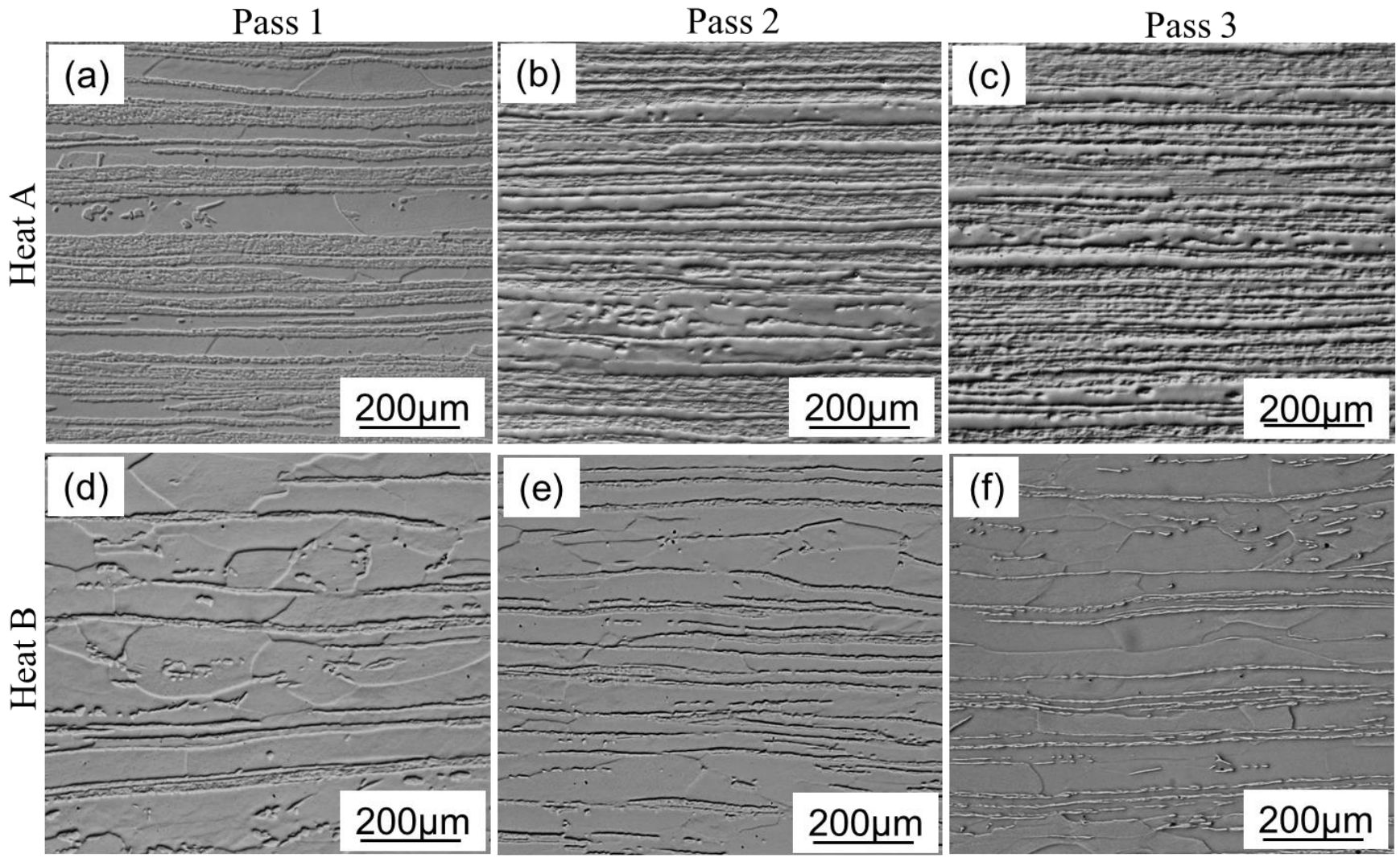

Figure 4.5: Light microscope images of heat A (a) to (c) and heat B (d) to (f) after (a) and (d) 1 pass, (b) and (e) 2 passes (c) and (f) 3 passes. *(Third pass strain rate: 80s^{-1}).*

The distance between primary ferrite and α'-martensite bands in heat A is shorter than that of heat B, even though heat A and B were deformed using the same deformation parameters. This is due to the high volume fraction of austenite in heat A at the deformation temperature.

Further microstructure analysis was performed using EBSD. **Figure 4.6** illustrates the microstructures of heat A and B after the one, two and three passes. The strain rate for pass 3 in **Figure 4.6** was $80s^{-1}$. The microstructures consist of primary ferrite, α´-martensite and inclusions of secondary ferrite within the α´-martensite matrix. The EBSD maps indicate that the α'-martensite and primary ferrite bands as well as the secondary ferrite grains within the martensite matrix show a pancake structure in heat A and B. The pancake morphology of the secondary ferrite grains indicate that these grains were formed through the phase transformation of austenite to ferrite during the pre-deformation heat treatment. The microstructures do not show strain free ferrite grains in the prior austenite regions, therefore phase transformation of austenite to ferrite did not occur during cooling after the last pass.

The flow stress curves in **Figure 4.1** show that static and dynamic recovery are the dominant restoration mechanisms, however the microstructures show that these restoration mechanisms occurred in the ferrite grains. Owing to the phase transformation of austenite to α'-martensite during quenching to room temperature, it is difficult to determine the restoration mechanisms in the prior austenite regions by using qualitative microstructural analysis. The texture evolution in the prior austenite regions can be used to estimate the texture of the parent austenite grains as well as the restoration mechanism that took place during processing [33]. Texture evolution and restoration mechanisms taking place in the prior austenite regions are discussed in **Section 4.5.2.** The microstructures indicate that subgrain formation occurs in the primary ferrite grains directly adjacent to the prior austenite regions. Recovery takes place in this particular location because austenite has a higher strength compared to ferrite at processing temperatures, therefore ferrite experiences more strain compared to the surrounding austenite grains and this is the driving force for the formation of primary ferrite subgrains.

Figure 4.6: EBSD band contrast maps of heat A (a) to (c) and heat B (d) to (f) after (a) and (d) 1 pass, (b) and (e) 2 passes (c) and (f) 3 passes. EBSD mapping conditions: magnification 1000X, step size 0.2 µm and working distance 10mm. *(Third pass strain rate: 80s^{-1}).*

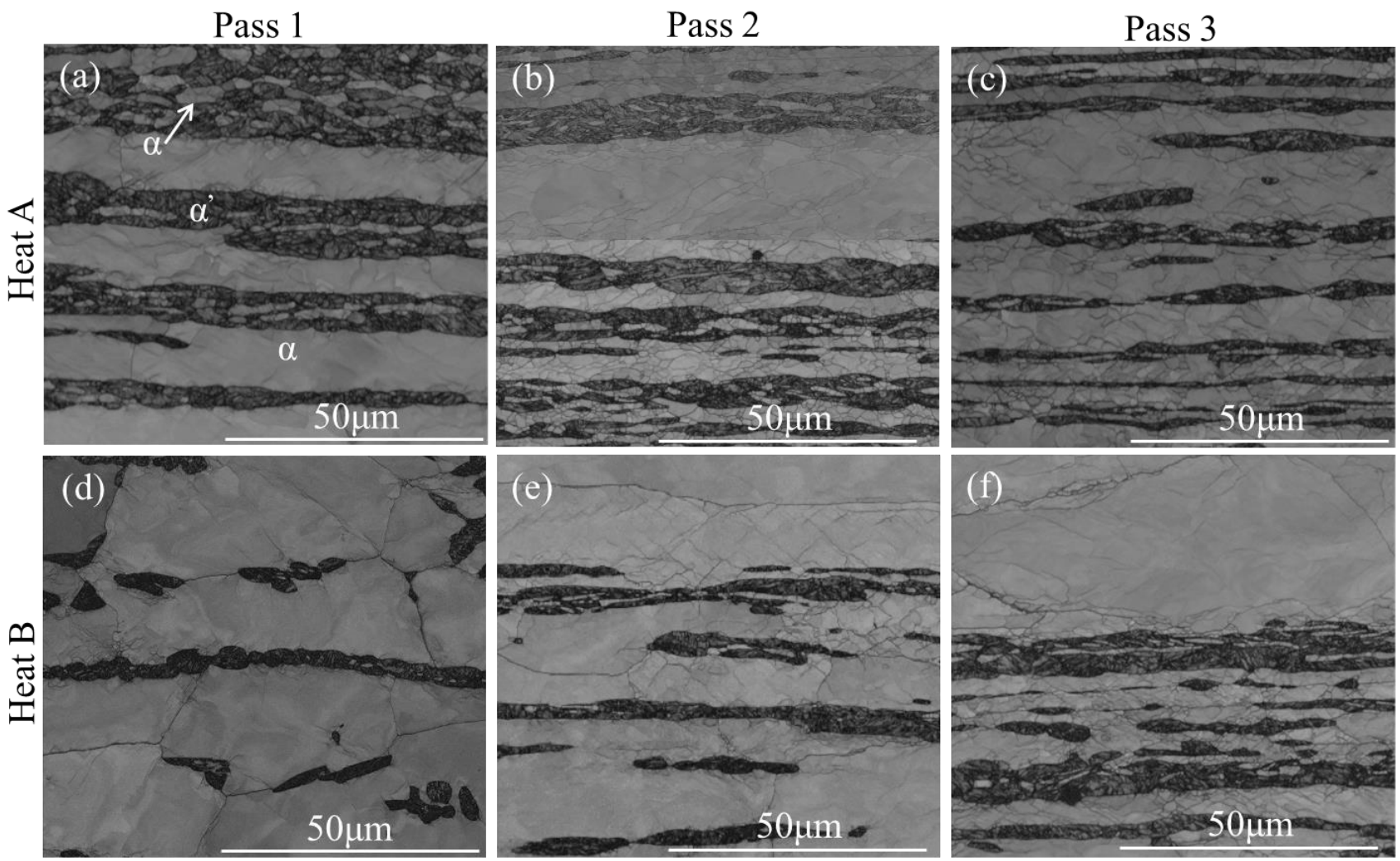
Pass 1
Pass 2
Pass 3
Heat A
Heat B
(a)
(b)
(c)
(d)
(e)
(f)
α
α'
α
50μm
50μm
50μm
50μm
50μm
50μm

The microstructures of heat A in **Figure 4.6** show that the ferrite subgrain formation occurred during the second and third pass. The flow stress curves show that recovery occurred during the interpass time between the first and second pass. This is indicated by a low stress value at the start of the second pass. Therefore the ferrite subgrain formation occurred through static and dynamic recovery during the interpass time and during deformation, respectively. Recovery occurs through a series of events, namely cell formation, annihilation of dislocations within cells, subgrain formation as well as subgrain growth [34]. The microstructures of heat A shows evidence of subgrain formation and subgrain growth after the two and three consecutive Steckel mill passes, respectively. The microstructure of heat A after the three consecutive passes shows a low number of subgrains compared to the microstructure after the two consecutive passes.

The microstructures of heat B in **Figure 4.6** show that ferrite subgrain formation occurred during the first pass deformation. In addition, the number of ferrite subgrains increased with increasing strain in heat B.

4.4 Texture evolution during deformation

4.5.1 Texture evolution in the primary ferrite grains

Figure 4.7 shows ODF sections at $\varphi_2 = 45^\circ$ of the pre-deformation heat treated and deformed samples. The ODFs show that after the pre-deformation heat treatment and the first pass, the ferrite grains consisted of a uniform α-fiber texture. However the strength of α-fiber texture increased during the first pass deformation. After two and three consecutive deformation passes, α-fiber texture became non-uniform with a strong {001} <110> rotated cube texture. In addition, a weak γ-fiber texture is also present after two consecutive passes. After three passes (third pass strain rate of $80s^{-1}$), the texture of the ferrite grains was dominated by non-uniform α-and γ-fiber textures with strong {001}<110> and {111}<112> texture components. The ODF sections at $\varphi_2 = 45^\circ$ indicate that before deformation the ferrite grains consisted of uniform α-fiber texture. However, as the amount of strain increased, α-fiber texture changed from a uniform state to a non-uniform state while the {001}<110> and {111}<112> texture components become more prominent.

4.5.2 Texture evolution in the prior austenite regions

The ODF sections in **Figure 4.8** show that after the pre-deformation heat treatment the textures in the prior austenite regions (now α'-martensite) were fairly random with a weak {001}<110>. After the first pass uniform and weak α- and γ-fiber textures were developed. After the two and three successive deformation passes the {111}<112>, and {001}<110> texture components became more prominent. The γ-fiber is uniform; however α-fiber is non-uniform throughout the hot deformation process. The texture evolution in the prior austenite regions show that the {001}<110> and {111}<112> texture components become more prominent as the amount of strain increases. This was also observed in the texture evolution of primary ferrite grains; however, the prior austenite regions show a uniform γ-fiber, whereas the primary ferrite grains show a non-uniform γ-fiber, as shown in **Figure 4.7**. Hinton and Beynon [30] also found that the rotated cube texture with {001}<110> component is the dominant texture component and intensifies with increasing strain in type 430 stainless steel. **Figure 4.7** and **Figure 4.8** show that intensity of the texture components increase with increasing strain (number of passes). Furthermore, the better defined {111}<112> texture in the primary ferrite phase after the 3rd pass at a strain rate of 80s^{-1} suggests that there is some degree of ferrite recrystallization which has occurred metadynamically or statically following the last pass. The presence of strong {111}<112> texture component in the prior austenite regions indicate an initial {110}<112> orientation of the parent austenite phase [23]. The {110}<112> texture component is well known from heavily cold rolled austenitic stainless steels.

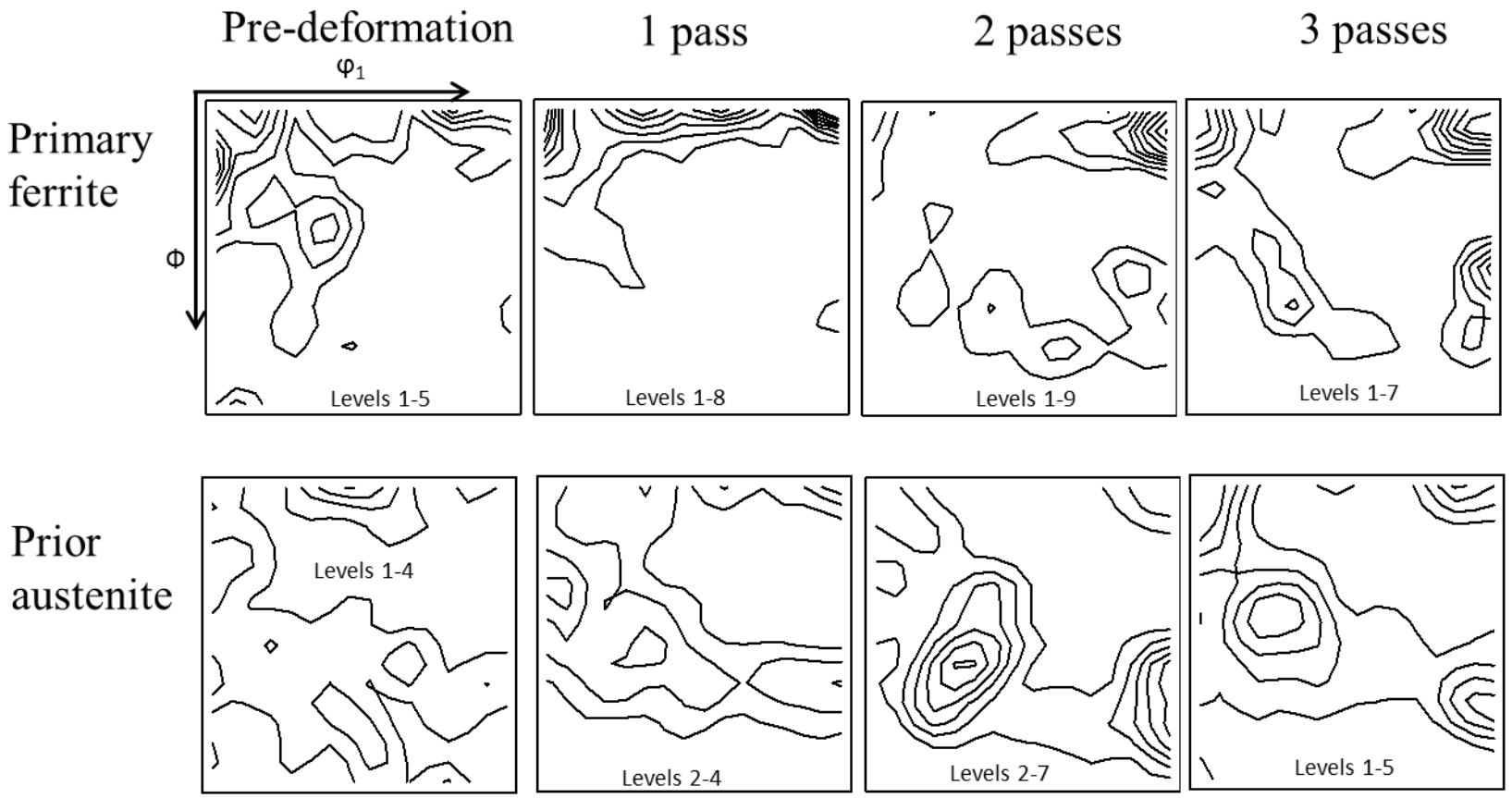

Figure 4.7: Texture representation of pre-deformation heat treated and deformed samples of heat A in the ferrite and prior austenite regions using ODFs at $\varphi_2 = 45°$. *(Third pass strain rate: 80s^{-1}).*

4.5.3 The effect of strain rate on texture evolution

Texture evolution is influenced by deformation parameters such as temperature, strain and strain rate. In order to investigate the effect of strain rate on texture evolution, plane strain compression tests were performed using the Steckel mill hot rolling parameters, however the third pass strain rate was reduced from $80s^{-1}$ to $40s^{-1}$. The flow stress curves indicate that deformation at strain rate of $40s^{-1}$ result in an increased work hardening rate.

The ODF sections at $\varphi_2 = 45^{\circ}$ in **Figure 4.8** indicate that the primary ferrite grains show a strong non uniform α-fiber texture with strong {001}<110> texture component in both high and low strain rate conditions. However when the third pass deformation occurred at a strain rate of $80s^{-1}$; the primary ferrite grains developed a strong {111}<112> texture component, whereas deformation at $40s^{-1}$ resulted in a weak γ-fiber texture. The prior austenite regions developed uniform γ-fiber texture with strong {111}<112> when deformed at a strain rate of $80s^{-1}$ as shown in **Figure 4.8**. However, deformation at $40s^{-1}$ resulted in the development of weaker uniform γ-fiber texture in the prior austenite regions, as shown in **Figure 4.8.**

The explanation for the difference in the flow curves for the 3^{rd} pass at $40s^{-1}$ and $80s^{-1}$ is provided in section 4.1. The rapid onset of softening (leading to a low work-hardening rate) for the $80s^{-1}$ test probably arises as a result of adiabatic heating contributing to recovery and even possibly metadynamic recrystallization as the texture suggests (i.e. well defined {111}<112> in the primary ferrite grains.

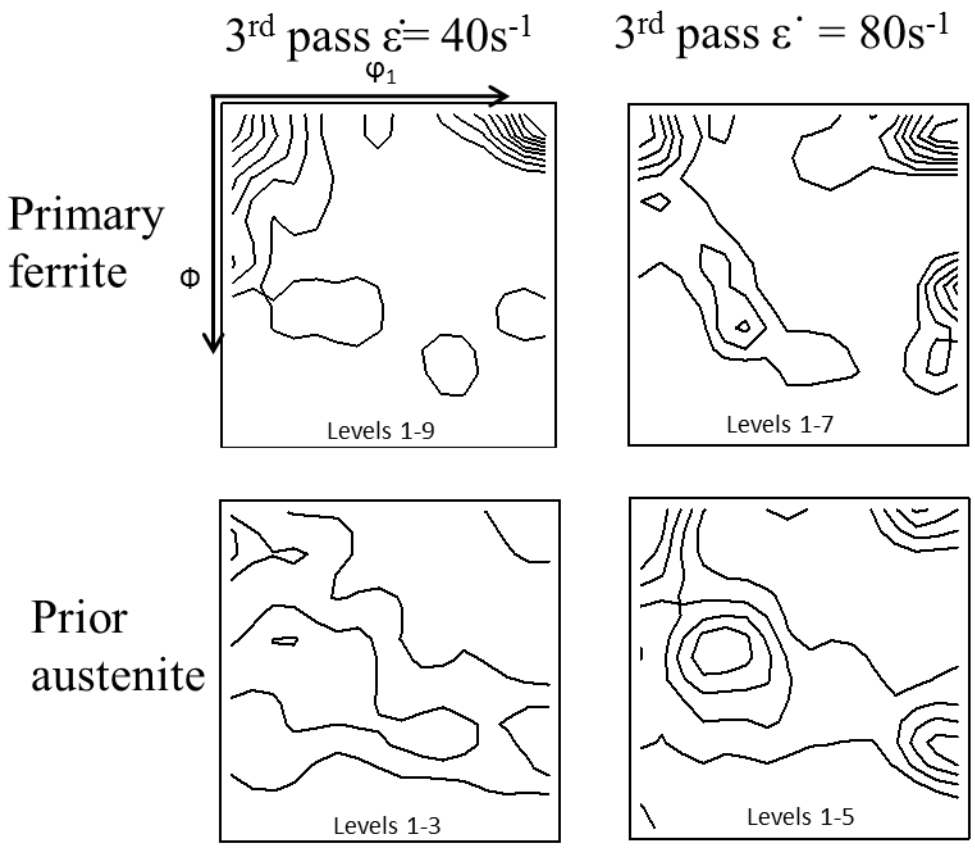

Figure 4.8: Texture representation deformed samples of heat A in the ferrite and prior austenite regions using ODFs at φ_2= 45°.

4.5.4 The effect of austenite volume fraction on texture evolution

Figure 4.9 shows the φ_2 = 45˚ ODFs of heat A and B after three consecutive Steckel mill hot rolling process. **Figure 4.9** indicates that heat A consists of strong α-and γ-fiber texture components in both the primary and prior austenite regions. However, **Figure 4.9** shows that heat B consists of strong α-fiber texture components with very weak γ-fiber texture components in the primary ferrite regions. The prior austenite regions in heat B consist of weak α- and γ-fiber texture components.

The microstructures in **Figure 4.3** as well as the flow stress curves in **Figure 4.1** indicate that the microstructure evolution in heat A and B occurs through dynamic recovery. Although the microstructure of heat A and B shows similar microstructural features, the texture development in both heats indicate that the effect of high austenite volume fraction is to intensify α- and γ-texture components as shown in **Figure 4.9**. The ferrite experiences higher strain in heat A compared

to heat B (the higher volume fraction of austenite in heat A partitions more strain to the primary ferrite phase). Consequently, when comparing the texture in the ferrite phase in the two heats (at the same strain rate), heat A is more likely to undergo some recrystallisation (higher strain energy driving force). The stronger {111}<112> texture in the primary ferrite in heat A supports this proposal.

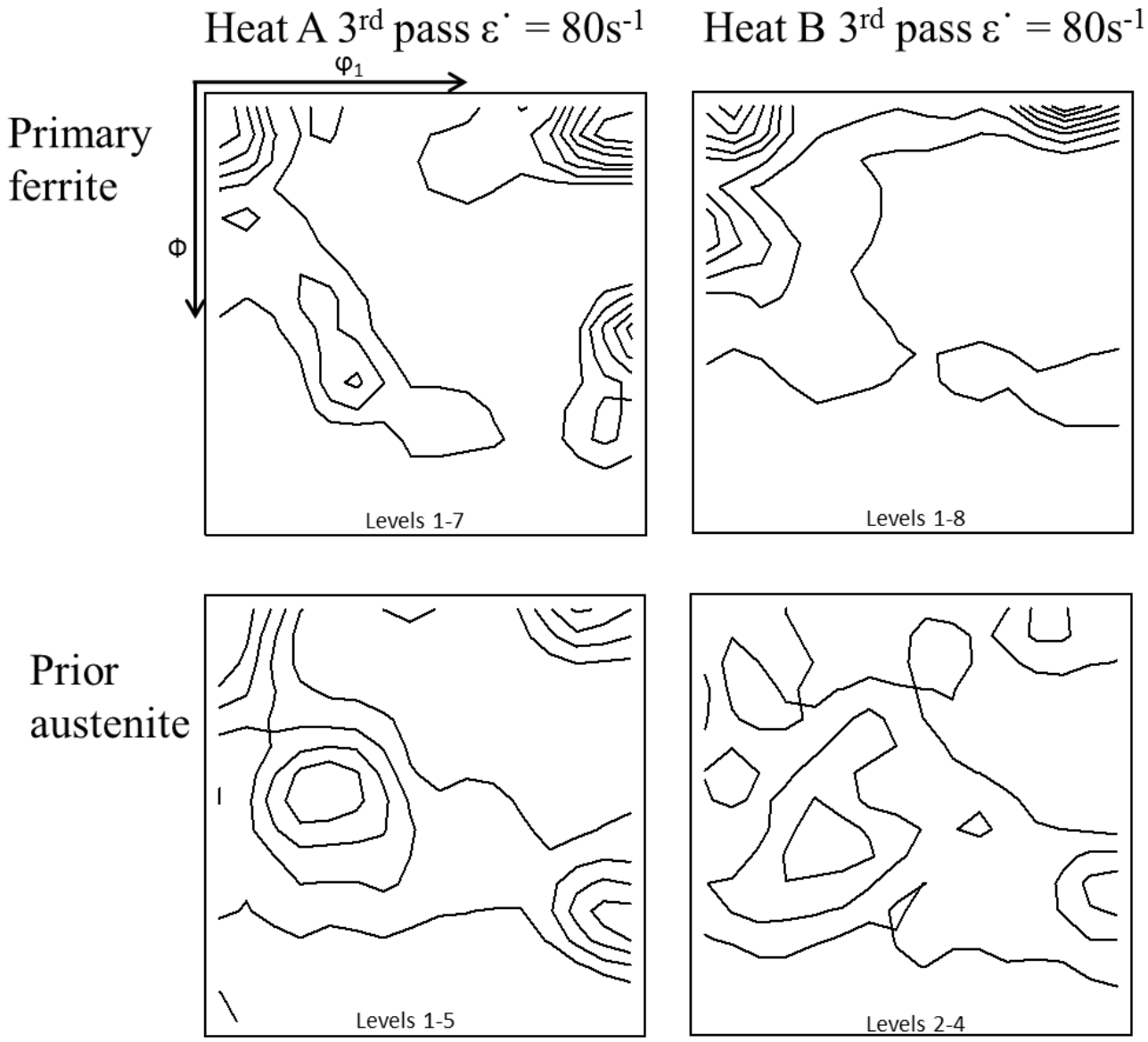

Figure 4.9: ODFs at $\varphi_2 = 45^{\circ}$ showing the texture components after three consecutive simulated Steckel mill hot rolling parameters.

5. MICROSTRUCTURE AND TEXTURE EVOLUTION DURING POST DEFORMATION HEAT TREATMENTS

The purpose of the post deformation heat treatments was to investigate the effect of phase transformation, austenite volume fraction, temperature and strain rate on the microstructure evolution and texture development of AISI 430 FSS.

Two post deformation heat treatments were performed. The first post deformation heat treatment was designed such that samples were quenched from the third pass deformation temperature to the annealing temperature of 700°C and 800°C and then annealed for 15 and 30 minutes. This post deformation heat treatment will be referred to as the continuous phase transformation heat treatment in this study. During the continuous phase transformation heat treatment, austenite transformed to secondary ferrite

During the second post deformation heat treatment samples were quenched from the third pass temperature to room temperature, followed by re-heating the sample to the annealing temperature of 700°C or 800°C. The samples were annealed in the salt bath for 15, 30 and 60 minutes. This heat treatment will be referred to as the martensite tempering heat treatment. During the martensite tempering heat treatment, the martensite transformed to secondary ferrite.

Two deformation protocols were used for this investigation. In the first deformation protocol, samples were deformed using three successive Steckel mill deformation passes followed by quenching to room temperature. The third pass strain rate used during the first deformation protocol was $80s^{-1}$. The second deformation protocol was similar to the first protocol, however the third pass strain rate was decreased from $80s^{-1}$ to $40s^{-1}$. The same protocols were applied for the continuous phase transformation exercise.

This chapter will focus on the results and discussions of the microstructure evolution and texture development during continuous phase transformation and martensite tempering heat treatments.

5.1. Microstructure evolution during continuous phase transformation heat treatment of heat A

5.1.1. Microstructure evolution of heat A deformed at 3rd pass strain rate of $40s^{-1}$

Figure 5.1 shows the microstructures of heat A after annealing at 700°C for 15 and 30 minutes. The EBSD maps in **Figure 5.1 (a)** and **(b)** show that after 15 minutes at 700°C the microstructure consists of α'-martensite and primary ferrite bands. **Figure 5.1 (b)** shows a high magnification EBSD map of the sample annealed at 700°C for 15 minutes. The EBSD map indicates that the non-indexed points in **Figure 5.1 (a)** consist of α'-martensite bands. The presence of α'-martensite after annealing at 700°C for 15 minutes indicate that the microstructure consisted of austenite and ferrite at 700°C and austenite transformed to α'-martensite during quenching from 700°C to room temperature. The EBSD maps in **Figure 5.1 (a)** and **(b)** also show the presence of low angle boundaries in the primary ferrite regions. This implies that recovery may have further progressed during the isothermal heat treatment. The microstructures in **Figure 4.6** also indicate that recovery occurred during hot deformation.

Figure 5.1 (c) and **(d)** illustrates the microstructure of heat A after soaking at 700°C for 30 minutes. The EBSD map shows that the microstructure is fully ferritic after 30 minutes at 700°C. The microstructure in **Figure 5.1 (c)** shows a low number of low angle grain boundaries compared to the microstructure in **Figure 5.1 (a).** Annealing at 700°C for more than 15 minutes promoted complete phase transformation of austenite to ferrite.

It can be seen in the light microscope image in **Figure 5.1 (d)** that the formation of precipitates occurred during annealing at 700°C for longer than 15 minutes. Precipitation occurred at ferrite grain boundaries as shown by the red arrow in **Figure 5.1 (d).** A study by Mola *et al*. [3] showed that precipitation occurred during hot rolling of FSS alloy at the austenite and ferrite two phase temperature range. The FSS alloy investigated by Mola *et al* had a combined C and N content of 0.103 wt. % and Al content of 0.11 wt. %. The C and N contents are similar to that of heat A; however, the Al content is greater than that of heat A, as shown in **Table 3.1**. Mola *et al*. reported that the precipitates formed during the annealing heat treatment were $Cr_{23}C_6$ and $Fe_{23}C_6$ carbides as well as aluminium nitride (AlN). The precipitates shown in **Figure 5.1 (d)** could be $Cr_{23}C_6$ and

$Fe_{23}C_6$ carbides as well as AlN. The location of the carbides is consistent with the work of Mola *et al.*

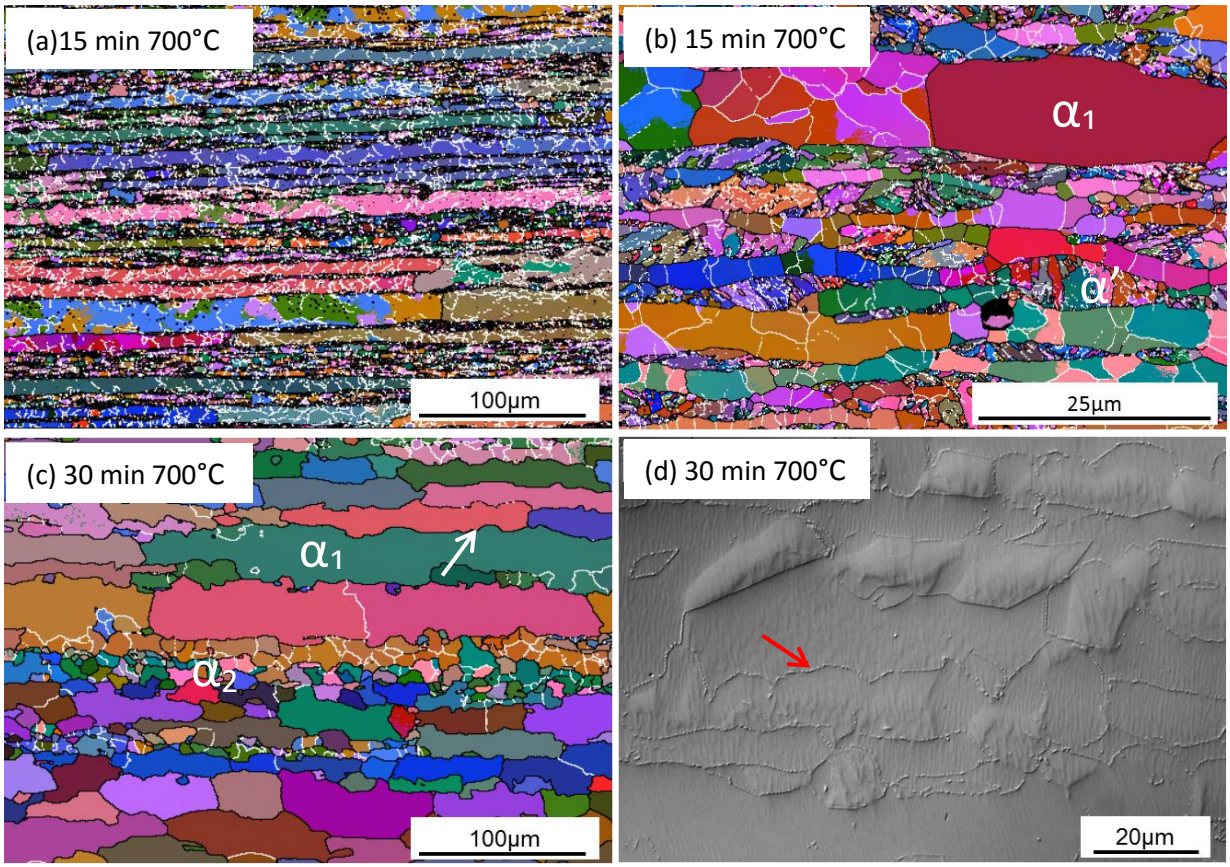

Figure 5.1: Microstructures of the sample deformed at third pass strain rate of $40s^{-1}$ and continuous phase transformation annealing heat treatment at 700°C. (a) and (b) low and high magnification EBSD maps after 15 minutes at 700°C, respectively. (c) and (d) show low magnification EBSD map and light microscope image after 30 minutes at 700°C. *(α_1: primary ferrite, α_2: secondary ferrite, α': martensite. White > 2˚and Black > 15˚misorientation)*

Figure 5.2 shows the microstructures of heat A after annealing at 800°C for 15 and 30 minutes. The microstructures consist of primary and secondary ferrite grains. The microstructures in **Figure 5.2 (a)** and **(b)** illustrate that austenite fully transformed to ferrite during annealing at 800°C for 15 minutes. This is indicated by the absence of martensite.

The light microscope images in **Figure 5.2 (e)** and **(f)** show that precipitation of carbides occurred at the ferrite grain boundaries. This was also observed in the microstructures annealed at 700°C for 30 minutes. However, the microstructure in **Figure 5.2 (e)** shows that precipitation occurred

within the first 15 minutes of the annealing time at 800°C while precipitates were observed after 30 minutes at 700°C. This means that annealing at 800°C promoted the phase transformation of austenite to ferrite, as well as the formation of precipitates during the first 15 minutes of the annealing time. Consequently, the rate of phase transformation of austenite to secondary ferrite and the precipitation of carbides is higher when annealing at 800°C compared to 700°C.

Figure 5.2 (b) and **(d)** shows that the primary ferrite grain growth occurred during the annealing heat treatment at 800˚C as indicated by the "wavy" grain boundaries in the primary ferrite grains. The "wavy" grain boundaries are indicated by the white arrows in **Figure 5.2 (b)** and **(d)**.The EBSD maps in Error! Reference source not found. **(a) and (c)** indicate that significant recovery occurred during deformation and isothermal heat treatment at 800°C. This is indicated by the presence of low angle boundaries in the microstructures, which persist even after significant time at 800˚C. It is quite evident that insufficient stored energy exists to promote significant recrystallisation and the subgrain structure remains stable. The microstructures also show that there is a high concentration of low angle boundaries in the primary ferrite grains surrounding the prior austenite regions which supports the notion that strain partitioning occurred in the primary ferrite grains surrounding the prior austenite regions.

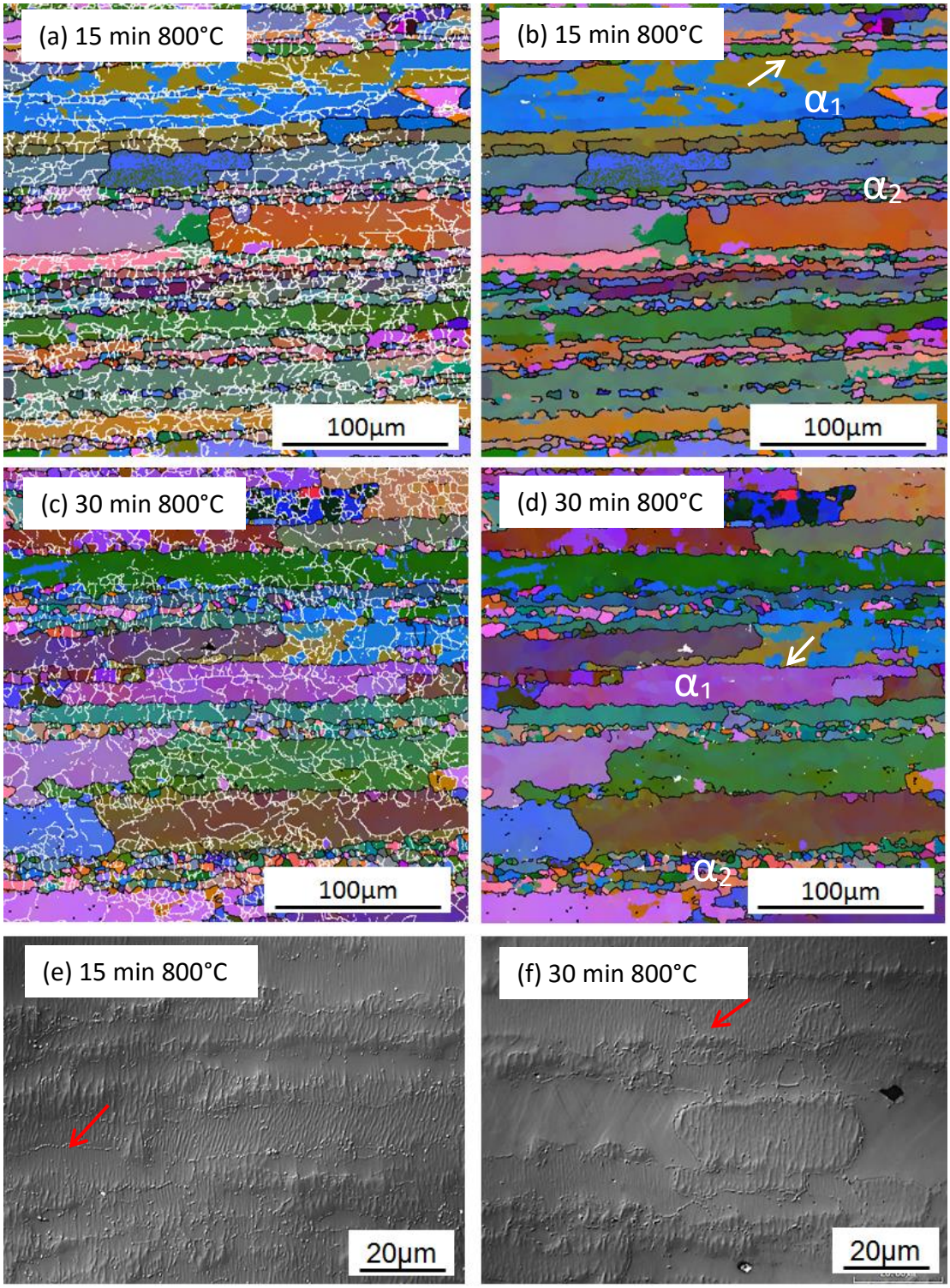

Figure 5.2: Microstructures of the sample deformed at third pass strain rate of $40s^{-1}$ followed by continuous phase transformation annealing heat treatment at 800°C. EBSD Euler map and light microscope images of the samples annealed at 800°C for (a), (b), (e) 15 minutes and (c), (d), (f) 30 minutes. (*α_1- primary ferrite, α_2- secondary ferrite, α': martensite. White > 2˚and Black > 15˚misorientation)*

5.1.2. Microstructure evolution of heat A deformed at 3rd pass strain rate of 80s^{-1}

Figure 5.3 and **Figure 5.4** show the microstructures of heat A after annealing at 700°C and 800°C, respectively. The microstructures consist of α'-martensite and primary ferrite bands after annealing for 15 minutes. This means that the microstructure consisted of austenite and ferrite at 700°C and 800°C; however during quenching after 15 minutes from the isothermal heat treatment to room temperature austenite transformed to α'-martensite. After 30 minutes at both annealing temperatures, the microstructure is fully ferritic, as shown in **Figure 5.3 (c)** and **(d)** and **Figure 5.4 (c)** and **(d)**. **Figure 5.3 (e)** and **Figure 5.4 (e)** show a high magnification EBSD Euler map that exhibits that the non-indexed points in **Figure 5.3 (b)** and **Figure 5.4(b)** consist of α'-martensite. The presence of α'-martensite in these microstructures indicates that the continuous phase transformation annealing heat treatment at 700˚C and 800˚C for 15 minutes was not sufficient to promote complete phase transformation of austenite to ferrite. However, **Figure 5.3 (c)** and **(d)** and **Figure 5.4 (c)** and **(d)** show that austenite completely transformed to secondary ferrite when the samples were soaked at 700˚C and 800˚C for 30 minutes.

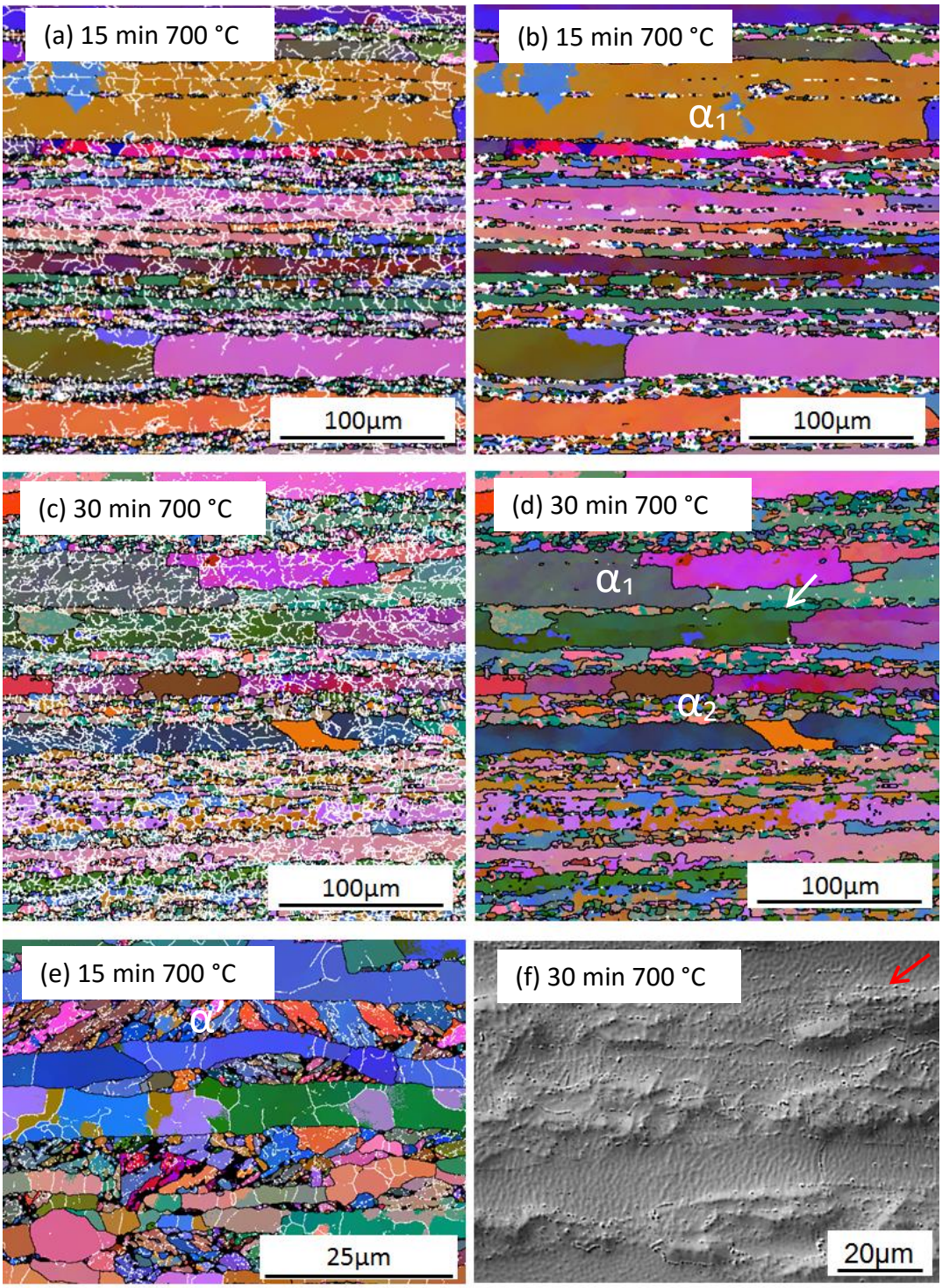

Figure 5.3: Microstructures of the sample deformed at third pass strain rate of $80s^{-1}$ followed by continuous phase transformation annealing heat treatment at 700°C. EBSD Euler maps of the samples annealed at 700˚C for (a),(b),(e) 15 minutes and (c), (d) 30 minutes. Light microscope image of the sample annealed at 700˚C for 30 minutes showing carbides precipitate. *(α_1- primary ferrite, α_2- secondary ferrite, α'- martensite. White > 2˚and Black > 15˚misorientation)*

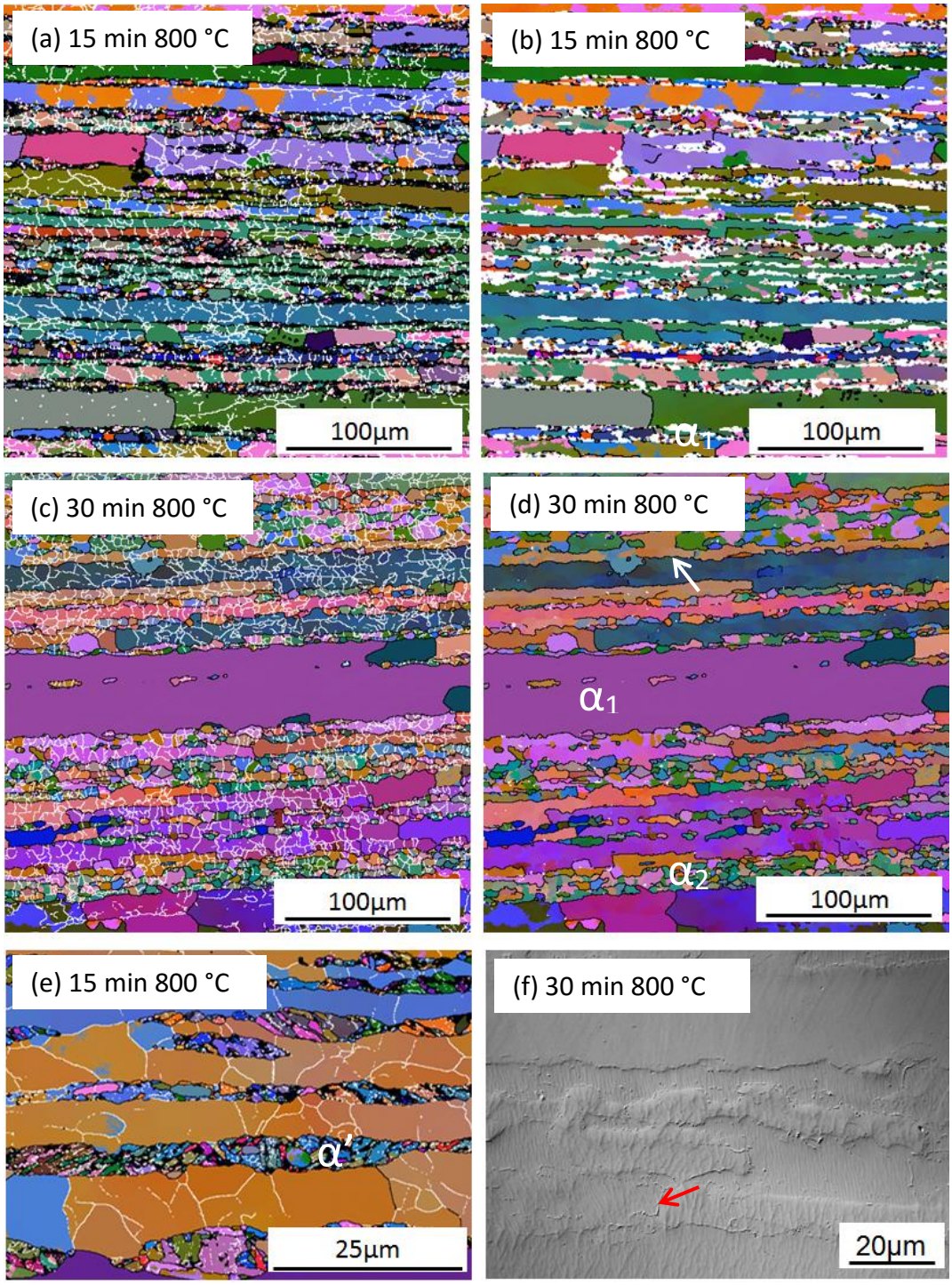

Figure 5.4: Microstructures of the sample deformed at third pass strain rate of $80s^{-1}$ followed by continuous phase transformation annealing heat treatment at 800°C. EBSD Euler maps of the samples annealed at 700˚C for (a), (b), (e) 15 minutes and (c),(d) 30 minutes. Light microscope image of the sample annealed at 700˚C for 30 minutes showing carbides precipitate. *(α_1- primary α, α_2- secondary α, α'- martensite. White > 2˚and Black > 15˚misorientation)*

Figure 5.3 (d) and **Figure 5.4 (d)** show that grain growth of primary ferrite occurred through the consumption of secondary ferrite grains, as shown by the "wavy" primary ferrite grain boundaries as indicated by the white arrow in **Figure 5.3 (d)** and **Figure 5.4 (d)**. This was also observed in **Figure 5.1 (c)** and **Figure 5.2 (b)** and **(d)** where the samples were deformed at a third pass strain rate of $40s^{-1}$. **Figure 5.3 (f) a**nd **Figure 5.4 (f)** show that annealing for 30 minutes promotes the formation of carbides at ferrite grain boundaries, as shown by the red arrow.

The EBSD maps in **Figure 5.3 (a)** and **(c)** and **Figure 5.4 (a)** and **(c)** show that recovery was the dominant restoration mechanism during deformation and annealing heat treatments at 700˚C and 800˚C. This is indicated by the presence of low angle grain boundaries in the microstructures of the deformed and annealed samples. FSS alloys have a high stacking fault energy; this means that dislocation climb and cross slip is rapid, hence the microstructures show that significant recovery occurred during deformation and isothermal heat treatment.

A study by Hinton and Beynon [30] showed that deformation at low strain rates resulted in a well-defined subgrain structure, which was believed to be due to longer deformation time allowing dynamic recovery to occur. However, the study showed that deformation at high strain rates was not sufficient to promote dynamic recovery. This means that the occurrence of restoration processes during the annealing heat treatment are dependent on the deformation and annealing conditions.

Figure 5.1 to 5.4 show that the following processes occurred during the continuous phase transformation heat treatment of heat A at 700˚C and 800˚C; recovery and phase transformation of austenite to secondary ferrite followed by the grain growth of the primary ferrite grains through the consumption of the secondary ferrite grains. The presence of low angle grain boundaries in the primary ferrite grains of the deformed and annealed samples indicate that recovery occurred during deformation and continuous phase transformation heat treatment. For the most part the primary ferrite maintains large elongated grains which are subdivided by persistent subgrain structures. Despite the earlier reference to the possibility of primary ferrite recrystallisation after the 3rd pass at 80s-1, there is little evidence to suggest that this has occurred. However, it is difficult to distinguish between recrystallised primary ferrite and

transformed austenite in some instances and hence the likelihood of some primary ferrite recrystallisation should not be dismissed. The austenite decomposition to ferrite occurs much faster at 800˚C. **Table 5.1** shows a summary of the results obtained during continuous phase transformation heat of heat A.

Table 5.1: summary of results obtained from the continuous heat treatment of heat A at 700˚C and 800˚C

Sample	α_1	α_2	α’	carbides	Figure no.	Comments and observations
40 SR 700˚C 15min	✓	×	✓	×	5.1 (a) & (b)	• Recovery in the α_1 grains • Phase transformation of γ to α’-martensite. • 15 min insufficient for complete phase transformation of γ to α_1
40 SR 700˚C 30min	✓	✓	×	✓	5.1 (c) & (d)	• Absence of α’-martensite indicate complete phase transformation of γ to α_2 • Therefore 30 min at 700˚C sufficient for γ to completely transform to α_2 • Recovery and grain growth of α_1 grains
40 SR 800˚C 15min	✓	✓	×	✓	5.2 (a), (b) & (e)	• Absence of α’-martensite indicate complete phase transformation of γ to α_2 • Therefore 15 min at 800˚C sufficient for γ to completely transform to α_2 • Recovery and grain growth of α_1 grains • Carbides precipitation
40 SR 800˚C 30min	✓	✓	×	✓	5.2 (c), (d) & (f)	Same as **40 SR 800˚C 15min**
80 SR 700˚C 15min	✓	×	✓	×	5.3 (a), (b) & (e)	Same as **40 SR 700˚C 15min**.
80 SR 700˚C 30min	✓	✓	×	✓	5.3 (c), (d) & (f)	Same as **40 SR 700˚C 30min**.
80 SR 800˚C 15min	✓	×	✓	×	5.4 (a), (b) & (e)	Same as **40 SR 700˚C 15min**
80 SR 800˚C 30min	✓	✓	×	✓	5.4 (c), (d) & (f)	Same as **40 SR 700˚C 30min**.

5.1.3. The effect of austenite volume fraction on the microstructure evolution during continuous phase transformation heat treatment

Figure 4.6 (c) and (f) showed the microstructures of heat A and heat B after three successive Steckel mill passes respectively. The microstructure consists of primary ferrite and α'-martensite bands. The microstructures also indicate that recovery is the dominant restoration mechanism during deformation as shown by the presence of subgrains in the primary ferrite grains.

Figure 5.5 (a) and **(b)** illustrate the microstructure of heat B after annealing at 700˚C for 15 and 30 minutes respectively. The microstructures in **Figure 5.5 (a)** and **(b)** consist of primary and secondary ferrite grains.

Figure 5.5 (a) and (b) also show that the primary ferrite grains show two types of grain boundaries; wavy and straight grain boundaries as indicated by the white and black arrows. The wavy ferrite grain boundaries were also observed in heat A after continuous phase transformation heat treatment 700˚C and 800˚C as shown in, **Figure 5.3 (a)** and **(c).** The presence of secondary α grains and the wavy grain boundaries in the microstructures of heat B after annealing at 700˚C for 15 and 30 minutes indicate that austenite transformed to secondary ferrite, followed by grain growth of the primary ferrite grains through the consumption of the secondary ferrite grains. This is indicated by the migrated grain boundaries as a result of grain growth.

The microstructures of heat A in **Figure 5.3 (a), (b)** and **(e)** shows that annealing at 700˚C for 15 minutes was not sufficient for complete phase transformation of austenite to ferrite. However, the microstructures of heat B in **Figure 5.5 (a)** shows that the austenite completely transformed to secondary ferrite during annealing at 700˚C for 15 minutes. It can be seen in **Figure 5.5** and **Figure 5.6** that continuous phase transformation heat treatment of heat B resulted in grain growth of the primary ferrite grains and precipitation of carbides during the first 15 minutes of the annealing time at 700˚C. The absence of significant subgrain boundaries indicates that the primary ferrite grains have mostly undergone continuous recrystallisation (extended recovery).

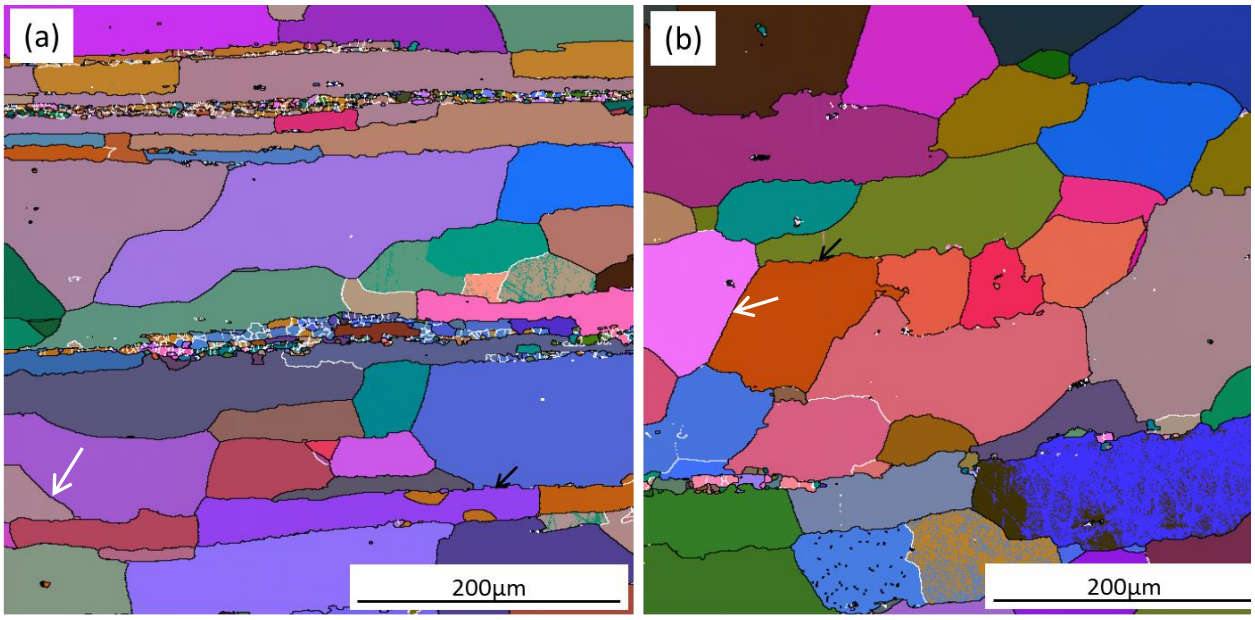

Figure 5.5: EBSD Euler maps of heat B after continuous phase transformation heat treatment at 700°C for (a) 15 and (b) 30 minutes deformed at a third pass strain rate $80s^{-1}$.

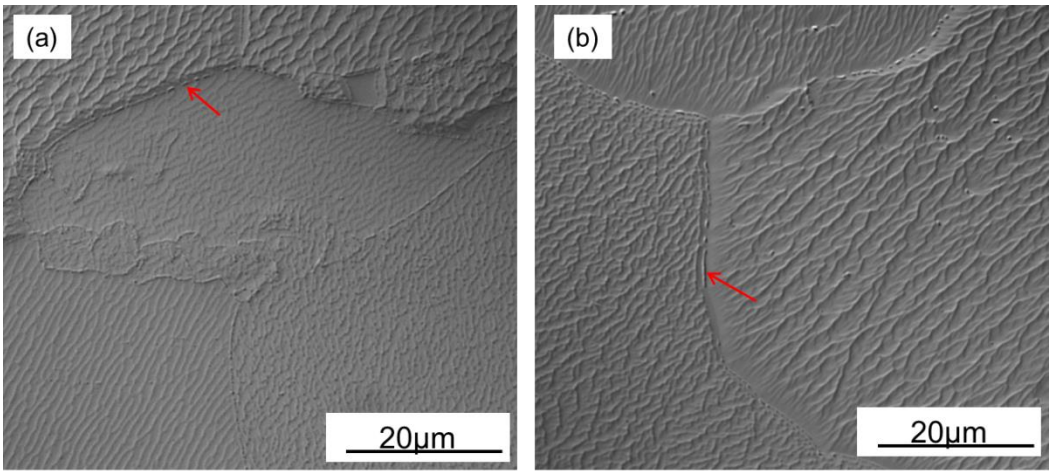

Figure 5.6: Light microscope images of heat B after continuous phase transformation heat treatment at 700°C for (a) 15 and (b) 30 minutes deformed at a third pass strain rate $80s^{-1}$.

5.2. Texture evolution of heat A during continuous phase transformation heat treatment

5.2.1. Texture evolution of heat A deformed at 3rd pass strain rate of $40s^{-1}$

The microstructures in **Figure 5.1 (a)** and **(b)** indicated that after annealing at 700°C for 15 minutes, austenite did not transform to ferrite. This is illustrated by the presence of α'-martensite

in the prior austenite regions. Texture analysis was then performed in the prior austenite and primary ferrite regions. **Figure 5.7** shows the φ_2 = 45˚ ODF section of the sample annealed at 700°C for 15 minutes. The φ_2 = 45˚ ODF section in **Figure 5.7** indicates that both regions consist of α-and γ-fiber textures, however the intensity of the texture components varies, in that the ODFs in **Figure 5.7** indicate that the annealing heat treatment at 700°C for 15 minutes promoted the development of γ-fiber texture with strong {111}<112> texture components in the primary ferrite regions. Also, the as-quenched prior austenite regions exhibit a weak γ-fiber which strengthens after the heat treatment at 700°C for 15 minutes. The ODFs indicate that the prior austenite regions consist of continuous γ-fiber texture, whereas the γ-fiber texture in the primary ferrite is not continuous. The prior austenite texture after isothermal heat treatment at 700°C for 15 minutes of course represents a mixture of residual martensite and secondary ferrite.

Annealing at 700°C for 30 minutes resulted in complete phase transformation of austenite to ferrite, as shown in **Figure 5.1 (c)**. The ODF in **Figure 5.8** indicates that after annealing at 700˚C for 30 minutes, the microstructure consisted of α-fiber texture component only in the primary ferrite regions, which does not support discontinuous recrystallisation. By comparison, the texture in the primary ferrite (**Figure 5.9**) after isothermal heat treatment at 800°C for 15 minutes indicates well defined near {111}<112> components. This texture almost disappears after annealing at 800°C for 30 minutes. Findings from two previous investigations will be used to explain this behaviour. Hinton and Beynon [30] investigated restoration processes during hot deformation of AISI 430 FSS and showed that annealing at 960˚C for 10 seconds resulted in strengthening and weakening of the α- and γ-fiber texture components, respectively. Furthermore, the microstructures and flow stress curves showed that recovery was the dominant restoration mechanism. A study by Huh and Engler [19] showed that when recrystallization was the dominant restoration mechanism the α-fiber texture became weak while the γ-fiber texture became uniform with strong {111}<112> texture component. Recovery only of the deformed primary ferrite strengthens the α-fiber texture. If appreciable discontinuous recrystallisation occurs initially, then the γ-fiber texture components will appear. However, if grain growth is allowed to occur, then the recrystallised grains will be consumed by the larger recovered grains and the γ-fiber will disappear. Consequently, the texture evolution in the primary ferrite is

argued as follows. Weak γ-fiber occurs in the primary ferrite after 700°C for 15 minutes. This disappears after annealing for 30 minutes (Figs. 5.7 and 5.8 respectively). When annealed at 800°C, then the γ-fiber is significantly stronger after 15 minutes which supports the earlier comment that recrystallization occurs more easily at 800°C. Nevertheless, when soaked at 800°C for 30 minutes, the γ-fiber weakens substantially (see **Figure 5.9**). The ODFs in **Figure 5.9** indicate that the prior austenite regions consist of strong and weak α- and γ-fiber texture components respectively after continuous phase transformation annealing heat treatment at 800 ˚C of the sample deformed at third pass strain rate of $40s^{-1}$. This means that phase transformation from austenite to ferrite promoted the development of the α-fiber texture components.

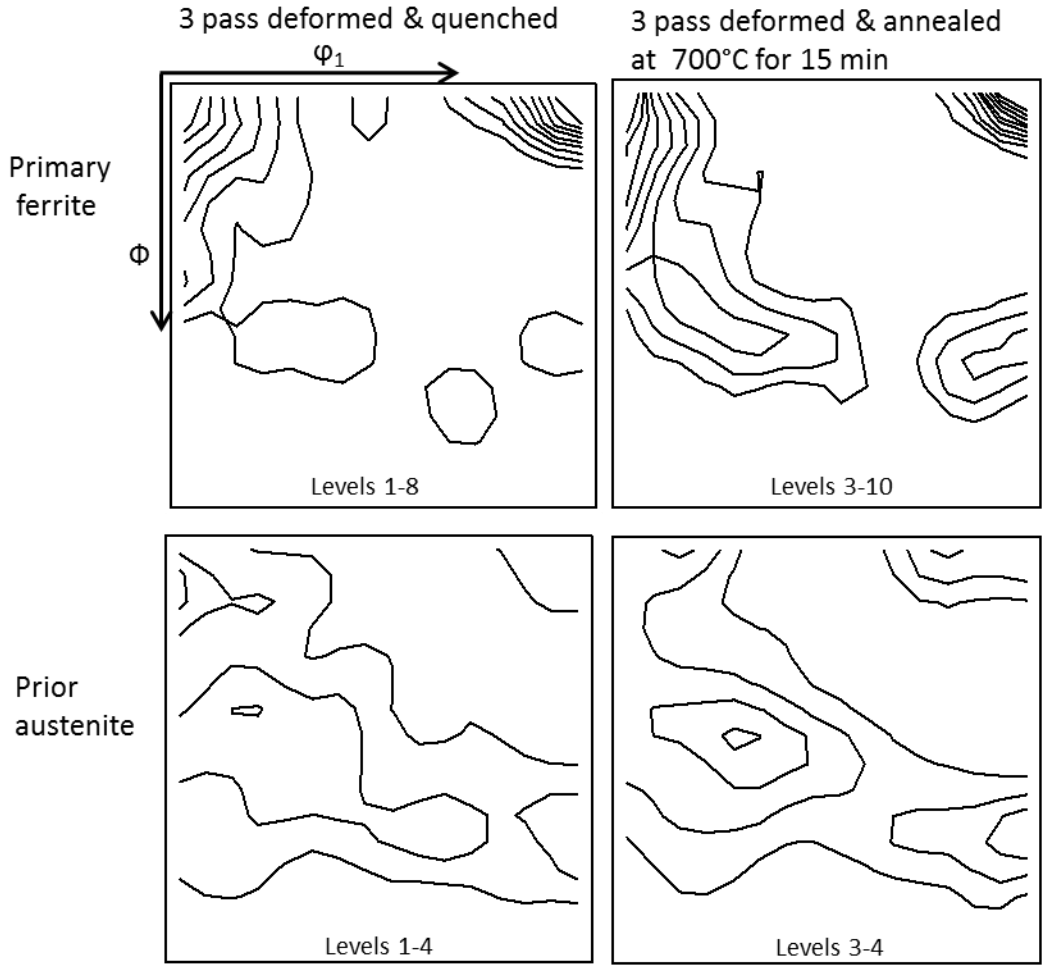

Figure 5.7: $\varphi_2 = 45^{\circ}$ ODF sections showing texture evolution of heat A during continuous phase transformation heat treatment at 700°C for 15 minutes. *(Third pass strain rate $40s^{-1}$)*

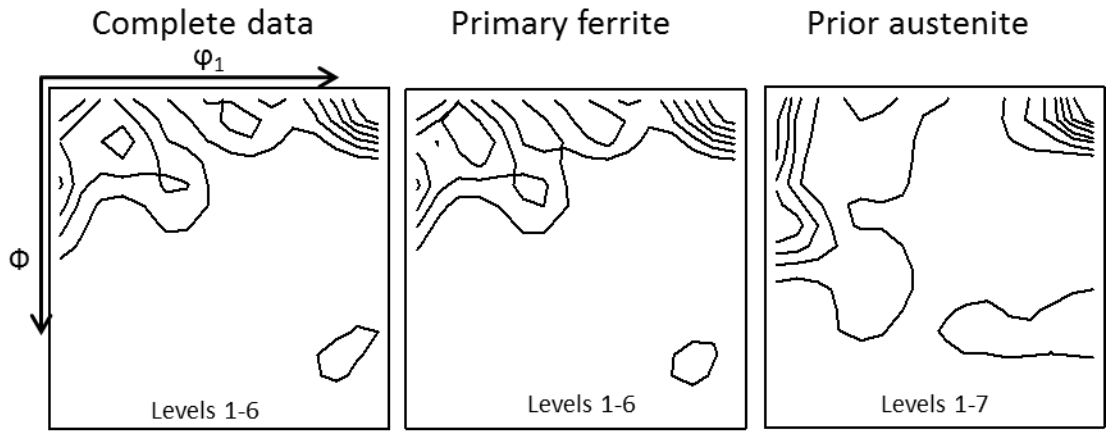

Figure 5.8: φ_2 = 45˚ ODF section showing texture of heat A after annealing at 700˚C for 30 minutes. *(Third pass strain rate 40s^{-1})*

The microstructures in **Figure 5.2 (a) and (b)** indicate that austenite completely transformed to ferrite during the first 15 minutes of the annealing heat treatment at 800°C. The ODFs of the prior austenite regions in **Figure 5.9** show that the intensity of the {001}<110> texture component increased during the first 15 minutes of the annealing heat treatment at 800°C and was weakened by further heat treatment up to 30 minutes. Although the austenite to ferrite transformation occurs by the K-S orientation relationship, and not discounting some degree of variant selection, the texture development during isothermal heat treatment, particularly at 800°C, suggests strong growth selection in favour of the {001}<110> component. Consequently, the expected γ-fiber texture in the now transformed secondary ferrite region is substantially weakened and the overall texture of the microstructure which evolves during hot deformation and continuous transformation is strengthened with respect to the α-fiber texture, and more particularly the {001}<110> component which is the 45 degree rotated cube orientation.

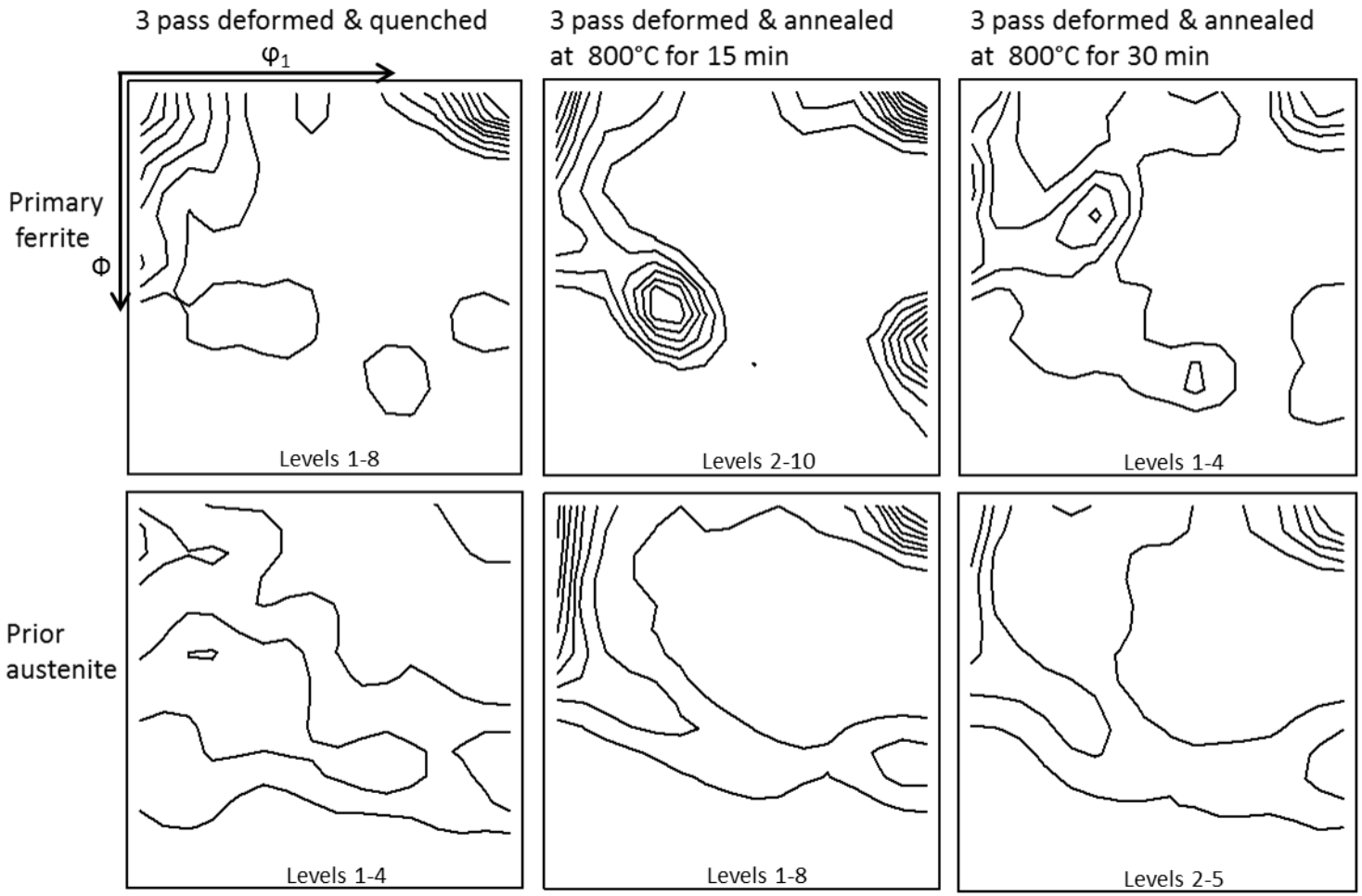

Figure 5.9: $\varphi_2 = 45^\circ$ ODF sections showing texture evolution of heat A during the annealing heat treatment at 800°C. *(Third pass strain rate 40s^{-1})*

5.2.2. Texture evolution of heat A deformed at 3rd pass strain rate of 80s^{-1}

Figure 5.10 and **Figure 5.11** show the texture evolution of heat A during continuous phase transformation heat treatment at 700°C and 800°C respectively. The ODFs in **Figure 4.7** indicate that the microstructure consisted of α and γ-fiber textures with strong {001}<110> and 111}<112> texture components after 3 pass deformation and quench to room temperature. Annealing at 700°C and 800°C for 15 minutes strengthened the γ-fiber texture components in the primary ferrite. Once again, this is consistent with the notion that some degree of recrystallization of the primary ferrite occurs in the early stages of isothermal annealing. These events most likely occur at the ferrite/austenite interface where the localized strain in the ferrite is expected to be greatest. The texture in the primary ferrite strengthens after isothermal heat treatment at 700°C for 30 minutes which suggests further recrystallization and recovery. By comparison, the γ-fiber texture disappears after soaking at 800°C for 30 minutes. The sustained isothermal heat treatment at the higher temperature promoted grain growth, which resulted in the smaller recrystallized grains being consumed and hence decrease in the γ-fiber texture component. The texture in the prior austenite regions is weak although the γ-fiber is easily identified. Further annealing at 700°C strengthened the α-fiber textures in both ferrite and prior austenite regions which supports growth selection. The microstructures in **Figure 5.3** and **Figure 5.4** show that austenite did not transform to ferrite during the first 15 minutes of the annealing heat treatment at 700°C and 800°C. However, annealing at both temperatures for longer than 15 minutes resulted in complete phase transformation of austenite to ferrite. Thus, the prior austenite regions of the samples annealed at 700°C and 800°C for 15 minutes consisted of martensite and some secondary ferrite. The weakening of the γ-fiber texture components in the prior austenite with increasing annealing time is due to phase transformation of austenite to ferrite and growth selection favouring the {001}<110> component.

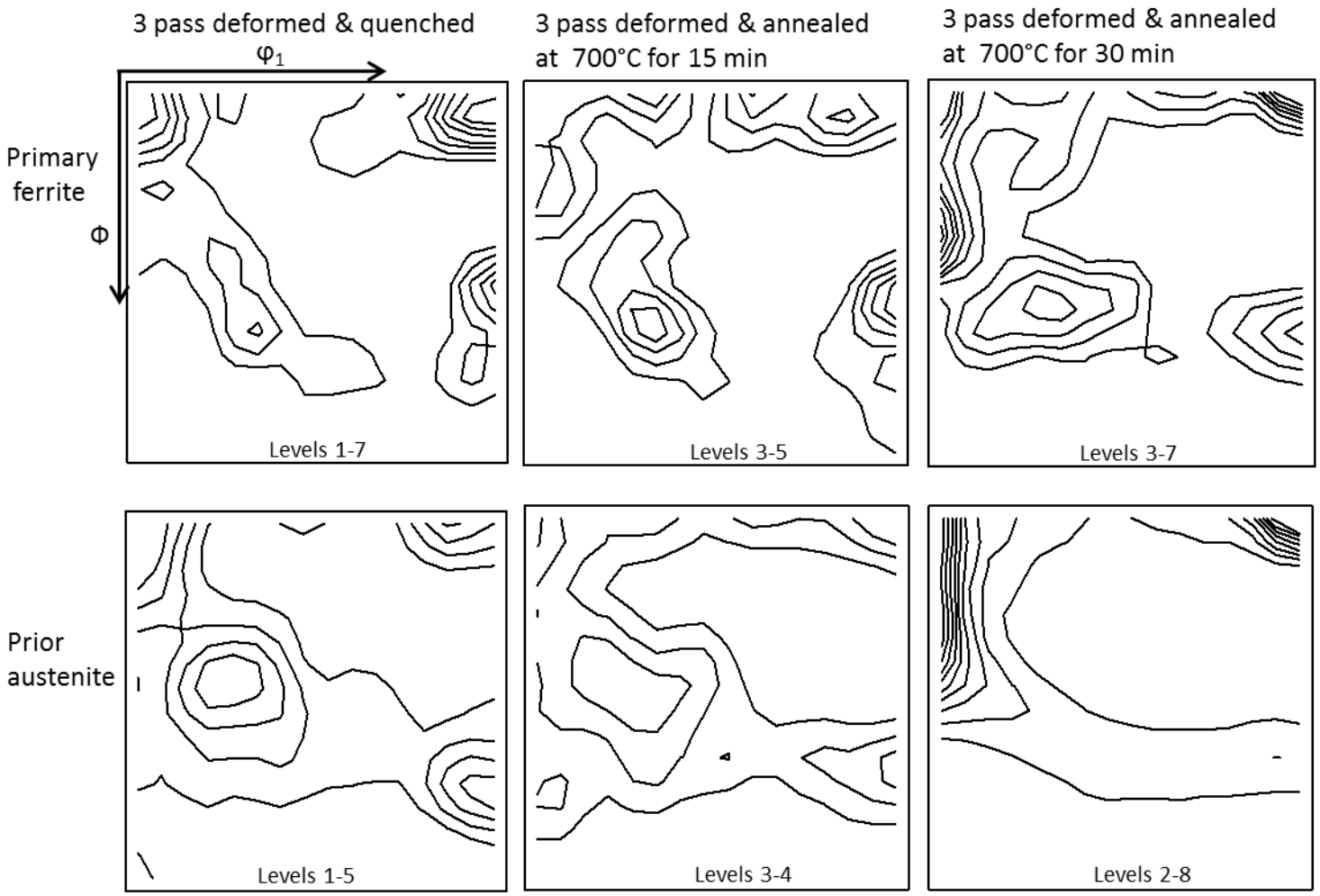

Figure 5.10: φ_2 = 45˚ ODF sections showing texture evolution of heat A during the annealing heat treatment at 700°C. *(Third pass strain rate 80s^{-1})*

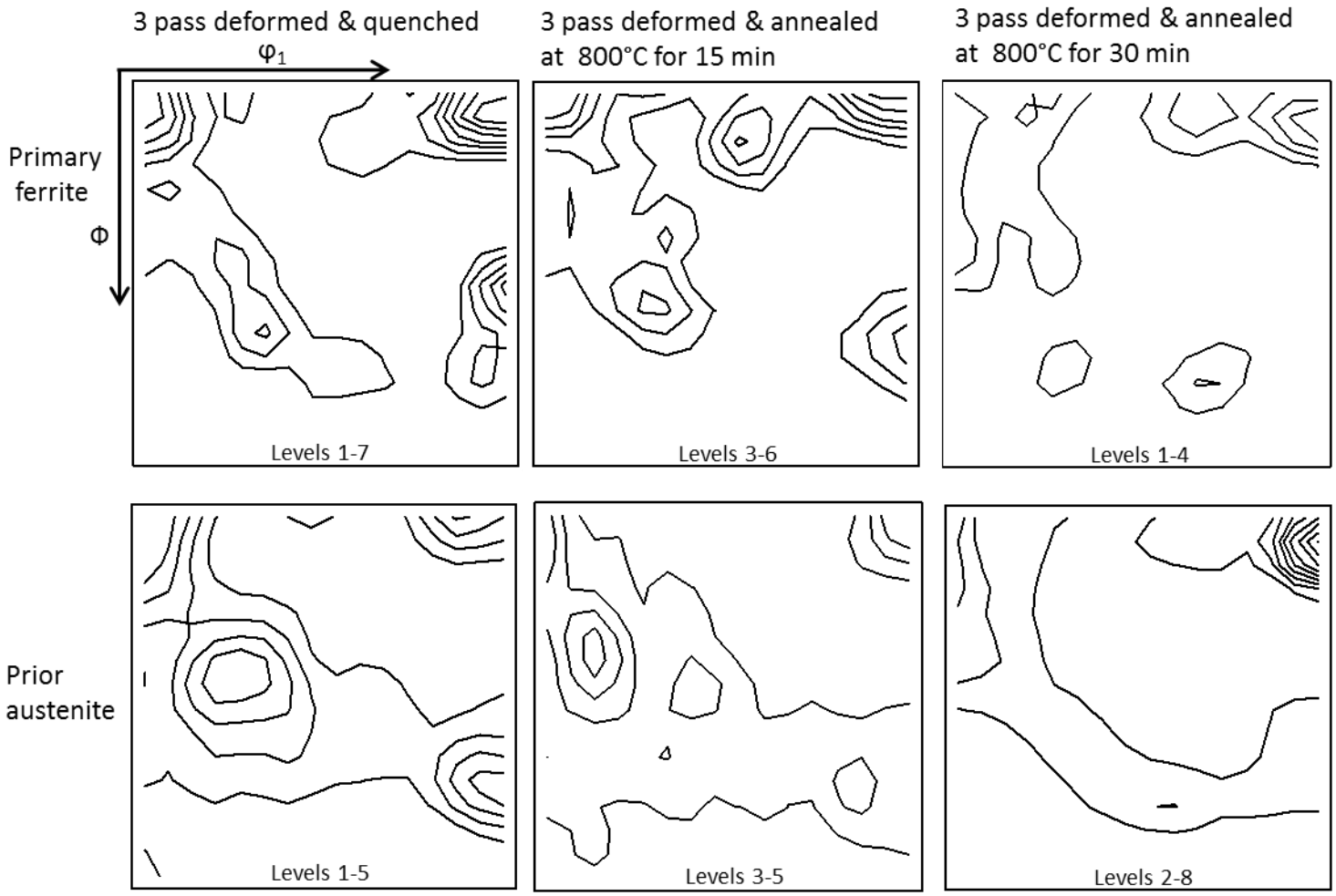

Figure 5.11: φ_2 = 45˚ ODF sections showing texture evolution of heat A during the annealing heat treatment at 800°C. *(Third pass strain rate 80s^{-1})*

5.2.3. The effect of austenite volume fraction on texture development

Figure 5.12 shows texture development of heat A and heat B during deformation and continuous phase transformation heat treatment in the primary ferrite regions. **Figure 5.12** shows that after three successive deformation passes, the primary ferrite grains of heat A consisted of the following α-fiber and γ-fiber texture components: {001}<110> and {111}<112>. However, continuous phase transformation annealing heat treatment for 15 minutes at 700°C resulted in slight weakening of the {001}<110> texture component. Further annealing at 700°C for 30 minutes strengthened the α-fiber texture components as shown in **Figure 5.12**.

After three successive passes, the primary ferrite grains in heat B also displayed dominant α-fiber texture. The intensity of {001}<110> texture component is similar to that of heat A. Isothermal heat treatment of heat B at 700°C for 15 minutes led to substantial weakening of the as deformed texture. After 30 minutes at the same temperature a major shift in texture occurred with an unusual peak at 45, 20, 45 on the ODF. It is difficult to explain this occurrence but it may be related to a near cube orientation.

The $\varphi_2 = 45^{\circ}$ ODF sections in **Figure 5.12** indicate that the higher austenite volume fraction in heat A promoted the development of {111}<112> texture component in the primary ferrite grains.

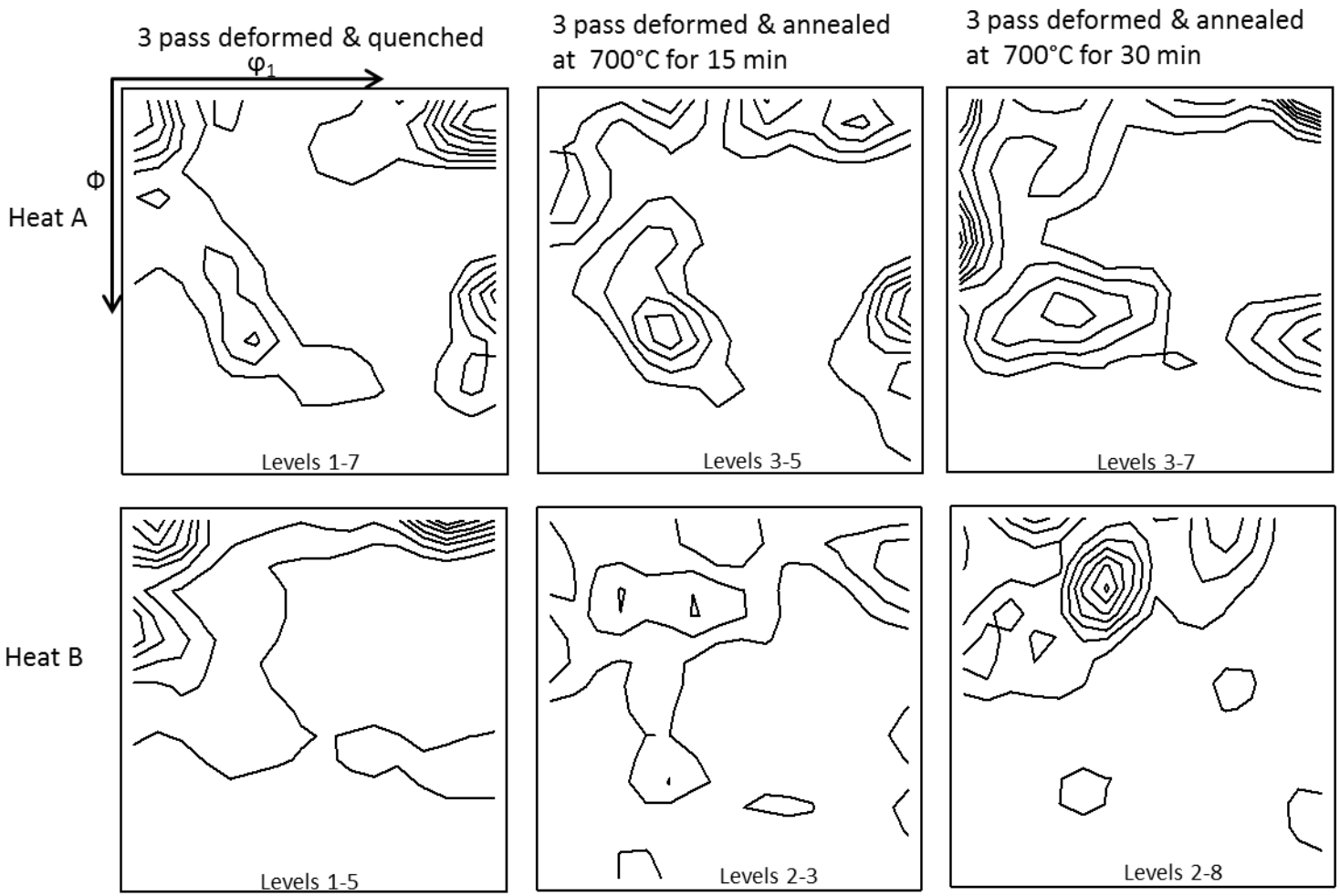

Figure 5.12: $\varphi_2 = 45^{\circ}$ ODF sections showing texture evolution of heat A and heat B during continuous phase transformation annealing heat treatment at 700°C. ***(****Third pass strain rate 80s^{-1})*

5.3. Microstructure evolution during martensite tempering heat treatment of heat A

The second post deformation heat treatment was designed such that samples were quenched from the third pass hot deformation temperature to room temperature. This was followed by reheating the samples from room temperature to annealing temperatures of 700˚C and 800˚C using a salt bath. The samples were annealed at 700˚C and 800˚C for 15, 30 and 60 minutes. The samples were subsequently quenched in water and then analysed using light microscopy and EBSD. The purpose of the second post deformation heat treatment was to temper the martensite in order to determine the effect of phase transformation of α'-martensite to ferrite on the microstructure evolution and texture development.

Figure 5.13 (a) shows the microstructure of heat A after quenching from the third pass deformation temperature to room temperature. The microstructure consists of bands of ferrite and martensite. The presence of martensite indicates that austenite transformed to martensite during quenching to room temperature. There are 10 possible misorientation angles i.e. 10.53˚, 14.88˚, 20.61˚, 21.06˚, 47.11˚, 49.47˚, 50.51˚, 51.73˚, 57.21˚, and 60.00˚, between the variants that satisfy the K-S orientation relationship [35]. However, in this study the martensite was found to be characterized by the misorientation angles of between 50˚ and 60˚, as shown in **Figure 5.13 (b)**. These misorientation angles are formed due to the transformation mechanism of austenite to martensite as well the nature of the martensite. **Figure 5.13 (b)** shows the misorientation profile across the martensite band indicated by the white dotted line in **Figure 5.13 (a)**. The misorientation profile shows that the martensite laths generally consist of misorietation angles ranging from 50˚ to 60˚, which is consistent with the K-S orientation relationship.

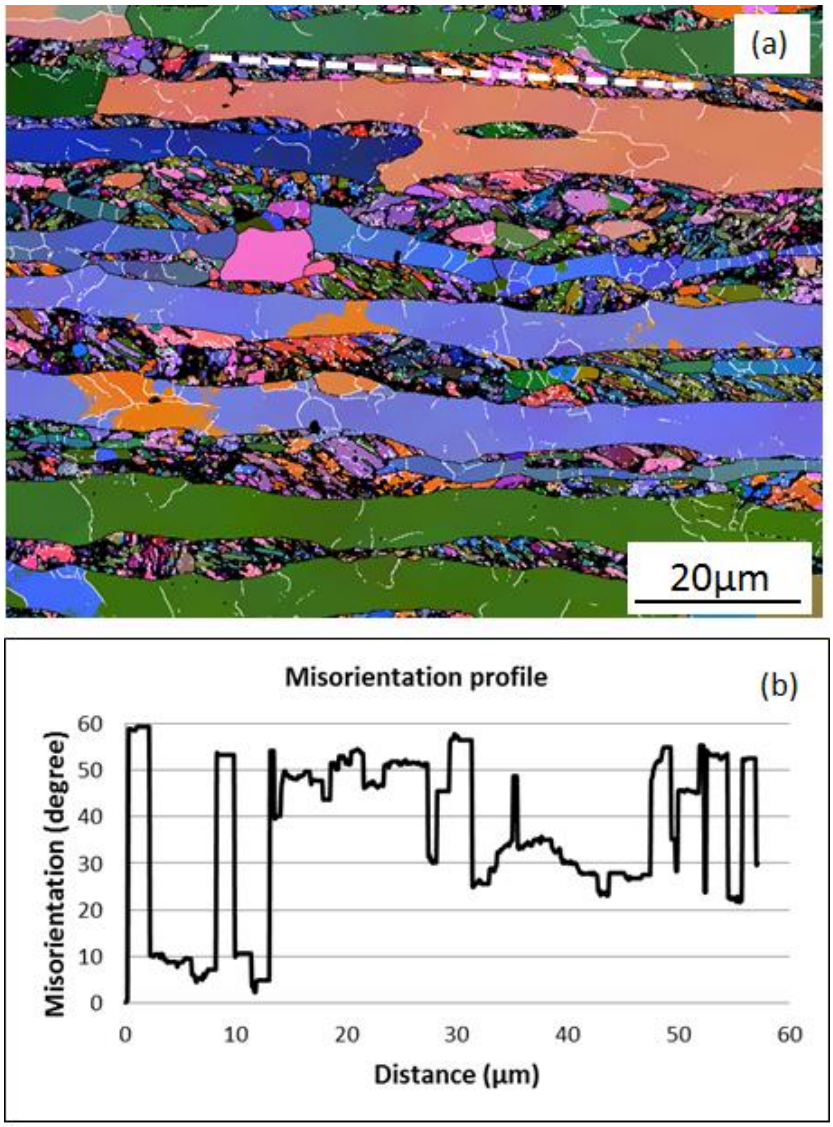

Figure 5.13: (a) EBSD Euler map of heat A after 3 consecutive steckel mill hot rolling process. (b) Misorientation profile of the martensite region of the microstructure in **Figure 5.13 (a)**.

5.3.1. Microstructure and texture evolution of heat A during martensite tempering heat treatment at 700˚C

Figure 5.14 (a) and **(b)** show the microstructure of heat A after martensite tempering heat treatment at 700˚C for 30 and 60 minutes respectively. The microstructures consist of primary ferrite bands and α'-martensite bands. The microstructures do not show a clear indication of the effect of the martensite tempering heat treatment when compared to the microstructure in

Figure 5.13 (a). However, there is some indication of grain boundary coalescence within the martensite regions when tempered for 60 minutes.

Figure 5.14 (c) and **(d)** show the $\varphi_2 = 45^\circ$ ODFs of the samples tempered at 700˚C for 30 and 60 minutes. The ODF in **Figure 5.14 (c)** shows that the martensite bands consisted of strong {001}<110> and weak {111}<110> and {111}<112> texture components after tempering at 700˚C for 30 minutes. However, **Figure 4.7** shows that after quenching from the third pass deformation temperature, the martensite bands (prior austenite regions) consisted of strong {001}<110>, {111}<110> and {111}<112>. On the other hand, the ODF in **Figure 5.14 (d)** shows that the martensite bands consisted of strong {001}<110>, {111}<110> and {111}<112> texture components after tempering at 700˚C for 60 minutes in comparison to the ODF in **Figure 5.14 (c)** for tempering at the same temperature for 30 minutes. Given that there is very little indication of martensite tempering at 700˚C for 30 minutes from the appearance of the orientation map in **Figure 5.14 (a)**, one would expect little change in the texture compared to the as-quenched condition. Consequently the difference in texture strength might be related to the sample size in Figure 3.14 (a) and the quality of the EBSD map. It should be noted that the EBSD map field of view for the martensite tempering study was much smaller than the field of view for the austenite to ferrite study in order to increase resolution to detect the fine martensitic structure.

5.3.2. Microstructure and texture evolution of heat A during martensite tempering heat treatment at 800˚C

Figure 5.15 (a) and **(b)** show the microstructures of heat A after martensite tempering heat treatment at 800˚C for 30 and 60 minutes respectively. The microstructure in **Figure 5.15 (a)** consists of bands of primary ferrite and martensite. Tempering for 30 minutes at 800˚C has had minimal effect on the martensite microstructure morphology when compared to the microstructure of the as quenched sample in **Figure 5.13 (a)**.

Figure 5.15 (b) shows the microstructure of heat A after martensite tempering heat treatment for 60 minutes. In this case there is much greater indication of grain boundary coalescence in the martensite regions giving rise to the classic polygonised ferrite morphology that one would expect in an advanced tempered martensite microstructure.

Figure 5.16 shows the misorientation profile across the polygonised ferrite grains (indicated by the white dotted line in **Figure 5.15 (b)** after martensite tempering heat treatment at 800˚C for 60 minutes. The misorientation range is again consistent with the K-S orientation relationship. However, the EBSD study has not been sufficiently exhaustive to detect the influence of grain coalescence (coarsening) on the orientation relationship.

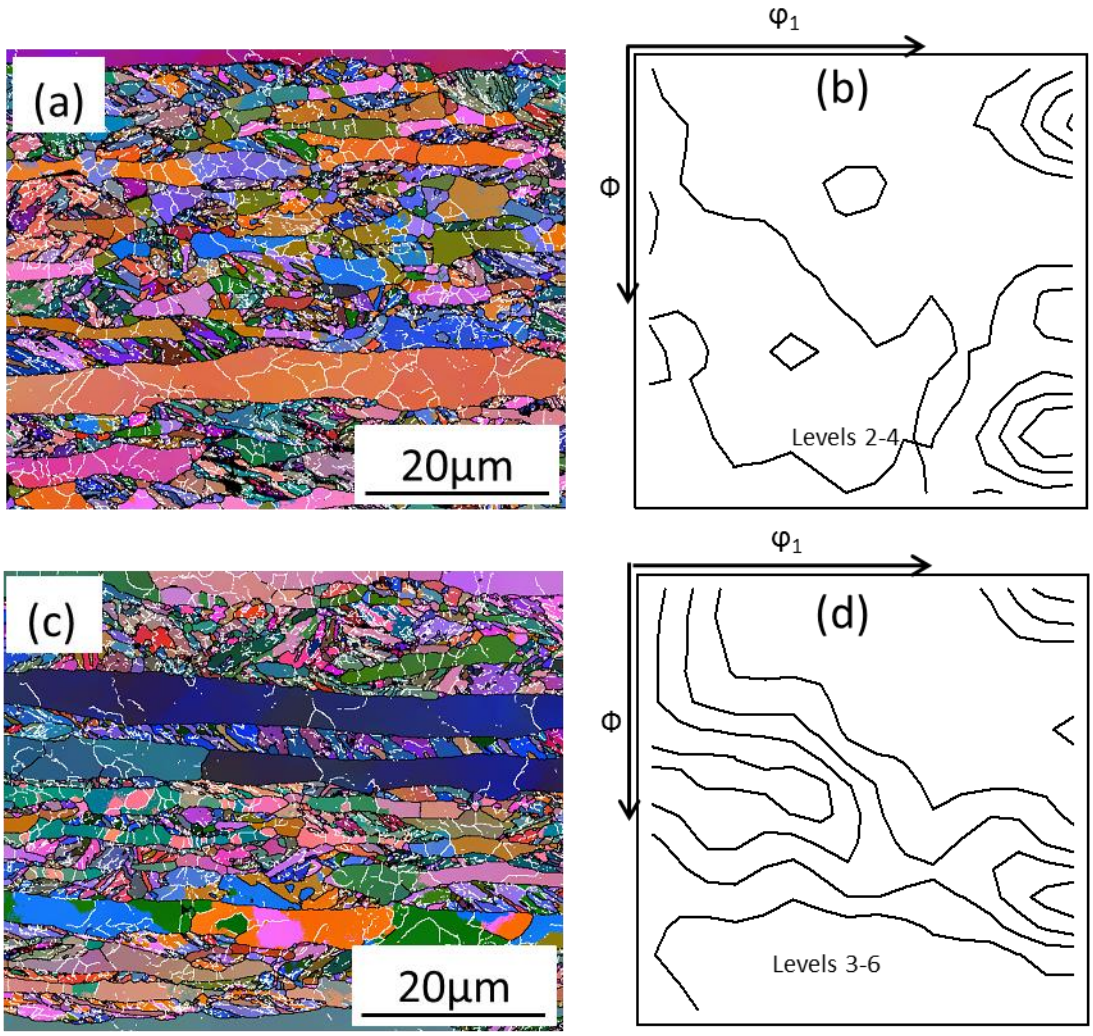

Figure 5.14: EBSD Euler maps after martensite tempering heat treatment at 700˚C for (a) 30 and (b) 60 minutes. ODFs at φ_2 = 45˚ of the microstructures tempered at 700˚C for (c) 30 and (d) 60 minutes.

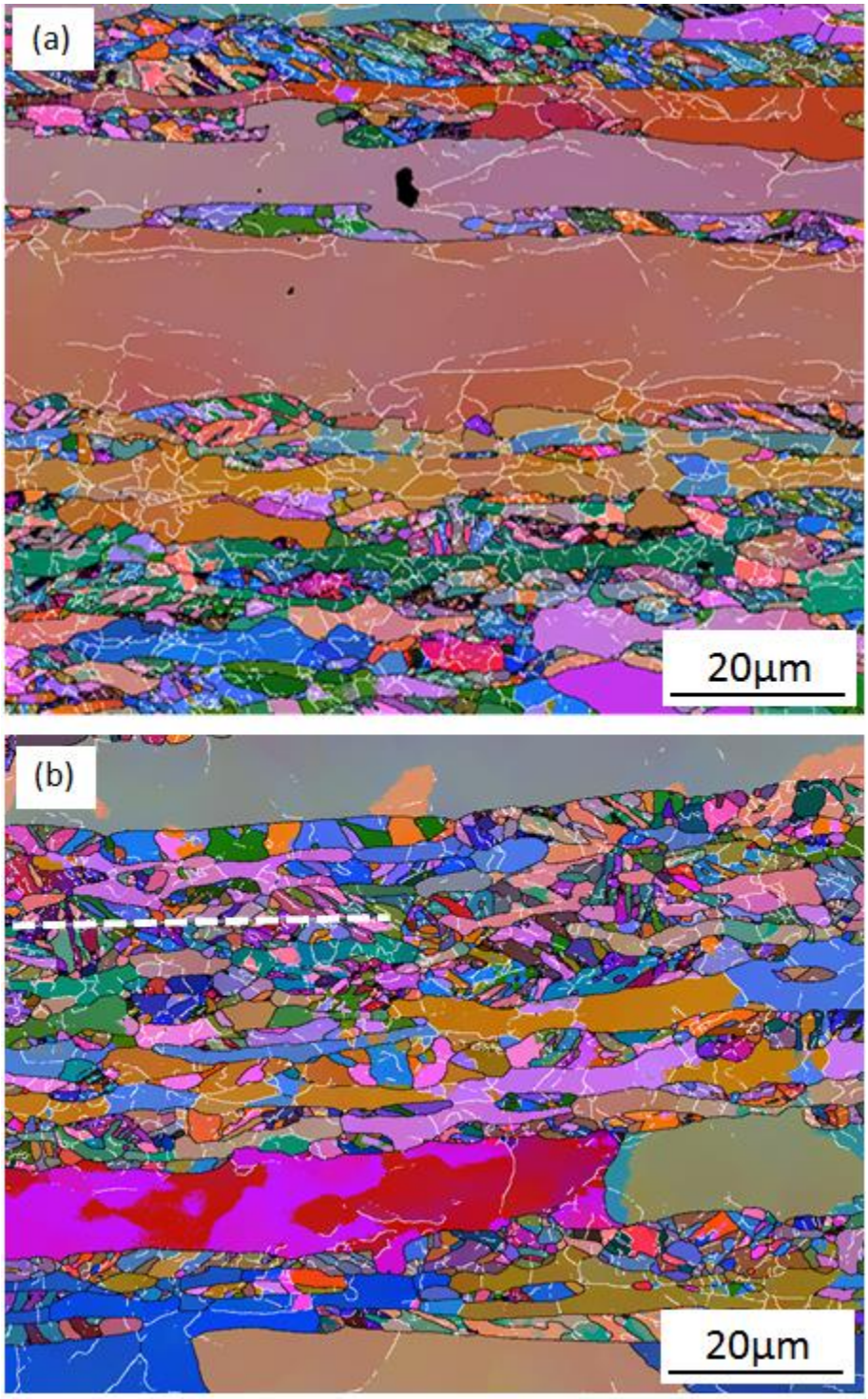

Figure 5.15: EBSD Euler map after martensite tempering heat treatment at 800˚C for (a) 30 and (b) 60 minutes.

(a)

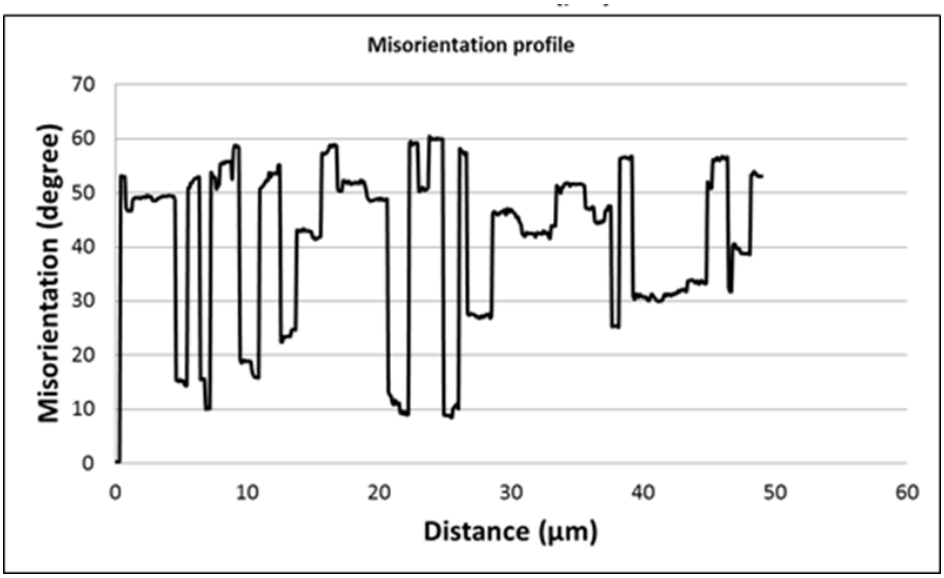

Figure 5.16: Misorientation profiles of the sample tempered at 800˚C for 60 minutes (see dotted line in Fig. 5.15(b)).

Figure 5.17 (c) and (d) show the $\varphi_2 = 45^\circ$ ODF after martensite tempering heat treatment at 800˚C for 30 and 60 minutes, respectively. The ODF in **Figure 5.17 (c)** shows that martensite tempering for 30 minutes at 800˚C weakened the α-fiber texture components and strengthened the γ-fiber texture components in the martensite (prior austenite) regions. Although, the microstructure in **Figure 5.15 (a)** did not show a significant effect of the martensite tempering heat treatment on the martensite regions, the ODF shows that there was a change in the texture of the martensite regions. **Figure 5.17 (a)** shows the ODFs of the deformed microstructure before the martensite tempering heat treatment. The ODF shows that the prior austenite regions consisted of strong {001}<110> and {111}<112> texture components. However, martensite tempering for 30 minutes at 800˚C weakened the {001}<110> and strengthened the {111}<112> and {111}<110> texture components. **Figure 5.17 (c)** also shows that the martensite tempering heat treatment at 800˚C for 30 minutes strengthened the {001}<110> and weakened the {111}<112> and {111}<110> texture components in the primary ferrite regions when compared to the texture components in **Figure 5.17 (a)**

Figure 5.17 (d) shows the $\varphi_2 = 45^\circ$ ODFs of martensite tempered sample at 800˚C for 60 minutes. The ODFs show that martensite tempering for longer than 30 minutes continued to weaken the {111}<112> and {111}<110> texture components in the primary ferrite regions. Again one must

be careful of placing too much emphasis on this interpretation because the high resolution EBSD map presents a small data sample, especially for the large elongated ferrite grains. However, the texture components in the martensite regions show similar intensities to that of the sample deformed and quenched to room temperature in **Figure 5.17 (a)** with a well defined γ-fiber texture. It is noted that the intensity of the {001}<110> increased with increasing tempering time, which could possibly be related to growth selection of this particular orientation component.

Figure 5.17 (b) shows that continuous phase transformation at 800˚C for 30 minutes weakened the {111}<112> and {111}<110> texture components in the primary ferrite and the prior austenite regions when compared to texture components in **Figure 5.17 (a).** However, the ODF in **Figure 5.17 (b)** indicate that there is a strong {001}<110> in the prior austenite regions when compared to **Figure 5.17 (a), (c)** and **(d)**.

5.3.3 Comparison of the austenite to ferrite transformation versus the martensite to ferrite transformation

The differences in texture evolution as a result of the isothermal continuous phase transformation process and the quench and martensite temper process are best highlighted in **Figure 5.17**. The prominent γ-fiber texture which is evident in the prior austenite region in the quenched state (now martensite) is maintained during reheating (tempering) at 700˚C and 800˚C. Although the austenite state prior to quenching is not known, and the aspects of variant selection have not been closely studied in this work, the martensite texture is undoubtedly related to the K-S orientation relationship between austenite and martensite. There are no indications to suggest that the strain rate in the final hot roll pass has influenced the martensite texture. During tempering the martensite recovers and the resultant polygonised ferrite coarsens. Once again, it may be expected that some growth selection occurs during the tempering process but for the most part the γ-fiber texture remains and in fact becomes better defined. The microstructure that evolves is highlighted in **Figure 5.18 (a)** wherein the prior austenite regions consist of fine grained ferrite whose morphology still resembles lath and packet forms associated with the martensite transformation.

In the case of the austenite to ferrite diffusional transformation, the situation regarding texture development is quite different. **Figure 2.17 (b)** displays dominant α-fiber texture with particularly strong {001}<110> presence. The {110}<110> and {111}<110> components are much weaker and the {111}<112> component, unlike in the case of the tempered martensite, is virtually absent. As argued earlier in chapter 2, if the parent austenite phase is recrystallized then the sharper {001}<110> component is explained by variant selection during transformation from the austenite cube orientations. The fact that the other {110}<110> and {110}<001> components are weaker, and the γ-fiber texture has all but disappeared points to strong growth selection of the {001}<110> orientation as the isothermal annealing proceeds for longer times as proposed in [27]. Consequently the decomposition path for the parent austenite phase has significant impact on texture evolution and distribution in the AISI430 ferritic stainless steels and hence likely to affect formability in different ways.

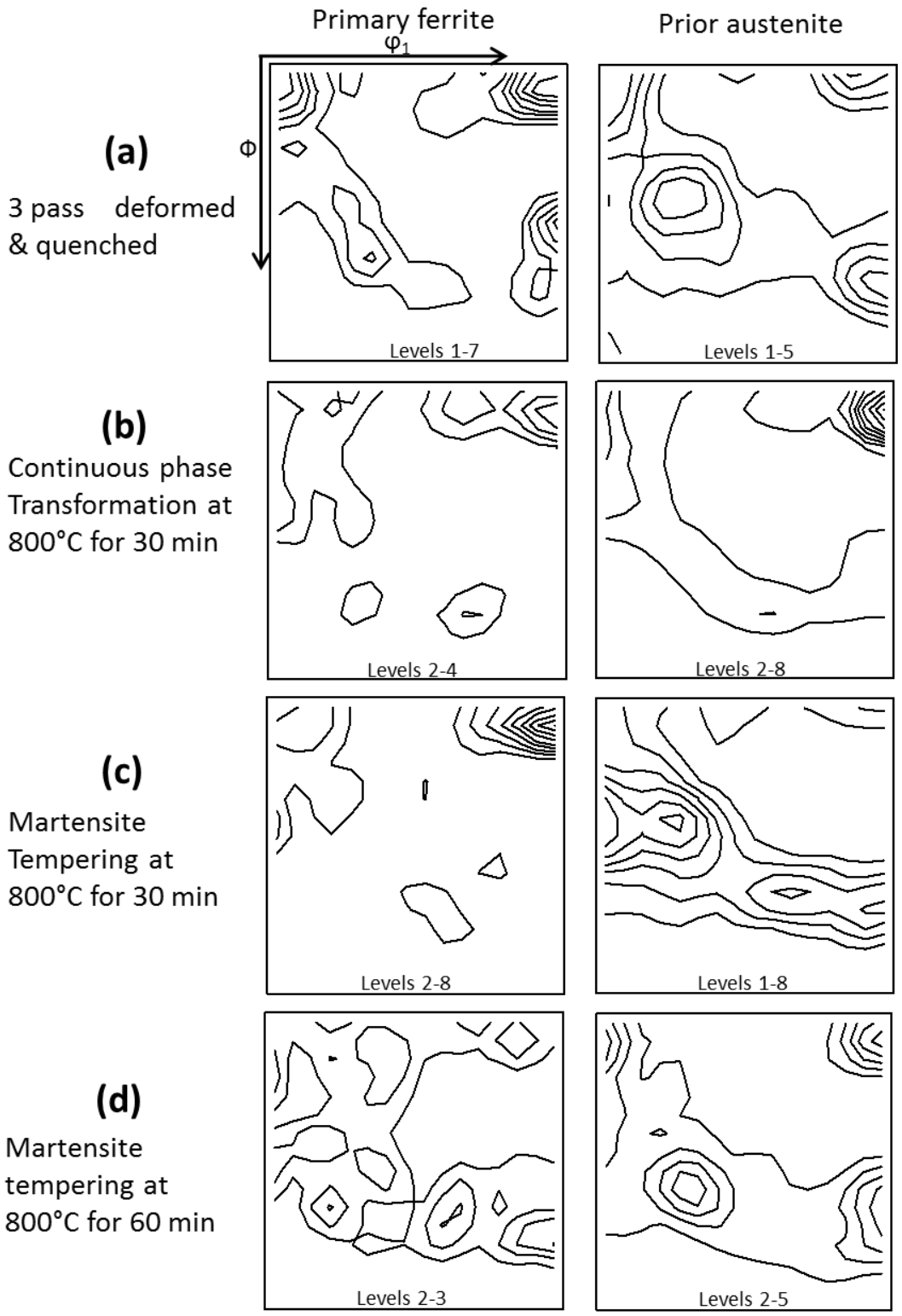

Figure 5.17: ODFs at φ_2 = 45˚in the primary ferrite and prior austenite regions after continuous phase transformation heat treatment and martensite tempering heat treatment at 800˚C.

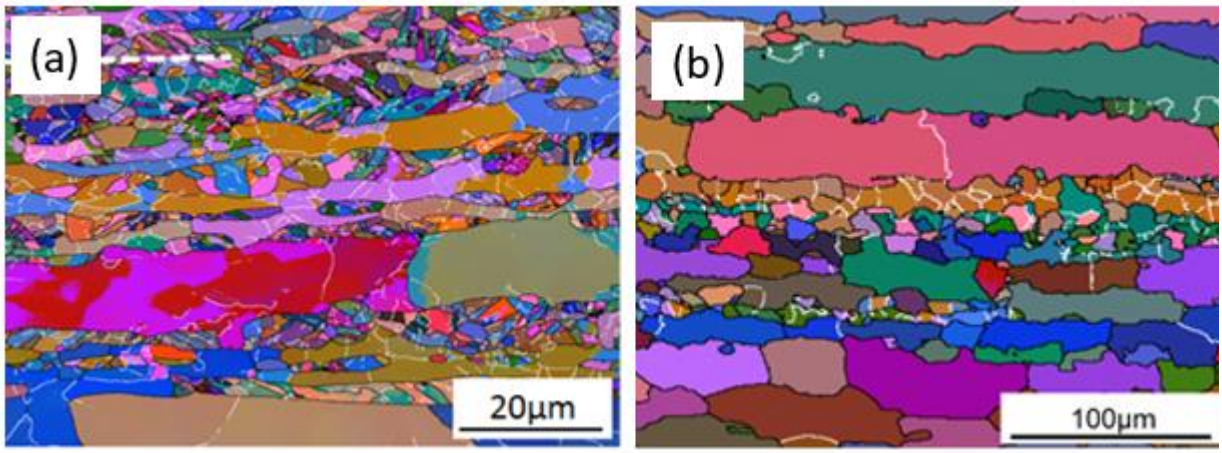

Figure 5.18: (a) Primary ferrite and polygonised ferrite (tempered martensite) microstructure evolved during the quench and martensite tempering process, and (b) primary ferrite and secondary ferrite microstructure.

6. CONCLUSIONS

i. The flow stress curves of heat A and B show similar trends, however, the flow stress values of heat A are higher than those of heat B values. This was due to the high austenite volume fraction in heat A during deformation.

ii. Austenite has a high strength compared to ferrite; therefore during deformation in the two phase temperature range, strain partitioning occurred in the primary ferrite grains seen by the presence of subgrains in the primary ferrite adjacent to the prior austenite regions. However, strain partitioning was not sufficient to initiate dynamic recrystallization in the primary ferrite grains.

iii. After three successive Steckel mill passes, heat A consisted of strong {001}<110> and {111}<112> in the martensite (prior austenite) and primary ferrite regions. Heat B consisted of strong {001}<110>, {112}<110> and weak {111}<112> texture components in the primary ferrite regions. The martensite (prior austenite) regions of heat B consisted of weak {001}<110>, and {111}<112> compared to heat A. Therefore, the high austenite volume fraction in heat A promoted the development of strong {111}<112> in the microstructure compared to heat B.

iv. Hot deformation at third pass strain rate of $80s^{-1}$ resulted in the development of strong {001}<110>, and {111}<112> texture components when compared to deformation at strain rate of $40s^{-1}$.

v. Continuous phase transformation heat treatment promoted the phase transformation of austenite to secondary ferrite, precipitation of carbides, as well as grain growth of the primary ferrite grains in both heat A and B. However, the kinetics of these processes were

influenced by the annealing time and temperature, strain rate and austenite volume fraction.

- Annealing time and temperature had a significant effect on the kinetics of the transformation, precipitation and grain growth when the samples were deformed a third pass strain rate of $40s^{-1}$. Complete phase transformation of austenite to secondary ferrite, carbide precipitation and grain growth of the primary ferrite grains occurred during the first 15 minutes of the annealing time at 800˚C. However, when annealing at 700˚C, these processes occurred after annealing for times longer than 15 minutes.
- The high austenite volume fraction in heat A promoted the occurrence of recovery in the primary ferrite grains.

vi. Texture development during continuous phase transformation heat treatment was also influenced by the annealing time and temperature, strain rate and austenite volume fraction.

- Annealing of the sample deformed at third pass strain rate of $40s^{-1}$ resulted in strengthening of the α and γ-fiber texture components. However, annealing for longer than 15 minutes weakened the γ-fiber texture components.
- Annealing of the sample deformed at third pass strain rate of $80s^{-1}$ at 700˚C resulted in weak and strong γ- and α-fiber texture components in the prior austenite regions respectively. However, the primary ferrite regions developed strong α and γ-fiber texture components during the annealing heat treatment at 700˚C. Annealing at 800˚C weakened the γ-fiber texture components in the primary ferrite while strengthening the α-finer texture.
- The high austenite volume fraction in heat A promoted the initial development of strong α and γ-fiber texture components compared to heat B but the γ-fiber texture significantly weakened with prolonged isothermal annealing.

vii. Martensite tempering heat treatment at 800˚C for 60 minutes resulted in the phase transformation of martensite to secondary ferrite. The prior austenite regions consisted of strong {001}<110> and {111}<112> texture components. However, the {001}<110> and {111}<112> texture components weakened in the primary ferrite regions after heat treatment at 800˚C for 60 minutes

viii. Although the martensite tempering heat treatment at 700˚C for 60 minutes did not have a significant effect on the microstructure, the γ-fiber texture became more uniform when compared to the microstructure prior to the martensite tempering heat treatment.

ix. Selection of the austenite decomposition process route has a highly significant influence on the texture development in the microstructural regions previously occupied by austenite. Variant and growth selection during continuous diffusional transformation from austenite to secondary ferrite promotes the occurrence of the {001}<110> rotated cube (45) component. In the case of the martensite tempering approach, the γ-fiber texture, particularly the {111}<112> component is strongly evident in the prior austenite regions.

x. The findings in this study suggest that there is a difference in microstructure evolution of heat A and heat B during deformation and subsequent annealing processes. Therefore, a comprehensive study which investigate the formability of the two heats would enable a recommendation as to which process or composition would provide the best formability.

7. REFERENCES

[1] O. Engler, M.Y. Huh and C. N. Tome, "Crystal-plasticity of ridging in ferritic stainless steel sheets," *Metallurgical and Materials Transactions A,* vol. 36A, pp. 3127-3139, 2005.

[2] H. Moo-Young, L. Jae-Hyup, H. P. Soo, E. Olaf and R. Dierk, "Effect of through thickness macro and micro-texture gradients on ridging of 17% Cr ferritic stainless steel sheet," *Steel Research International,* vol. 76, no. 11, pp. 797-806, 2005.

[3] J. Mola, I. Jung, J. Park, D. Chae and B. C. De cooman, "Ridging control in transformable ferritic stainless steels," *Metallurgical and Materials Transactions A,* vol. 43A, pp. 228-224, 2012.

[4] I. Tikhovskiy, D. Raabe and F. Roters, "Simulation of the deformation texture of a 17% Cr ferritic stainless steel using the texture component crystal plasticity finite element method considering texture gradients," *Scripta Materialia,* vol. 54, pp. 1537-1542, 2006.

[5] J.I. Hamada, N. Ono and H. Inoue, "Effect of texture on r-value of ferritic stainless steel sheets," *ISIJ International,* vol. 51, no. 10, pp. 1740-1748, 2011.

[6] H. Yan, H. Bi, X. Li and Z. Xu, "Microstructure, texture and grain boundaries character distribution evolution of ferritic stainless steel during rolling process," *Journal of Materials Processing Technology ,* vol. 209, pp. 2627-2631, 2009.

[7] R. D. Knutsen and N. J. Wittridge , "Modelling surface ridging in ferritic stainless steel," *Materials Science and Technology,* vol. 18, pp. 1279-1285, 2002.

[8] R. K. Ray and J. J. Jonas, "Transformation textures in steels," *International Matrials Review,* vol. 35, no. 1, pp. 1-36, 1990.

[9] F. B. Pickering, The metallurgical evolution of stainless steels, Ohio: American Society for Metals, 1979.

[10] J. Charles, J. D. Mithieux, P. O. Santacreu and L. Peguet, "The ferritic stainless steel family: the appropriate answer to nickel volatility?," *Revue de Metallurgie,* pp. 124-139, 2009.

[11] D. Peckner and I. M. Bernstein , Handbook of stainless steels, United States of America: McGraw-Hill, 1977.

[12] B. K. Jha, P. Jha and C. D. Singh, "Process technology for the continous hot band annealing of 17% Cr ferritic stainless steel," *JMEPEG,* vol. 11, pp. 180-186, 2002.

[13] J.I. Hamada, Y. Matsumoto, F. Fudanoki and S. Maeda, "Effect of initial solidified structure on ridging phenomenon and texture in type 430 ferritic stainless steel sheets," *ISIJ International,* vol. 43, no. 12, pp. 1989-1998, 2003.

[14] L. E. Collins, "Processing of niobium-containing steels by steckel mill rolling," 2001.

[15] S. Parker, "Microstructure evolution of AISI 304 stainless steel in the Steckel mill rolling process," 2004.

[16] Columbus Stainless , "Columbus Stainless," [Online]. Available: http://www.columbus.co.za/. [Accessed 21 June 2015].

[17] H.J. Shin, J.K. An, S. H. Park and N. L. Lee, "The effect of texture on ridging of ferritic stainless steel," *Acta Materialia,* vol. 51, pp. 4693-4706, 2003.

[18] L. K. S. Sudipta Patra, "Influence of hot band annealing and cold rolling on texture and ridging of 430 stainless steel containing aluminium," *Material Sciences and Applications,* vol. 4, pp. 70-76, 2013.

[19] M. Y. Huh and O. Engler, "Effect of intermediate annealing on texture, formability and ridging of 17% Cr ferritic stainless steel sheet," *Material Science and Engineering,* vol. A308, pp. 74-87, 2001.

[20] R. D. Knutsen, "Correlating microstructural features and surface roughening in ferritic stainless steel," *Material Science Forum,* vol. 550, pp. 65-74, 2007.

[21] R. K. Ray, J. J. Jonas, M. P. Butron-Guillen and J. Savoie, "Transformation textures in steels," *ISIJ International,* vol. 34, no. 12, pp. 927-942, 1994.

[22] J. J. Jonas, "Transformation textures associated with steel processing," in *Microstructure and texture in steel and other materials*, A. Haldar, S. Suwas and D. Bhattacharjee, Eds., Springer, 2009, pp. 3-17.

[23] M. Y. D. Raabe, "Experimental investigation of the transformation texture in hot rolled ferritic stainless steel using single orientation determination," *Metallurgical and Materials Transactions A,* vol. 27A, pp. 49-57, 1996.

[24] R. D. Knutsen, J. A. Basson and C. N. Machio, "The influence of austenite potential on the annealing behaviour of AISI 430 ferritic stainless steel".

[25] G. J. Davies, J. S. Kallend and P. P. Morris, *Acta Metallurgica,* vol. 24, p. 159, 1976.

[26] C. S. Da Costa Viana, M. P. Butro-Guillen and J. J. Jonas, "A variant selection model for the prediction of FCC-to-BCC transformation textures," *Textures and Microstrucutures ,* Vol. 26-27, pp. 599-610, 1996.

[27] J. Savoie, R. K. Ray, M. P. Butron-Gullen and J. J. Jonas, "Comparison between simulated and experimental transformation textures in a Nb microalloyed steel," *Acta Metallurgica et Materialia,* vol. 42, no. 7, pp. 2511-2523, 1994.

[28] M. P. Butron-Gullen, J. J. Jonas and R. K. Ray, "Effect of austenite pancaking on texture formation in plain carbon and a Nb microalloyed steel," *Acta Metallurgica et Materialia,* vol. 42, no. 11, pp. 3615-3627, 1994.

[29] M. E. Wahabi, J. M. Cabrera and J. M. Prado, "Hot working of two AISI 304 steels: a comparative study," *Material Science and Engineering A,* vol. 343, pp. 116-125, 2003.

[30] J. S. Hinton and J. H. Beynon, "Restoration process during hot deformation in the delta ferrite and austenite dual phase region of AISI 430 ferritic stainless steel," *ISIJ International,* vol. 47, no. 10, pp. 1465-1474, 2007.

[31] S. I. Kim and Y.C. Yoo, "Continous dynamic recrystallization of AISI 430 ferritic stainless steel," *Metals and Materials International,* vol. 8, no. 1, pp. 7-13, 2002.

[32] S. V. Mehtonen, E. J. Palmiere, R. D. Misra, L. P. Karjalainen and D. A. Porter, "Dynamic restoration mechanisms in a Ti-Nb stabilized ferritic stainless steel during hot deformation," *Materials Science & Engineering A,* vol. 601, pp. 7-19, 2014.

[33] D. Raabe and M. Ylitalo, "Experimental investigation of the transformation texture in the hot rolled ferritic stainless steel using single orientation determination," *Metallurgical and Materials Transactions A,* vol. 27A, pp. 49-57, 1996.

[34] F. J. Humphreys and M. Hatherly, Recrystallization and related annealing phenomena, 2 ed., Oxford: Elsevier, 2004.

[35] H. Kitahara, R. Ueji, N. Tsuji and Y. Minamino, "Crstallographic features of lath martensite in low-carbon steel," *Acta Materialia,* pp. 1279-1288, 2006.

8. APPENDICES

Appendix A: mill log data

Table A. 1: Steckel mill log data

Pass number	Segment Number	Entry Temperature (˚C)	Exit Temperature (˚C)	Entry Gauge (mm)	Exit Gauge (mm)	Arc length (mm)	Speed (mm/s)
1	0	-1.00	-1.00	-1.00	-1.00	99.00	1.83
1	1	-1.00	800.00	25.66	18.84	58.44	1.80
1	2	694.07	809.73	25.79	18.85	58.92	1.80
1	3	749.78	837.84	25.87	18.87	59.20	1.80
1	4	848.57	913.33	25.91	18.87	59.37	1.80
1	5	900.00	932.36	25.94	18.81	59.73	1.80
1	6	900.00	919.38	25.96	18.80	59.87	1.80
1	7	900.00	911.78	26.00	18.82	59.96	1.80
1	8	900.00	907.00	26.03	18.88	59.83	1.80
1	9	900.00	907.00	25.97	18.91	59.44	1.80
1	10	900.00	907.00	25.87	18.98	58.76	1.80
1	11	900.00	907.00	25.83	19.01	58.43	1.80
1	12	900.00	907.00	25.74	19.04	57.94	1.80
1	13	900.00	907.00	25.75	19.02	58.03	1.81
1	14	900.00	907.00	25.76	18.99	58.21	1.81
1	15	900.00	907.00	25.82	19.00	58.41	1.80
1	16	901.00	907.00	25.84	19.01	58.48	1.80
1	17	902.51	907.00	25.83	19.03	58.35	1.79
1	18	904.32	911.53	25.85	19.07	58.26	1.81
1	19	906.33	913.04	25.88	19.07	58.37	1.80
1	20	907.00	914.00	25.86	19.09	58.23	1.79
1	21	907.00	914.76	25.90	19.12	58.26	1.80
1	22	907.00	917.00	25.86	19.17	57.90	1.80
1	23	907.00	917.00	25.91	19.19	58.01	1.79
1	24	907.00	917.00	25.98	19.22	58.19	1.80
1	25	904.13	917.00	25.93	19.27	57.75	1.90
1	26	901.76	917.00	25.90	19.30	57.46	2.00
1	27	900.01	916.62	25.86	19.32	57.22	2.12
1	28	900.00	914.34	25.78	19.33	56.80	2.37
1	29	900.00	913.49	25.78	19.29	56.98	2.65
1	30	900.00	912.29	25.81	19.27	57.19	2.79
1	31	903.00	911.00	25.81	19.26	57.23	3.11
1	32	903.00	911.00	25.82	19.27	57.27	3.26
1	33	906.00	912.18	25.85	19.30	57.28	3.57
1	34	906.00	914.54	25.92	19.34	57.37	3.76
1	35	906.00	918.00	25.95	19.40	57.26	4.09
1	36	906.00	918.00	25.91	19.38	57.18	4.19
1	37	902.10	918.00	25.80	19.30	57.05	4.53

1	38	902.00	918.00	25.79	19.24	57.25	4.69
1	39	901.21	918.00	25.77	19.22	57.23	5.02
1	40	899.00	918.00	25.77	19.24	57.19	5.15
1	41	899.00	918.00	25.83	19.30	57.20	5.34
1	42	899.00	918.00	25.91	19.30	57.54	5.48
1	43	899.00	918.00	25.87	19.42	56.84	5.54
1	44	899.00	918.00	25.80	19.40	56.60	5.54
1	45	899.00	918.00	25.78	19.30	56.97	5.57
1	46	899.00	918.00	25.85	19.26	57.45	5.64
1	47	897.10	918.00	25.91	19.37	57.23	5.63
1	48	896.00	918.00	25.81	19.35	56.87	5.59
1	49	896.00	915.98	25.76	19.24	57.15	5.66
1	50	896.00	915.00	25.80	19.22	57.37	5.62
1	51	896.00	916.00	25.90	19.27	57.58	5.64
1	52	896.00	918.00	25.84	19.41	56.73	5.63
1	53	895.01	916.98	25.76	19.32	56.80	5.68
1	54	893.00	915.00	25.78	19.21	57.32	5.67
1	55	893.00	915.00	25.77	19.21	57.29	5.66
1	56	893.00	915.00	25.82	19.23	57.47	5.64
1	57	893.00	915.00	25.86	19.26	57.47	5.66
1	58	893.00	915.00	25.87	19.42	56.81	5.53
1	59	893.00	915.00	25.75	19.37	56.52	5.47
1	60	893.00	915.00	25.78	19.28	57.04	5.22
1	61	893.00	915.00	25.76	19.27	57.00	5.09
1	62	892.03	915.00	25.85	19.28	57.35	4.82
1	63	890.00	911.00	25.94	19.30	57.64	4.64
1	64	889.81	910.15	25.79	19.38	56.61	4.33
1	65	887.08	908.00	25.74	19.30	56.77	4.23
1	66	887.00	908.00	25.76	19.19	57.34	3.91
1	67	887.00	908.00	25.77	19.24	57.19	3.68
1	68	887.00	908.00	25.79	19.18	57.52	3.36
1	69	887.00	908.00	25.80	19.20	57.49	3.27
1	70	888.35	909.39	25.79	19.24	57.26	3.00
1	71	889.60	911.53	25.83	19.24	57.42	2.91
1	72	890.00	912.00	25.91	19.31	57.48	2.78
1	73	890.00	912.00	25.92	19.33	57.43	2.78
1	74	889.55	910.64	25.85	19.41	56.78	2.70
1	75	887.64	909.12	25.78	19.38	56.64	2.71
1	76	886.00	902.54	25.71	19.33	56.52	2.70
1	77	886.00	901.01	25.71	19.29	56.71	2.68
1	78	885.88	901.00	25.76	19.23	57.18	2.66
1	79	884.43	901.00	25.76	19.25	57.08	2.63
1	80	883.00	901.00	25.80	19.24	57.28	2.64
1	81	883.00	901.00	25.80	19.25	57.25	2.64
1	82	887.00	901.00	25.86	19.29	57.36	2.65
1	83	887.00	901.00	25.92	19.29	57.60	2.66
1	84	887.00	901.00	25.89	19.40	57.00	2.63
1	85	885.54	901.00	25.83	19.41	56.69	2.60
1	86	884.00	901.00	25.71	19.32	56.59	2.54
1	87	882.75	900.05	25.72	19.29	56.71	2.47

1	88	881.00	898.00	25.77	19.22	57.26	2.47
1	89	881.00	898.00	25.74	19.20	57.18	2.48
1	90	881.00	898.00	25.79	19.21	57.41	2.50
1	91	882.37	898.00	25.76	19.21	57.24	2.49
1	92	885.00	899.93	25.79	19.23	57.29	2.52
1	93	885.00	901.00	25.80	19.25	57.24	2.52
1	94	885.00	901.00	25.83	19.30	57.18	2.50
1	95	885.00	901.00	25.85	19.30	57.27	2.48
1	96	885.00	901.00	25.91	19.32	57.41	2.48
1	97	885.00	901.00	26.01	19.37	57.64	2.60
1	98	885.00	901.00	25.88	19.43	56.80	2.66
1	99	883.20	900.67	25.82	19.45	56.47	2.63
1	100	880.99	894.66	25.70	19.38	56.28	2.65
1	101	879.49	894.00	25.72	19.32	56.60	2.65
1	102	878.00	891.00	25.76	19.26	57.05	2.43
1	103	878.00	891.00	25.74	19.24	57.04	2.26
1	104	878.00	891.00	25.78	19.20	57.38	2.00
1	105	878.16	891.83	25.79	19.21	57.40	1.99
1	106	880.55	894.00	25.77	19.20	57.35	2.02
1	107	881.00	894.00	25.76	19.23	57.20	2.01
1	108	881.00	894.00	25.83	19.25	57.36	2.02
1	109	881.00	894.00	25.91	19.28	57.62	2.01
1	110	881.00	894.00	25.92	19.36	57.31	2.01
1	111	881.00	894.00	25.80	19.41	56.59	2.02
1	112	881.00	893.16	25.76	19.40	56.43	2.02
1	113	880.35	891.00	25.73	19.33	56.60	2.03
1	114	878.83	891.00	25.75	19.24	57.06	2.02
1	115	878.00	889.29	25.76	19.25	57.10	2.01
1	116	878.00	888.00	25.71	19.31	56.63	2.01
1	117	878.00	888.00	25.79	19.26	57.19	2.02
1	118	878.00	888.00	25.79	19.31	56.96	2.02
1	119	878.00	-1.00	25.77	-1.00	99.00	2.01
1	120	878.00	-1.00	25.75	-1.00	99.00	2.02
1	121	878.00	-1.00	0.00	-1.00	99.00	1.87
1	122	878.00	-1.00	0.00	-1.00	99.00	1.70
2	0.00	-1.00	-1.00	-1.00	-1.00	99.00	2.13
2	1.00	-1.00	-1.00	-1.00	-1.00	99.00	2.13
2	2.00	-1.00	640.67	-1.00	13.94	99.00	2.11
2	3.00	-1.00	686.53	-1.00	13.95	99.00	2.10
2	4.00	885.00	778.72	19.26	13.97	51.45	2.10
2	5.00	885.00	817.97	19.26	13.99	51.35	2.09
2	6.00	887.55	858.83	19.33	13.99	51.67	2.10
2	7.00	888.00	861.00	19.33	14.02	51.56	2.10
2	8.00	888.00	861.00	19.25	14.10	50.75	2.10
2	9.00	888.00	861.00	19.22	14.09	50.67	2.11
2	10.00	890.58	861.00	19.28	14.10	50.94	2.10
2	11.00	891.00	861.00	19.36	14.11	51.22	2.10
2	12.00	891.00	861.00	19.37	14.20	50.89	2.09
2	13.00	891.00	861.00	19.37	14.23	50.70	2.10
2	14.00	893.58	861.00	19.35	14.22	50.70	2.10

2	15.00	895.07	861.00	19.27	14.21	50.29	2.11
2	16.00	896.59	861.41	19.24	14.20	50.25	2.11
2	17.00	898.47	864.00	19.20	14.20	50.02	2.11
2	18.00	900.46	864.00	19.19	14.21	49.93	2.10
2	19.00	903.61	864.00	19.19	14.22	49.84	2.10
2	20.00	904.00	864.09	19.17	14.23	49.71	2.11
2	21.00	907.43	866.58	19.15	14.24	49.54	2.11
2	22.00	908.00	867.00	19.16	14.25	49.55	2.12
2	23.00	908.00	867.00	19.16	14.31	49.25	2.25
2	24.00	908.00	867.00	19.19	14.31	49.41	2.36
2	25.00	908.00	867.00	19.21	14.33	49.43	2.60
2	26.00	908.00	867.00	19.22	14.34	49.38	2.73
2	27.00	908.00	867.00	19.30	14.38	49.60	3.04
2	28.00	908.00	868.11	19.35	14.41	49.73	3.19
2	29.00	906.24	870.00	19.40	14.46	49.70	3.50
2	30.00	904.00	870.00	19.37	14.46	49.53	3.65
2	31.00	901.83	870.00	19.31	14.46	49.25	3.96
2	32.00	901.00	870.00	19.27	14.44	49.13	4.14
2	33.00	901.00	872.75	19.20	14.40	49.03	4.45
2	34.00	901.02	873.00	19.17	14.39	48.94	4.58
2	35.00	905.00	876.44	19.16	14.40	48.81	4.79
2	36.00	905.32	879.09	19.12	14.40	48.61	4.83
2	37.00	908.00	883.35	19.12	14.39	48.64	4.92
2	38.00	908.00	884.00	19.15	14.38	48.86	4.92
2	39.00	908.00	884.00	19.28	14.45	49.16	4.95
2	40.00	908.00	885.99	19.35	14.46	49.47	4.97
2	41.00	908.00	887.00	19.22	14.49	48.65	4.97
2	42.00	908.00	887.00	19.24	14.44	49.01	5.01
2	43.00	908.00	887.00	19.18	14.38	48.98	5.04
2	44.00	908.00	887.00	19.21	14.42	48.96	5.00
2	45.00	908.00	887.00	19.23	14.41	49.07	5.01
2	46.00	908.00	887.00	19.23	14.44	48.96	5.00
2	47.00	908.00	887.00	19.36	14.45	49.55	4.99
2	48.00	908.00	888.90	19.29	14.48	49.07	5.01
2	49.00	908.00	890.00	19.19	14.43	48.83	5.03
2	50.00	908.00	890.00	19.20	14.41	48.93	5.01
2	51.00	908.00	890.00	19.18	14.41	48.86	5.01
2	52.00	908.00	890.00	19.10	14.45	48.25	5.00
2	53.00	908.00	890.00	19.14	14.46	48.41	5.00
2	54.00	908.00	891.89	19.13	14.40	48.66	5.01
2	55.00	908.00	893.00	19.15	14.41	48.70	5.01
2	56.00	908.55	893.00	19.15	14.42	48.69	5.03
2	57.00	911.00	893.00	19.25	14.47	48.90	5.00
2	58.00	911.00	893.00	19.27	14.48	48.98	5.01
2	59.00	911.00	895.45	19.20	14.45	48.77	5.02
2	60.00	911.00	896.00	19.16	14.46	48.49	5.01
2	61.00	912.11	896.00	19.18	14.43	48.74	5.01
2	62.00	914.00	896.00	19.19	14.43	48.78	4.99
2	63.00	914.00	896.00	19.20	14.45	48.73	5.00
2	64.00	914.00	896.00	19.34	14.43	49.56	4.99

2	65.00	914.00	896.00	19.29	14.49	49.04	5.00
2	66.00	914.55	896.00	19.22	14.47	48.78	5.02
2	67.00	917.00	898.44	19.21	14.41	48.99	5.01
2	68.00	917.00	899.00	19.13	14.41	48.59	5.02
2	69.00	917.00	899.00	19.14	14.45	48.39	5.02
2	70.00	917.00	899.00	19.14	14.45	48.41	4.99
2	71.00	917.00	901.46	19.16	14.41	48.73	5.00
2	72.00	917.53	902.00	19.16	14.45	48.54	5.01
2	73.00	920.00	902.00	19.33	14.46	49.39	5.00
2	74.00	920.00	902.00	19.37	14.53	49.25	5.01
2	75.00	920.00	902.00	19.23	14.51	48.60	5.01
2	76.00	920.00	902.00	19.21	14.45	48.80	5.00
2	77.00	920.00	902.00	19.16	14.44	48.59	5.00
2	78.00	920.00	902.00	19.19	14.45	48.72	5.01
2	79.00	920.00	902.00	19.15	14.46	48.47	4.99
2	80.00	920.00	902.00	19.16	14.45	48.57	5.02
2	81.00	920.00	902.00	19.32	14.48	49.18	5.01
2	82.00	920.00	902.00	19.30	14.45	49.24	5.01
2	83.00	920.00	902.00	19.23	14.48	48.73	5.01
2	84.00	920.00	902.00	19.19	14.46	48.61	5.02
2	85.00	920.00	904.46	19.19	14.42	48.85	5.01
2	86.00	920.00	905.00	19.23	14.42	49.05	5.01
2	87.00	920.00	905.00	19.31	14.44	49.37	5.01
2	88.00	920.00	905.00	19.37	14.43	49.72	5.02
2	89.00	920.00	905.00	19.31	14.43	49.39	5.03
2	90.00	920.00	905.00	19.23	14.46	48.86	5.02
2	91.00	921.47	905.00	19.20	14.42	48.90	5.01
2	92.00	924.00	905.00	19.16	14.41	48.78	5.02
2	93.00	924.00	905.00	19.16	14.41	48.74	4.99
2	94.00	924.00	905.00	19.13	14.45	48.34	5.02
2	95.00	924.00	905.00	19.16	14.43	48.61	5.02
2	96.00	924.00	906.89	19.16	14.42	48.70	5.00
2	97.00	924.00	908.00	19.31	14.46	49.28	4.99
2	98.00	924.00	908.00	19.40	14.50	49.50	5.00
2	99.00	924.00	908.00	19.30	14.50	49.01	4.99
2	100.00	924.00	908.00	19.23	14.51	48.63	4.95
2	101.00	924.00	908.00	19.20	14.46	48.69	4.74
2	102.00	924.00	908.00	19.22	14.45	48.84	4.64
2	103.00	924.00	908.00	19.22	14.43	48.96	4.39
2	104.00	924.00	908.00	19.19	14.43	48.83	4.22
2	105.00	924.00	908.00	19.23	14.39	49.24	3.95
2	106.00	924.00	906.68	19.27	14.42	49.28	3.79
2	107.00	924.00	904.54	19.28	14.42	49.28	3.47
2	108.00	924.00	902.62	19.26	14.42	49.23	3.32
2	109.00	924.00	902.00	19.05	14.37	48.41	3.01
2	110.00	924.00	900.21	19.07	14.39	48.39	2.85
2	111.00	923.48	899.00	19.08	14.42	48.31	2.51
2	112.00	922.32	898.00	19.06	14.41	48.28	2.36
2	113.00	921.00	895.00	19.02	14.42	47.97	2.11
2	114.00	921.00	893.58	19.01	14.42	47.93	2.03

2	115.00	921.00	891.88	19.01	14.42	47.92	1.94
2	116.00	921.00	890.29	19.01	14.42	47.92	1.90
2	117.00	919.07	888.68	18.97	14.42	47.72	1.86
2	118.00	918.00	887.13	18.97	14.42	47.70	1.85
2	119.00	918.00	886.00	18.97	14.44	47.62	1.85
2	120.00	918.00	886.00	18.94	14.44	47.47	1.86
2	121.00	916.75	886.00	18.95	14.43	47.56	1.81
2	122.00	915.31	886.00	18.98	14.45	47.58	1.81
2	123.00	915.00	886.00	18.98	14.49	47.40	1.80
2	124.00	915.00	886.00	18.98	14.50	47.35	1.80
2	125.00	912.00	883.00	18.95	14.50	47.21	1.80
2	126.00	912.00	883.00	18.94	14.51	47.09	1.80
2	127.00	911.00	882.33	18.90	14.51	46.91	1.80
2	128.00	909.50	880.35	18.85	14.50	46.66	1.80
2	129.00	909.00	879.00	18.87	14.44	47.03	1.81
2	130.00	909.00	879.00	18.87	14.45	47.04	1.80
2	131.00	909.00	879.00	18.86	14.43	47.07	1.80
2	132.00	909.00	879.00	18.87	14.43	47.11	1.80
2	133.00	909.00	879.00	18.92	14.43	47.41	1.80
2	134.00	909.00	879.00	18.92	14.42	47.45	1.79
2	135.00	909.00	879.00	18.92	14.45	47.25	1.80
2	136.00	909.00	879.00	18.97	14.45	47.57	1.80
2	137.00	909.00	879.00	19.19	14.47	48.60	1.80
2	138.00	909.00	879.00	19.36	-1.00	99.00	1.80
2	139.00	908.01	-1.00	18.84	-1.00	99.00	1.79
2	140.00	906.50	-1.00	0.00	-1.00	99.00	1.81
2	141.00	903.00	-1.00	0.00	-1.00	99.00	1.62
3	0.00	-1.00	-1.00	-1.00	-1.00	99.00	1.97
3	1.00	-1.00	800.00	-1.00	9.46	99.00	2.12
3	2.00	-1.00	800.00	-1.00	9.35	99.00	2.09
3	3.00	878.09	800.00	14.46	9.25	51.02	2.08
3	4.00	876.00	805.27	14.45	9.29	50.85	2.10
3	5.00	876.00	885.78	14.71	9.31	52.00	2.11
3	6.00	876.00	923.92	15.06	9.31	53.65	2.09
3	7.00	876.00	896.10	14.79	9.33	52.29	2.11
3	8.00	873.40	886.00	14.48	9.33	50.76	2.10
3	9.00	873.00	886.00	14.43	9.39	50.23	2.09
3	10.00	870.45	886.00	14.43	9.39	50.23	2.11
3	11.00	870.00	885.58	14.41	9.39	50.12	2.10
3	12.00	870.00	883.00	14.42	9.38	50.24	2.10
3	13.00	870.00	883.00	14.42	9.37	50.26	2.11
3	14.00	870.00	883.00	14.42	9.38	50.21	2.10
3	15.00	872.79	883.00	14.44	9.40	50.19	2.11
3	16.00	873.00	883.00	14.42	9.39	50.19	2.11
3	17.00	875.79	883.47	14.42	9.42	50.02	2.11
3	18.00	876.00	886.00	14.44	9.43	50.05	2.10
3	19.00	878.78	886.18	14.41	9.45	49.85	2.10
3	20.00	879.00	887.58	14.42	9.46	49.82	2.09
3	21.00	879.00	889.00	14.40	9.46	49.72	2.09
3	22.00	879.00	889.00	14.40	9.46	49.70	2.10

3	23.00	879.00	889.45	14.34	9.48	49.32	2.13
3	24.00	882.00	891.79	14.31	9.49	49.08	2.31
3	25.00	882.00	892.00	14.32	9.51	49.05	2.54
3	26.00	882.00	892.00	14.30	9.52	48.89	2.69
3	27.00	885.00	894.74	14.31	9.55	48.80	2.96
3	28.00	885.00	895.00	14.32	9.55	48.85	3.12
3	29.00	885.00	896.33	14.31	9.56	48.71	3.39
3	30.00	885.00	898.47	14.32	9.57	48.78	3.55
3	31.00	885.00	901.00	14.28	9.58	48.52	3.89
3	32.00	885.00	901.00	14.28	9.57	48.51	4.03
3	33.00	888.79	904.57	14.25	9.55	48.47	4.35
3	34.00	889.02	907.08	14.25	9.56	48.46	4.50
3	35.00	892.00	910.28	14.27	9.57	48.48	4.82
3	36.00	892.48	911.00	14.27	9.60	48.35	4.99
3	37.00	895.00	913.64	14.27	9.63	48.18	5.32
3	38.00	896.12	915.79	14.25	9.63	48.08	5.50
3	39.00	901.15	919.80	14.23	9.63	48.01	5.78
3	40.00	902.00	921.00	14.24	9.63	48.04	5.84
3	41.00	904.44	923.29	14.28	9.63	48.25	5.95
3	42.00	905.00	925.00	14.32	9.67	48.26	6.00
3	43.00	905.00	926.69	14.30	9.69	48.05	6.05
3	44.00	906.30	928.00	14.30	9.66	48.18	6.07
3	45.00	908.00	929.69	14.33	9.65	48.42	6.06
3	46.00	909.30	931.00	14.35	9.65	48.48	6.08
3	47.00	911.00	931.00	14.33	9.68	48.24	6.11
3	48.00	911.00	931.00	14.31	9.69	48.09	6.13
3	49.00	911.00	932.67	14.27	9.68	47.90	6.13
3	50.00	912.32	934.00	14.25	9.67	47.87	6.11
3	51.00	914.00	934.00	14.30	9.67	48.10	6.11
3	52.00	914.00	934.00	14.31	9.68	48.14	6.12
3	53.00	914.00	934.00	14.30	9.69	48.02	6.12
3	54.00	914.00	934.00	14.28	9.68	48.01	6.12
3	55.00	914.00	935.68	14.29	9.66	48.13	6.12
3	56.00	914.00	937.00	14.29	9.67	48.10	6.11
3	57.00	914.00	937.00	14.32	9.67	48.19	6.12
3	58.00	914.00	937.00	14.28	9.68	47.99	6.12
3	59.00	914.00	937.00	14.29	9.68	48.01	6.12
3	60.00	914.00	937.00	14.29	9.70	47.93	6.14
3	61.00	914.00	937.00	14.27	9.70	47.82	6.12
3	62.00	914.00	937.00	14.29	9.69	47.96	6.11
3	63.00	914.00	937.00	14.32	9.70	48.07	6.12
3	64.00	914.00	937.00	14.36	9.70	48.31	6.10
3	65.00	914.00	937.00	14.37	9.70	48.33	6.12
3	66.00	914.00	937.00	14.34	9.69	48.22	6.13
3	67.00	914.00	937.00	14.33	9.69	48.19	6.11
3	68.00	914.00	937.00	14.29	9.69	47.96	6.12
3	69.00	914.00	937.00	14.30	9.69	48.06	6.11
3	70.00	914.00	935.32	14.32	9.70	48.09	6.13
3	71.00	914.00	934.00	14.30	9.71	47.96	6.11
3	72.00	914.00	934.00	14.30	9.70	47.97	6.11

3	73.00	914.00	934.00	14.32	9.68	48.18	6.13
3	74.00	914.00	934.00	14.39	9.68	48.54	6.13
3	75.00	914.00	934.00	14.37	9.70	48.33	6.11
3	76.00	914.00	934.00	14.29	9.69	48.01	6.11
3	77.00	914.00	934.00	14.30	9.67	48.09	6.12
3	78.00	914.00	934.00	14.28	9.68	48.02	6.12
3	79.00	914.00	934.00	14.29	9.69	47.98	6.11
3	80.00	914.00	934.00	14.32	9.71	47.99	6.11
3	81.00	914.00	934.00	14.30	9.71	47.88	6.11
3	82.00	914.00	934.00	14.30	9.71	47.92	6.12
3	83.00	914.00	934.00	14.30	9.71	47.97	6.15
3	84.00	914.00	934.00	14.31	9.70	48.02	6.14
3	85.00	914.00	934.00	14.33	9.71	48.07	6.11
3	86.00	911.33	934.00	14.35	9.71	48.21	6.12
3	87.00	911.00	934.00	14.36	9.70	48.24	6.12
3	88.00	911.00	933.67	14.33	9.69	48.16	6.12
3	89.00	911.00	931.00	14.31	9.66	48.20	6.12
3	90.00	911.00	931.00	14.30	9.68	48.08	6.12
3	91.00	911.00	931.00	14.31	9.70	48.05	6.12
3	92.00	911.00	931.00	14.32	9.70	48.09	6.10
3	93.00	911.00	929.34	14.31	9.67	48.19	6.11
3	94.00	909.66	928.00	14.34	9.69	48.26	6.14
3	95.00	908.00	928.00	14.32	9.71	48.02	6.12
3	96.00	908.00	928.00	14.29	9.70	47.90	6.10
3	97.00	908.00	928.00	14.27	9.68	47.92	6.12
3	98.00	908.00	928.00	14.28	9.69	47.91	6.13
3	99.00	908.00	928.00	14.29	9.70	47.90	6.12
3	100.00	908.00	928.00	14.31	9.70	47.99	6.11
3	101.00	905.33	928.00	14.28	9.68	47.96	6.10
3	102.00	905.00	928.00	14.28	9.68	47.94	6.13
3	103.00	905.00	928.00	14.27	9.69	47.86	6.11
3	104.00	905.00	928.00	14.29	9.69	47.96	6.11
3	105.00	905.00	926.34	14.32	9.70	48.09	6.13
3	106.00	905.00	925.00	14.33	9.69	48.17	6.12
3	107.00	905.00	925.00	14.31	9.70	48.04	6.11
3	108.00	903.66	925.00	14.30	9.69	48.02	6.13
3	109.00	902.00	925.00	14.29	9.69	48.00	6.13
3	110.00	902.00	924.67	14.29	9.68	48.03	6.12
3	111.00	902.00	922.00	14.30	9.68	48.05	6.12
3	112.00	902.00	922.00	14.30	9.68	48.05	6.12
3	113.00	902.00	922.00	14.34	9.68	48.27	6.12
3	114.00	902.00	922.00	14.36	9.70	48.31	6.12
3	115.00	902.00	922.00	14.34	9.69	48.23	6.13
3	116.00	900.68	922.00	14.31	9.67	48.18	6.10
3	117.00	899.00	920.33	14.27	9.66	48.00	6.11
3	118.00	899.00	919.00	14.27	9.68	47.95	6.12
3	119.00	899.00	919.00	14.23	9.68	47.70	6.12
3	120.00	899.00	919.00	14.23	9.68	47.69	6.11
3	121.00	899.00	919.00	14.26	9.69	47.80	6.10
3	122.00	899.00	919.00	14.25	9.69	47.77	6.06

3	123.00	896.55	917.08	14.27	9.67	48.02	5.84
3	124.00	896.00	916.00	14.31	9.69	48.12	5.77
3	125.00	896.00	916.00	14.36	9.69	48.34	5.46
3	126.00	895.04	916.00	14.36	9.69	48.35	5.34
3	127.00	893.00	912.58	14.33	9.67	48.31	5.04
3	128.00	893.00	912.00	14.28	9.68	47.95	4.90
3	129.00	892.16	909.00	14.24	9.65	47.88	4.57
3	130.00	890.00	908.72	14.22	9.66	47.77	4.42
3	131.00	890.00	905.00	14.18	9.65	47.61	4.10
3	132.00	890.00	905.00	14.17	9.65	47.59	3.97
3	133.00	887.54	902.00	14.15	9.60	47.67	3.62
3	134.00	886.46	900.59	14.10	9.62	47.35	3.31
3	135.00	885.17	899.00	14.09	9.60	47.39	3.15
3	136.00	884.00	898.65	14.09	9.60	47.37	2.98
3	137.00	884.00	896.00	14.09	9.60	47.39	2.65
3	138.00	884.00	895.79	14.09	9.59	47.47	2.51
3	139.00	884.00	892.00	14.06	9.61	47.21	2.22
3	140.00	882.98	892.00	14.05	9.60	47.23	2.11
3	141.00	881.00	889.00	14.08	9.59	47.41	1.99
3	142.00	881.00	889.00	14.09	9.59	47.48	1.93
3	143.00	881.00	886.00	14.12	9.61	47.50	1.87
3	144.00	880.43	885.75	14.13	9.64	47.39	1.85
3	145.00	878.60	883.00	14.10	9.63	47.27	1.85
3	146.00	877.00	883.00	14.06	9.65	46.99	1.84
3	147.00	877.00	880.00	14.01	9.66	46.68	1.82
3	148.00	877.00	880.00	14.01	9.65	46.69	1.80
3	149.00	877.00	878.23	13.99	9.65	46.63	1.80
3	150.00	877.00	877.00	13.99	9.65	46.60	1.80
3	151.00	877.00	877.00	13.97	9.65	46.54	1.80
3	152.00	877.00	877.00	14.01	9.65	46.70	1.80
3	153.00	877.00	877.00	14.08	9.65	47.07	1.80
3	154.00	877.00	877.00	14.00	9.67	46.54	1.80
3	155.00	875.76	877.00	13.95	9.71	46.08	1.80
3	156.00	874.27	877.00	13.93	9.73	45.88	1.81
3	157.00	874.00	877.00	13.92	9.70	45.97	1.80
3	158.00	874.00	877.00	13.94	9.69	46.12	1.80
3	159.00	874.00	874.67	13.97	9.67	46.37	1.80
3	160.00	874.00	873.00	13.97	9.67	46.40	1.81
3	161.00	875.65	873.00	13.98	9.66	46.45	1.80
3	162.00	877.66	873.00	13.99	9.67	46.49	1.79
3	163.00	878.00	873.37	14.03	9.68	46.62	1.80
3	164.00	880.48	877.00	14.19	9.69	47.46	1.80
3	165.00	881.00	877.00	14.62	9.74	49.38	1.79
3	166.00	881.00	877.00	13.99	-1.00	99.00	1.80
3	167.00	878.96	-1.00	0.00	-1.00	99.00	1.80
3	168.00	876.44	-1.00	0.00	-1.00	99.00	1.81
3	169.00	726.00	-1.00	0.00	-1.00	99.00	1.62
3	170.00	-1.00	-1.00	0.00	-1.00	99.00	1.35

Appendix B: steckel mill hot rolling process

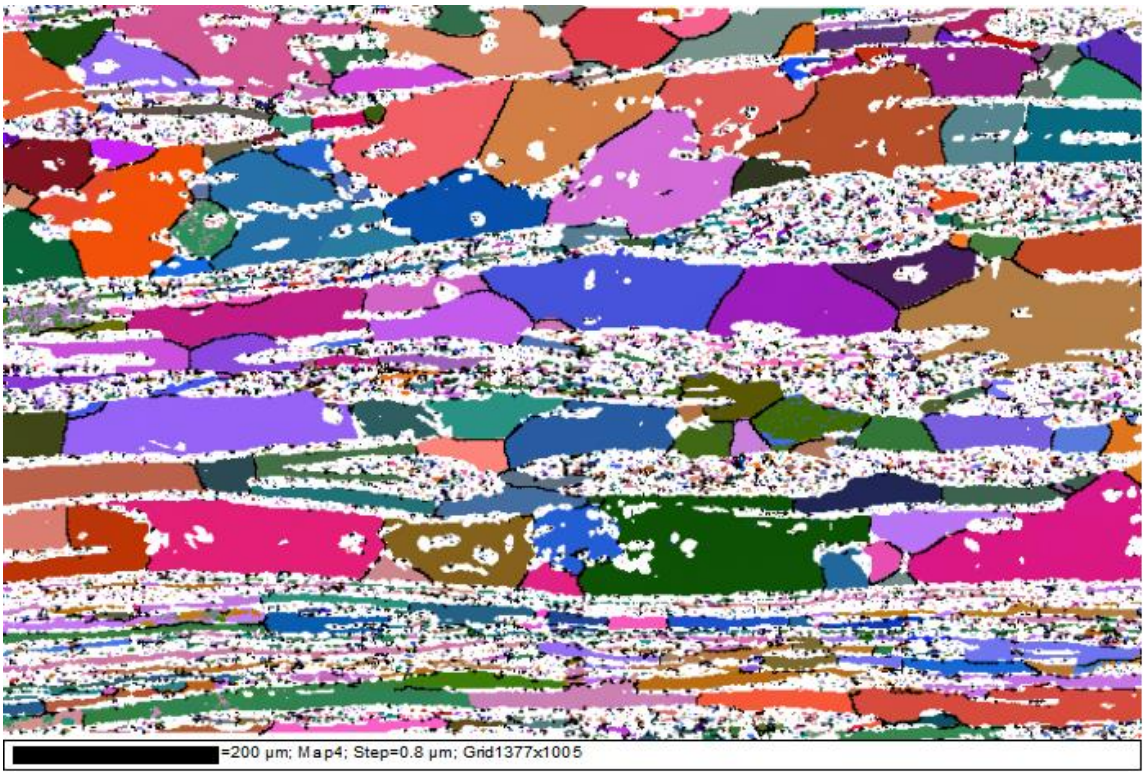

Figure B. 1: EBSD Euler map of heat A after pre-deformation heat treatment

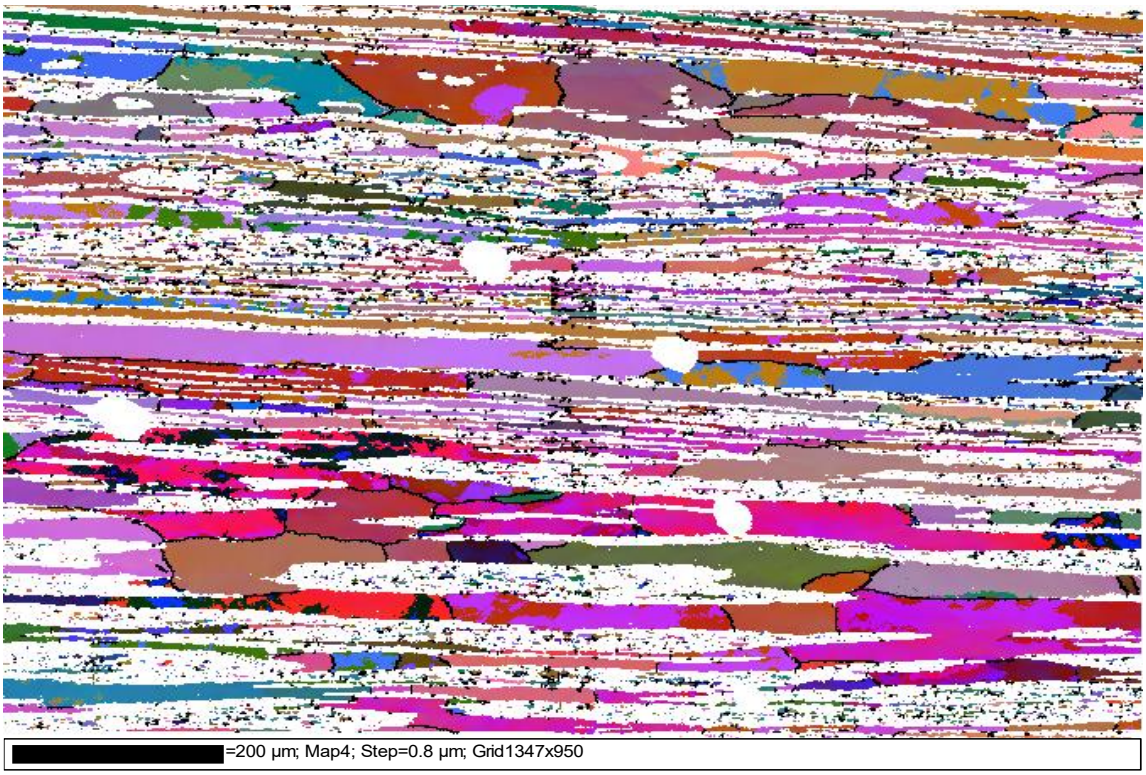

Figure B. 2: EBSD Euler map of heat A after 1 pass deformation

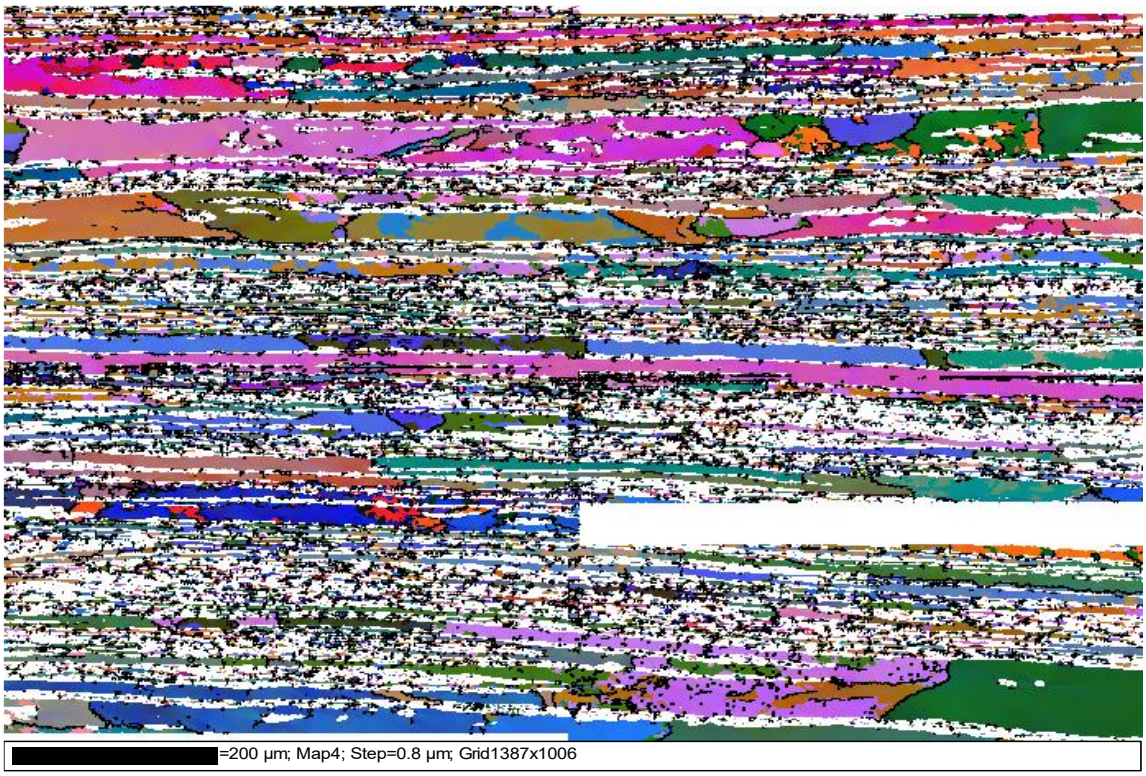

Figure B. 3: EBSD Euler map of heat A after 2 pass deformation.

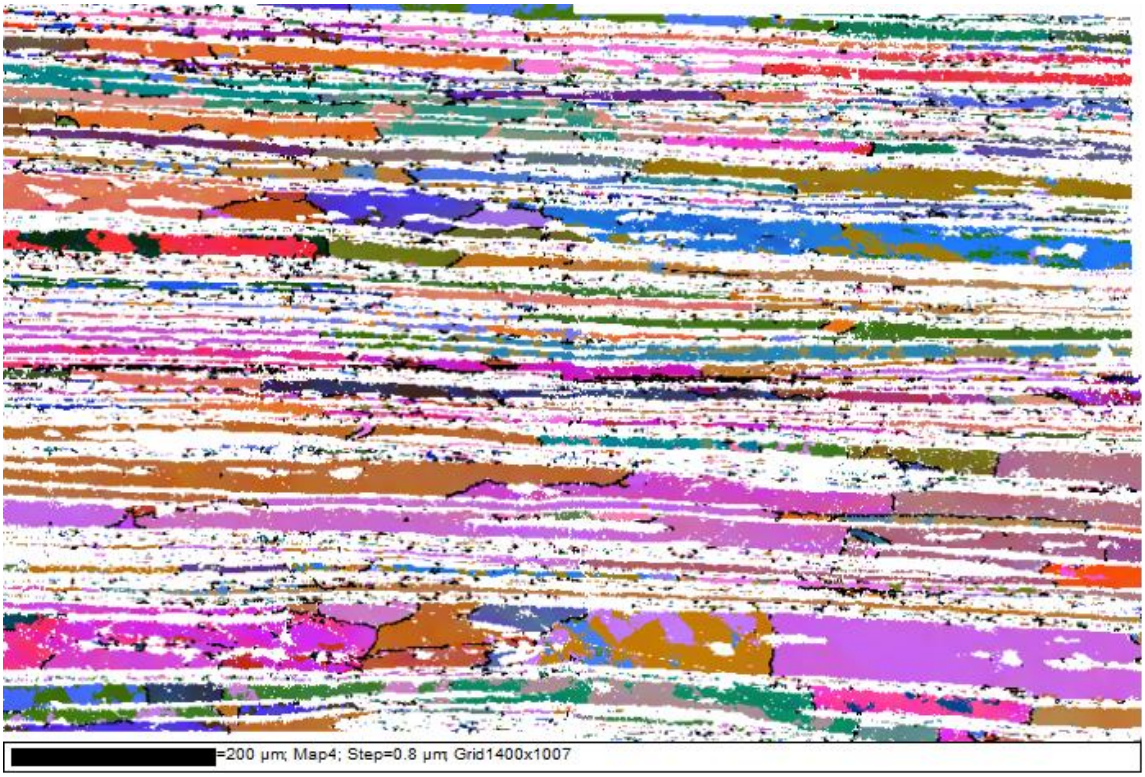

Figure B. 4: EBSD Euler map of heat A after 3 pass deformation, 3rd pass strain rate = $80s^{-1}$.

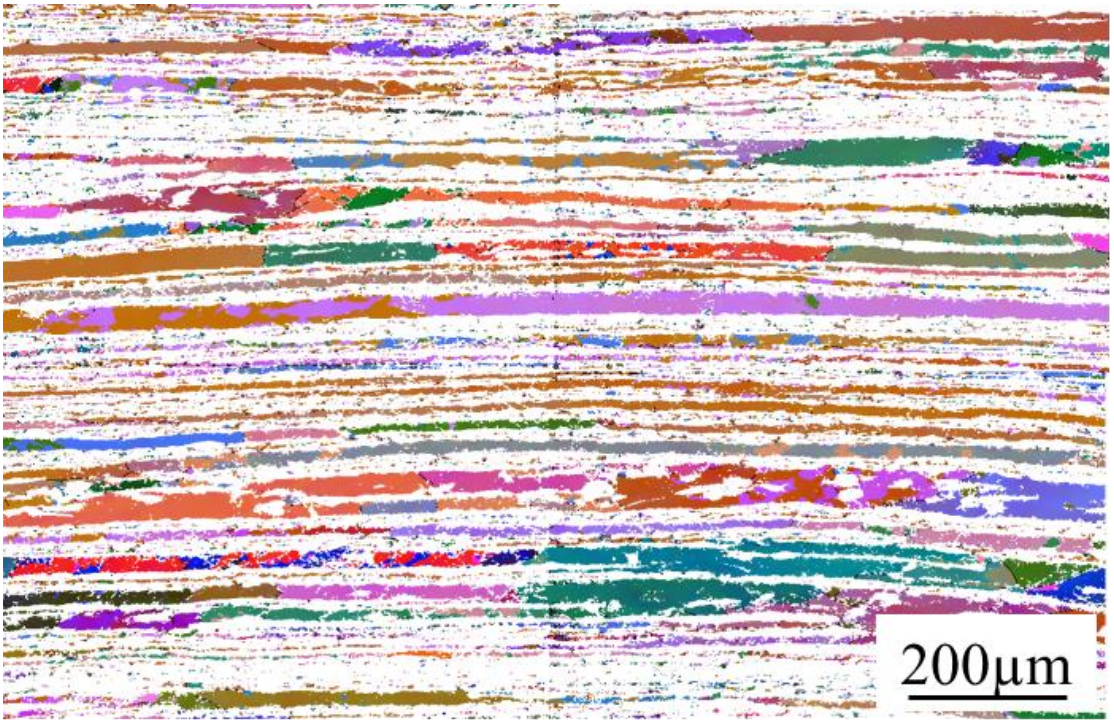

Figure B. 5: EBSD Euler map of heat A after 3 pass deformation, 3rd pass strain rate = $40s^{-1}$.

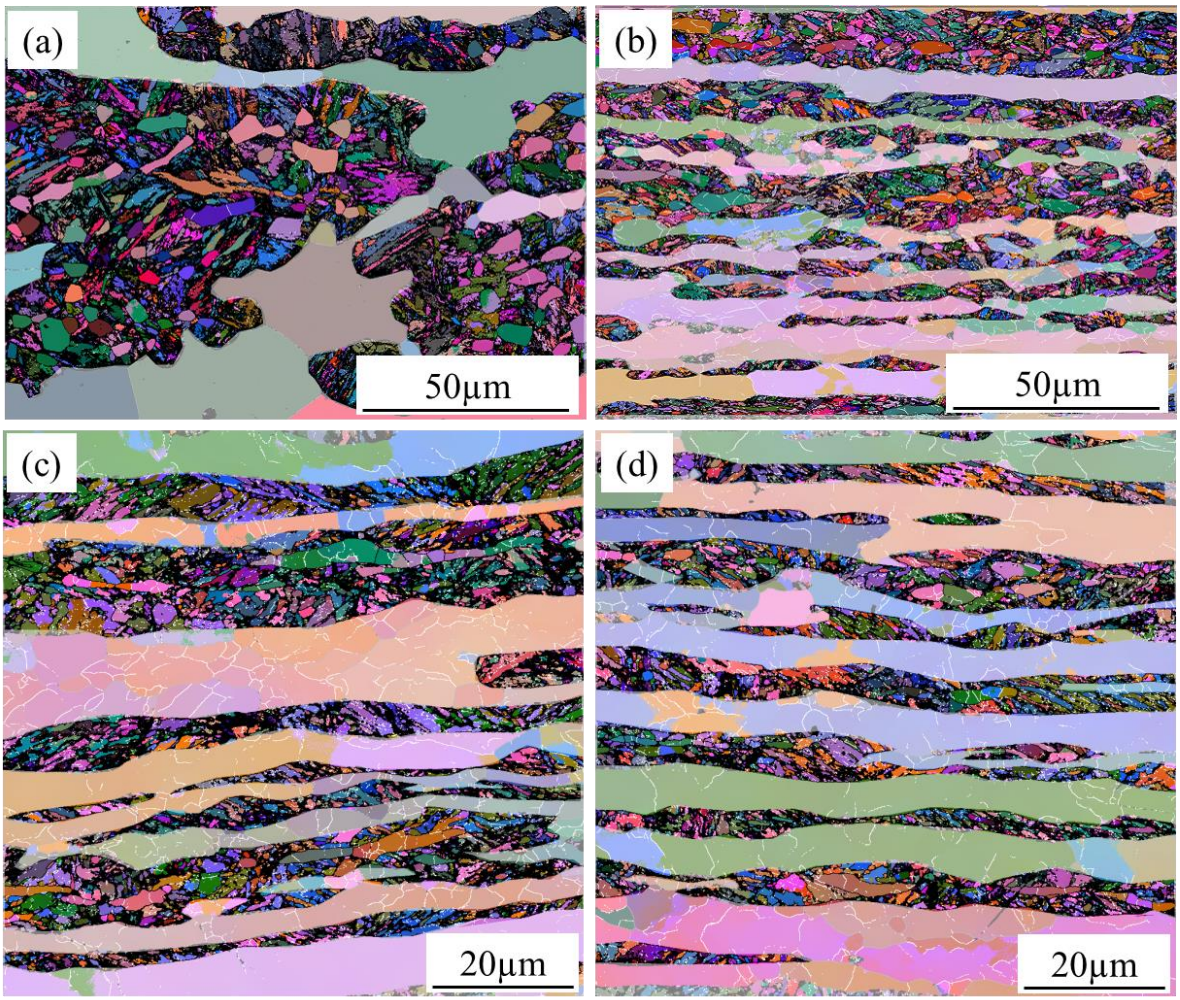

Figure B. 6: EBSD Euler map of heat A after (a) pre-deformation heat treatment, (b) 1 pass, (c) 2 passes and (d) 3 passes where the 3rd pass strain rate = 80s^{-1}. The prior austenite regions are highlighted.

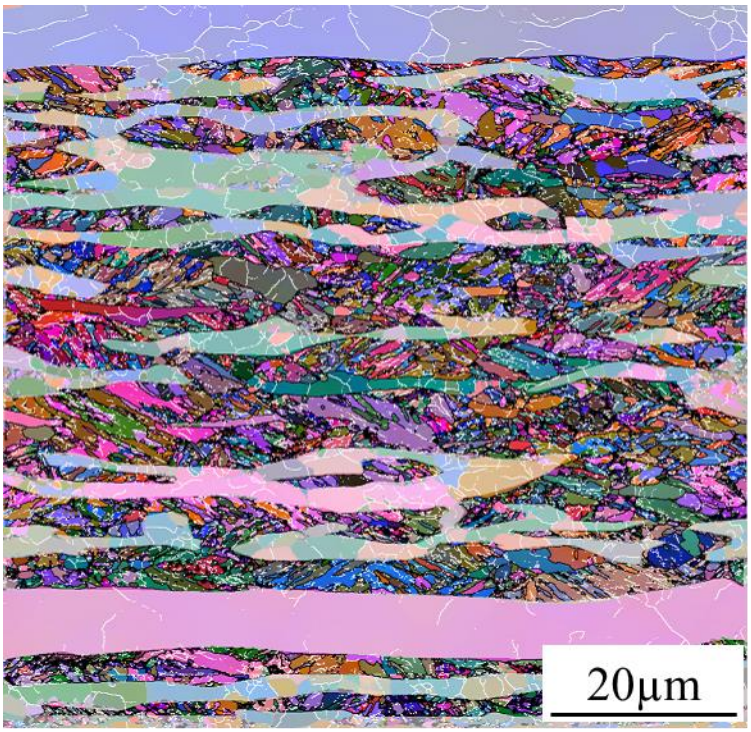

Figure B. 7: EBSD Euler map of heat A after 3 passes where the 3rd pass strain rate = $40s^{-1}$.

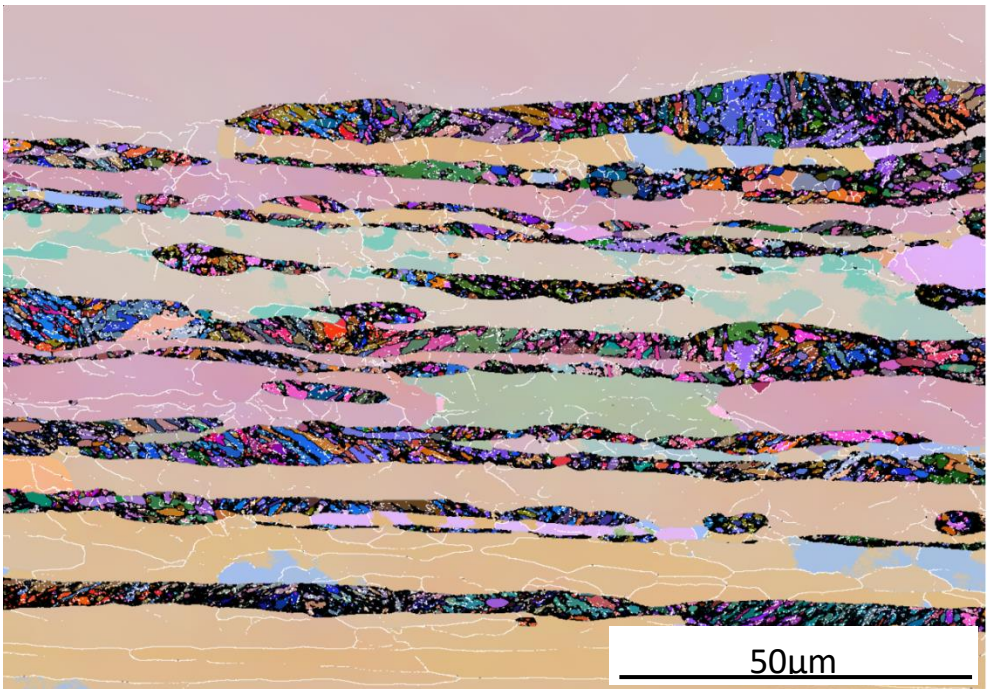

Figure B. 8: EBSD Euler map of heat B after 3 passes where the 3rd pass strain rate = $80s^{-}.^{1}$

Appendix C: continuous phase transformation heat treatments

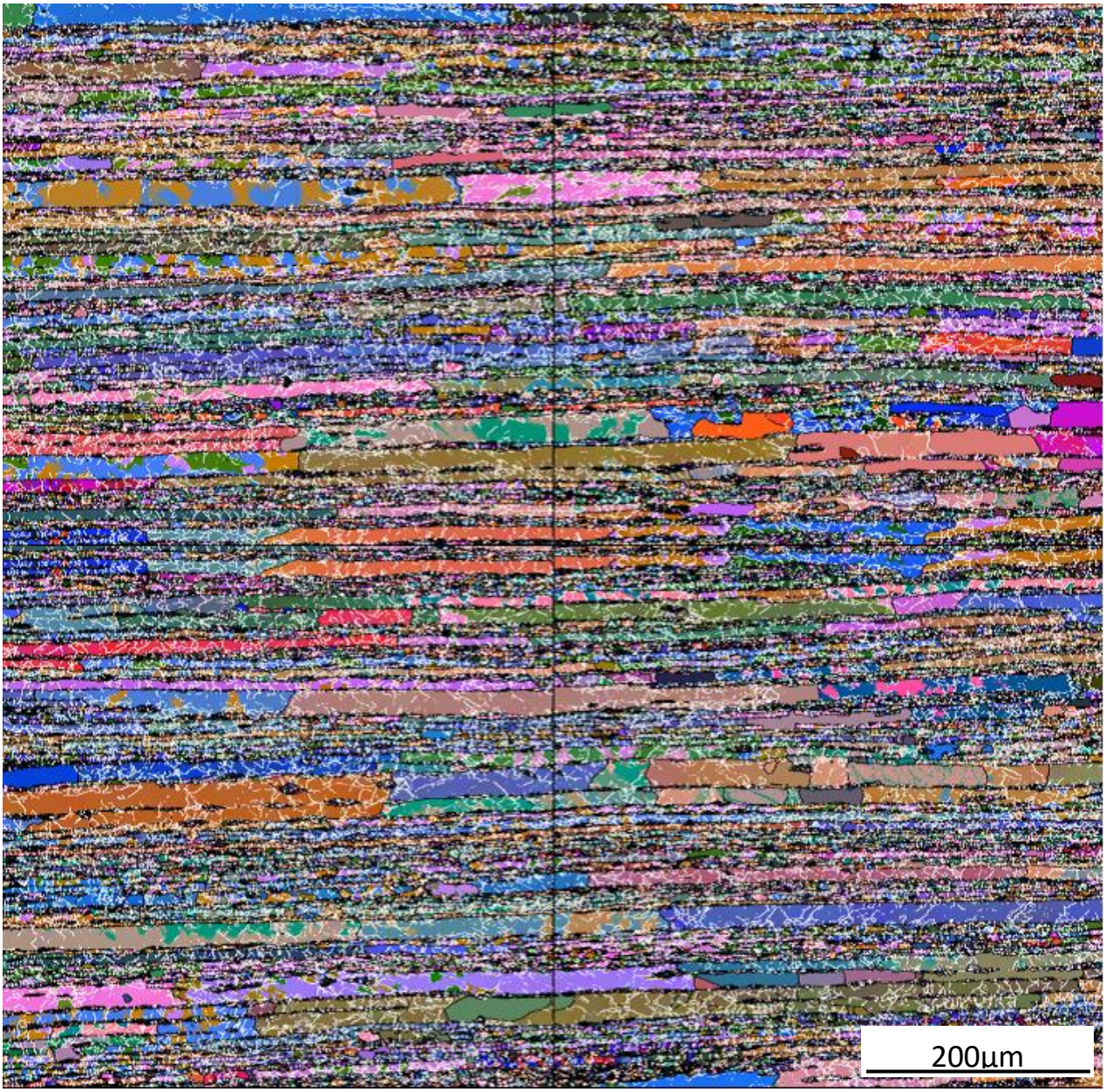

Figure C. 1: EBSD Euler map of heat A deformed at third pass strain rate of $40s^{-1}$ and continuous phase transformation annealing heat treatment at 700˚C for 15 minutes.

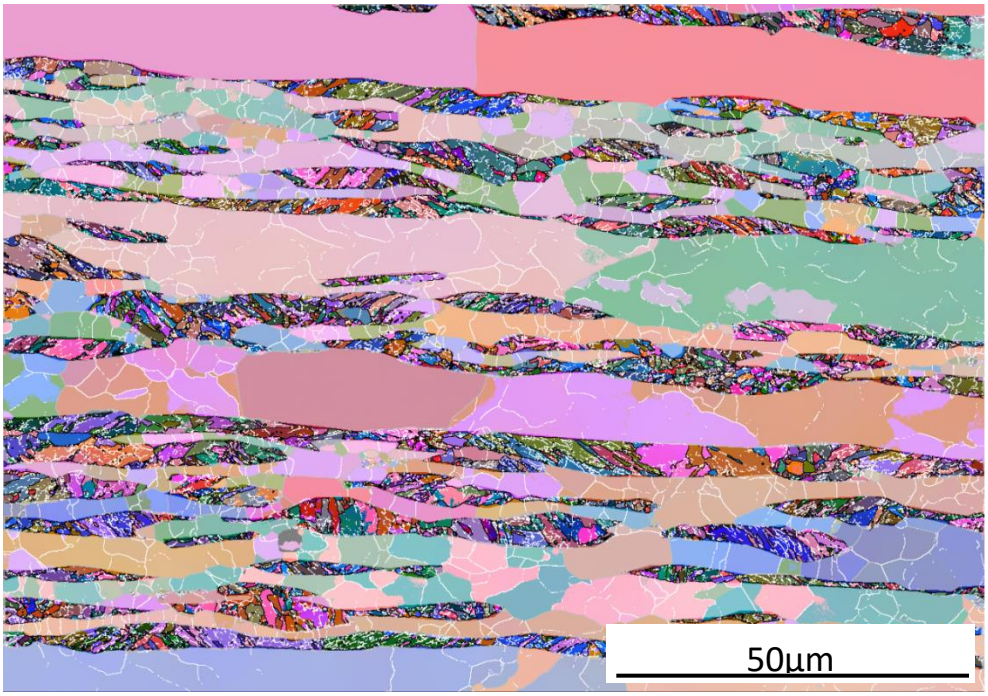

Figure C.2 EBSD Euler map of heat A deformed at third pass strain rate of $40s^{-1}$ and continuous phase transformation annealing heat treatment at 700˚C for 15 minutes.

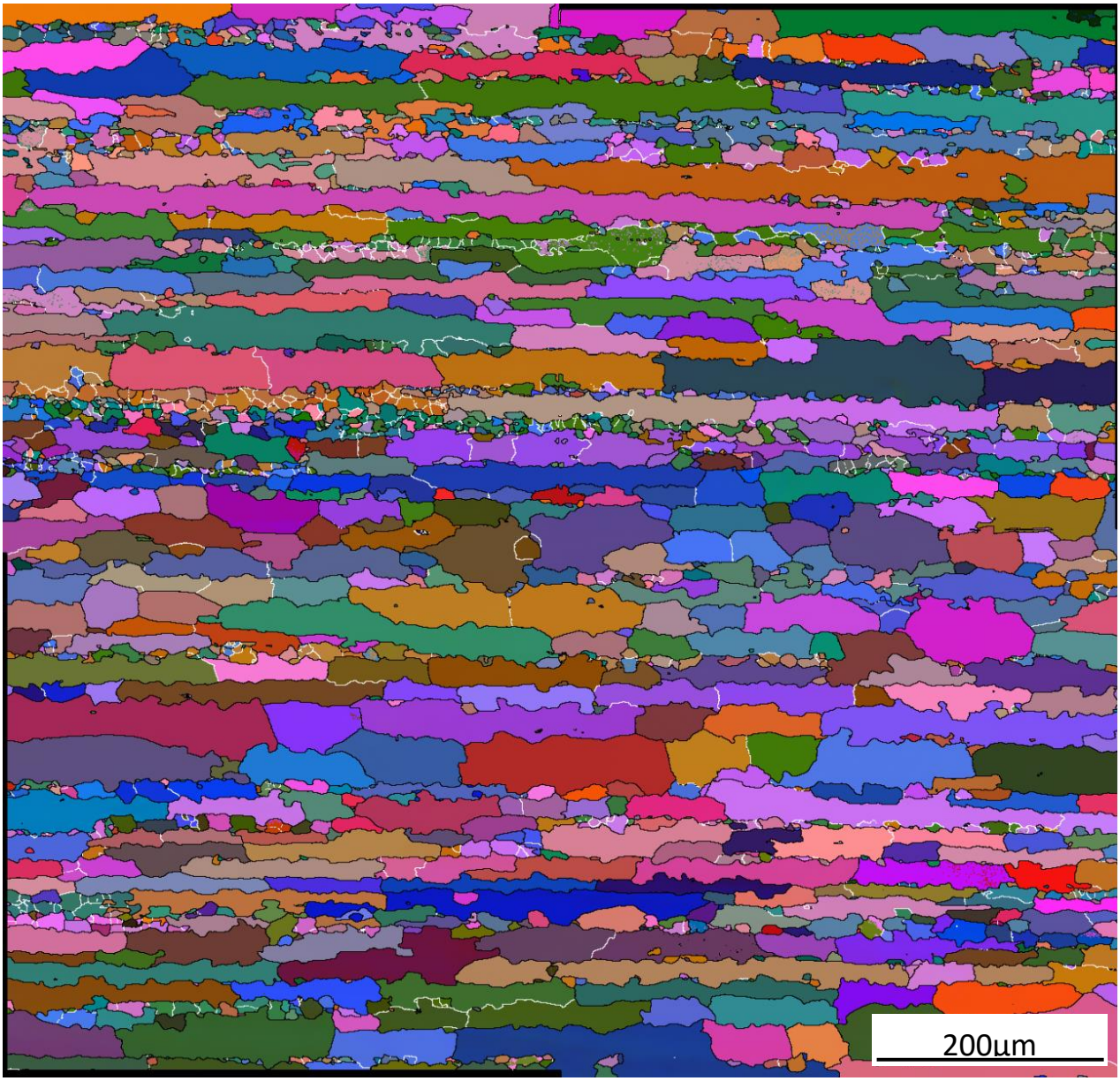

Figure C.3: EBSD Euler map of heat A deformed at third pass strain rate of $40s^{-1}$ and continuous phase transformation annealing heat treatment at 700˚C for 30 minutes

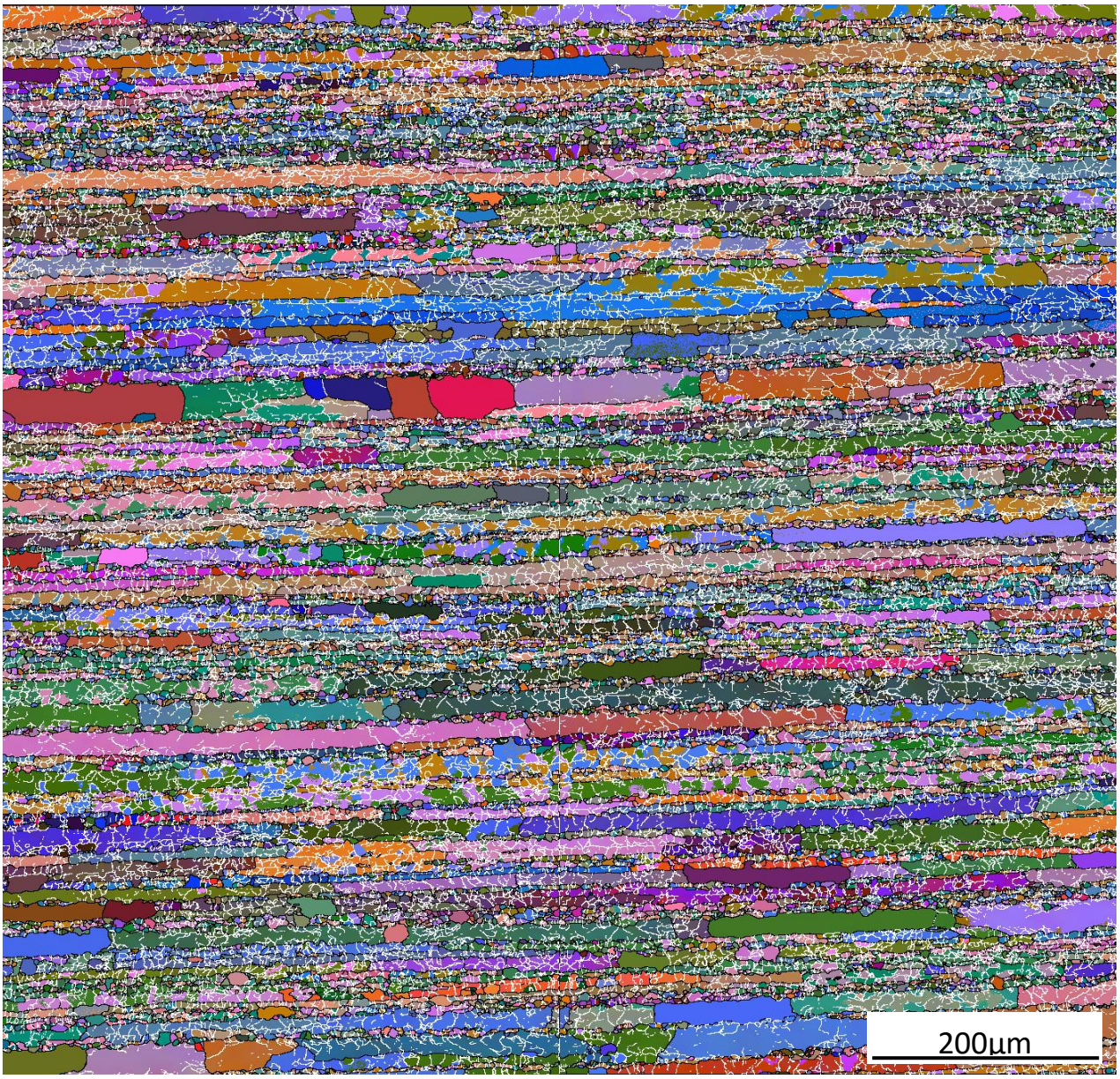

Figure C.4: EBSD Euler map of heat A deformed at third pass strain rate of $40s^{-1}$ and continuous phase transformation annealing heat treatment at 800˚C for 15 minutes.

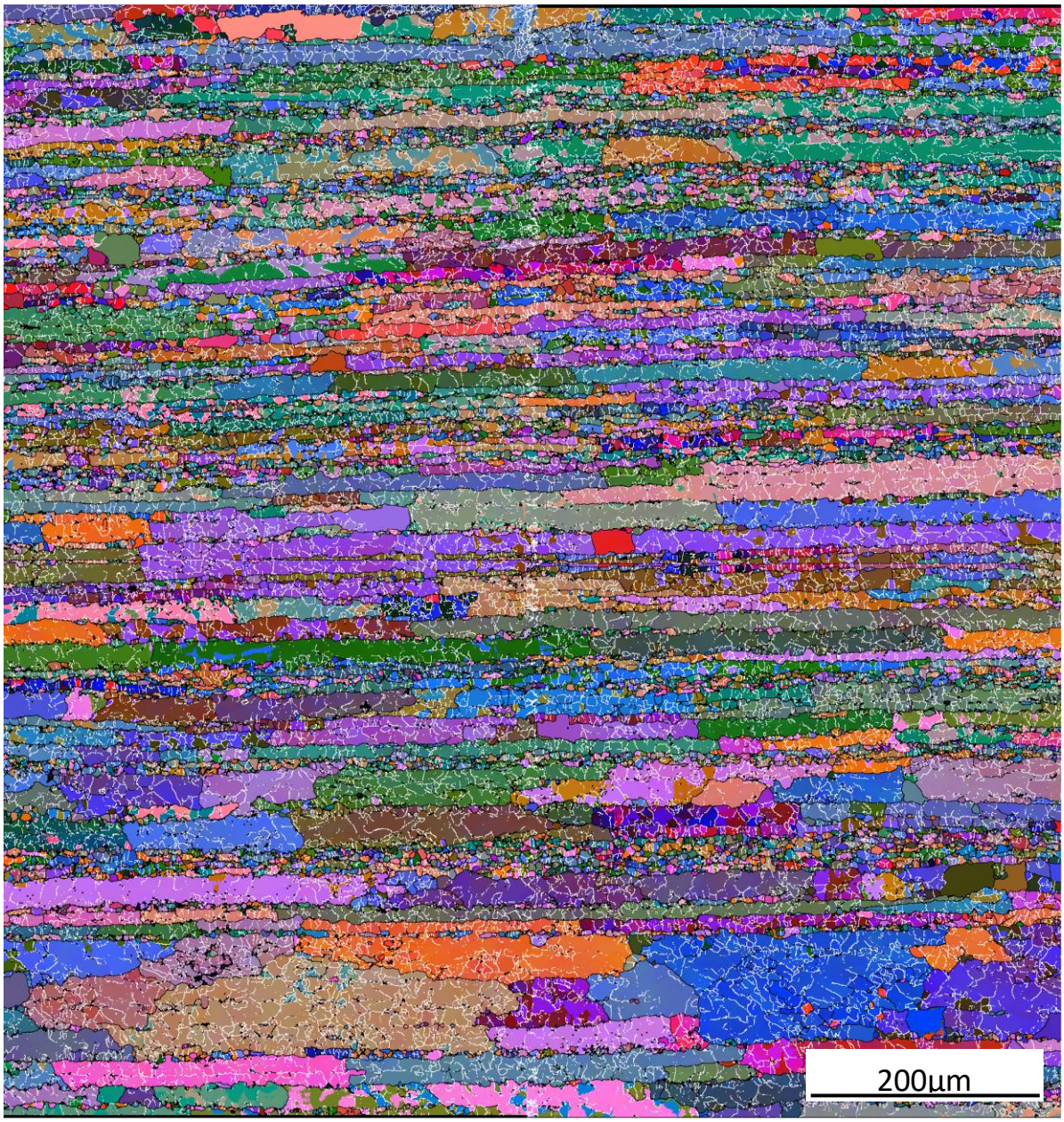

Figure C.5: EBSD Euler map of heat A deformed at third pass strain rate of $40s^{-1}$ and continuous phase transformation annealing heat treatment at 800˚C for 30 minutes.

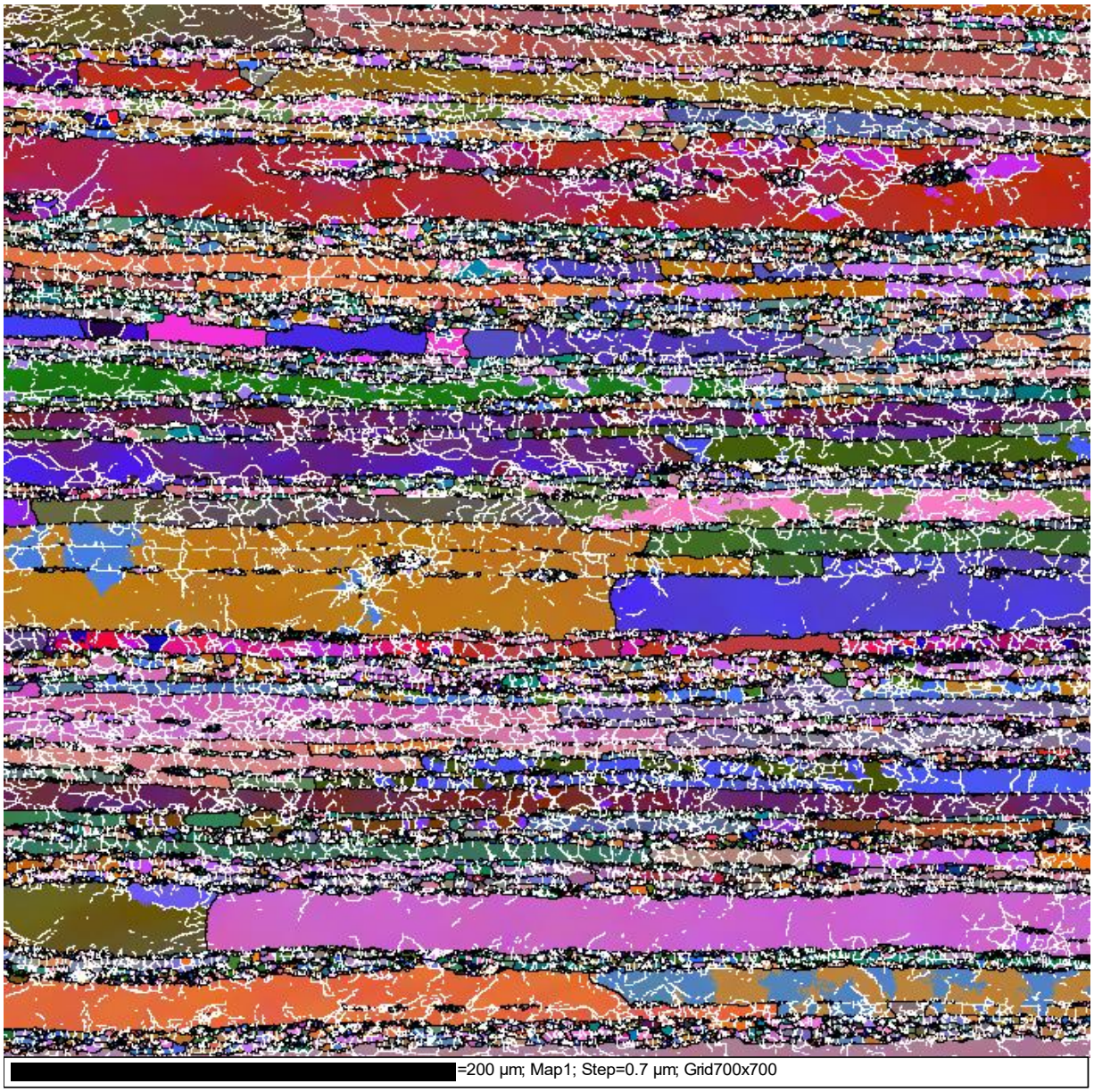

Figure C.6: EBSD Euler map of heat A deformed at third pass strain rate of $80s^{-1}$ and continuous phase transformation annealing heat treatment at 700˚C for 15 minutes.

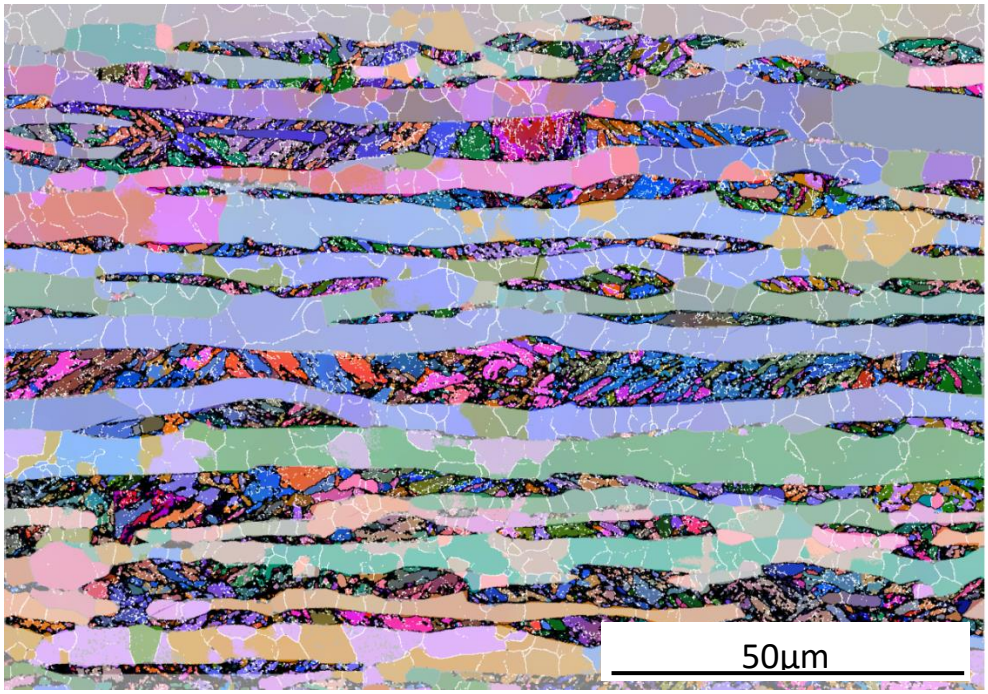

Figure C.7: EBSD Euler map of heat A deformed at third pass strain rate of $80s^{-1}$ and continuous phase transformation annealing heat treatment at 700˚C for15 minutes.

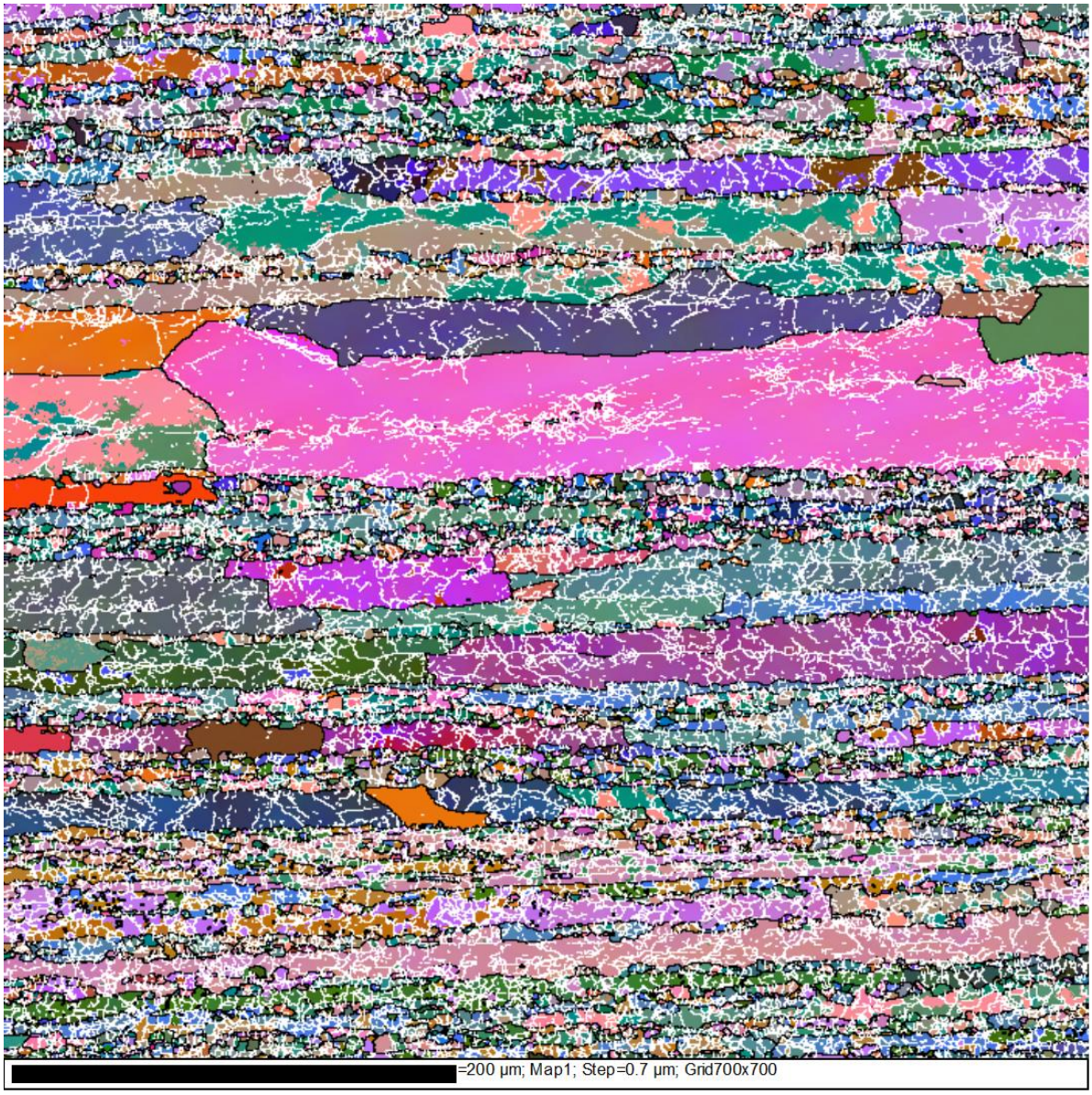

Figure C.8: EBSD Euler map of heat A deformed at third pass strain rate of $80s^{-1}$ and continuous phase transformation annealing heat treatment at 700˚C for 30 minutes.

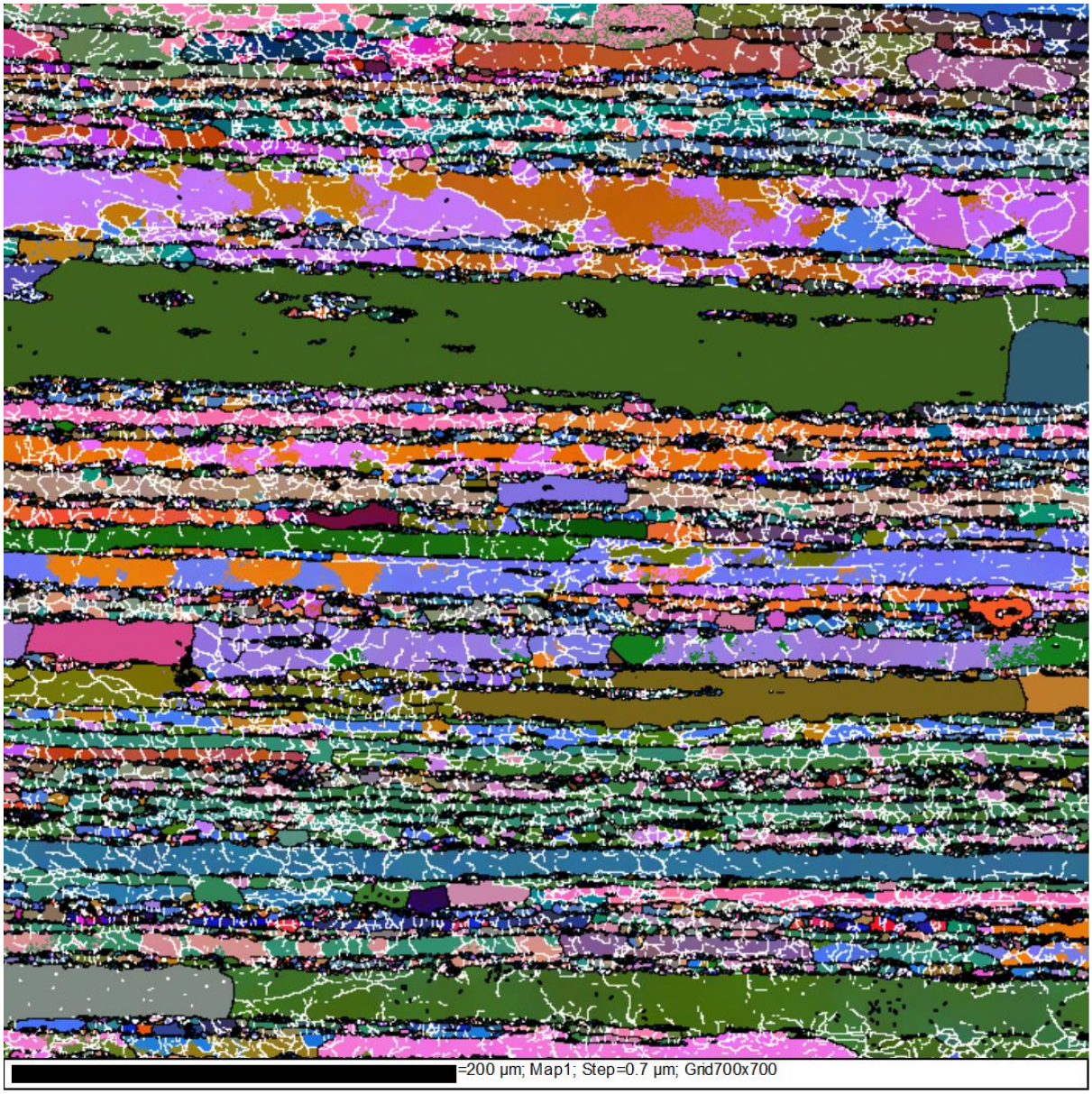

Figure C.9: EBSD Euler map of heat A deformed at third pass strain rate of $80s^{-1}$ and continuous phase transformation annealing heat treatment at 800˚C for 15 minutes.

Figure C.10: EBSD Euler map of heat A deformed at third pass strain rate of $80s^{-1}$ and continuous phase transformation annealing heat treatment at 800˚C for 15 minutes.

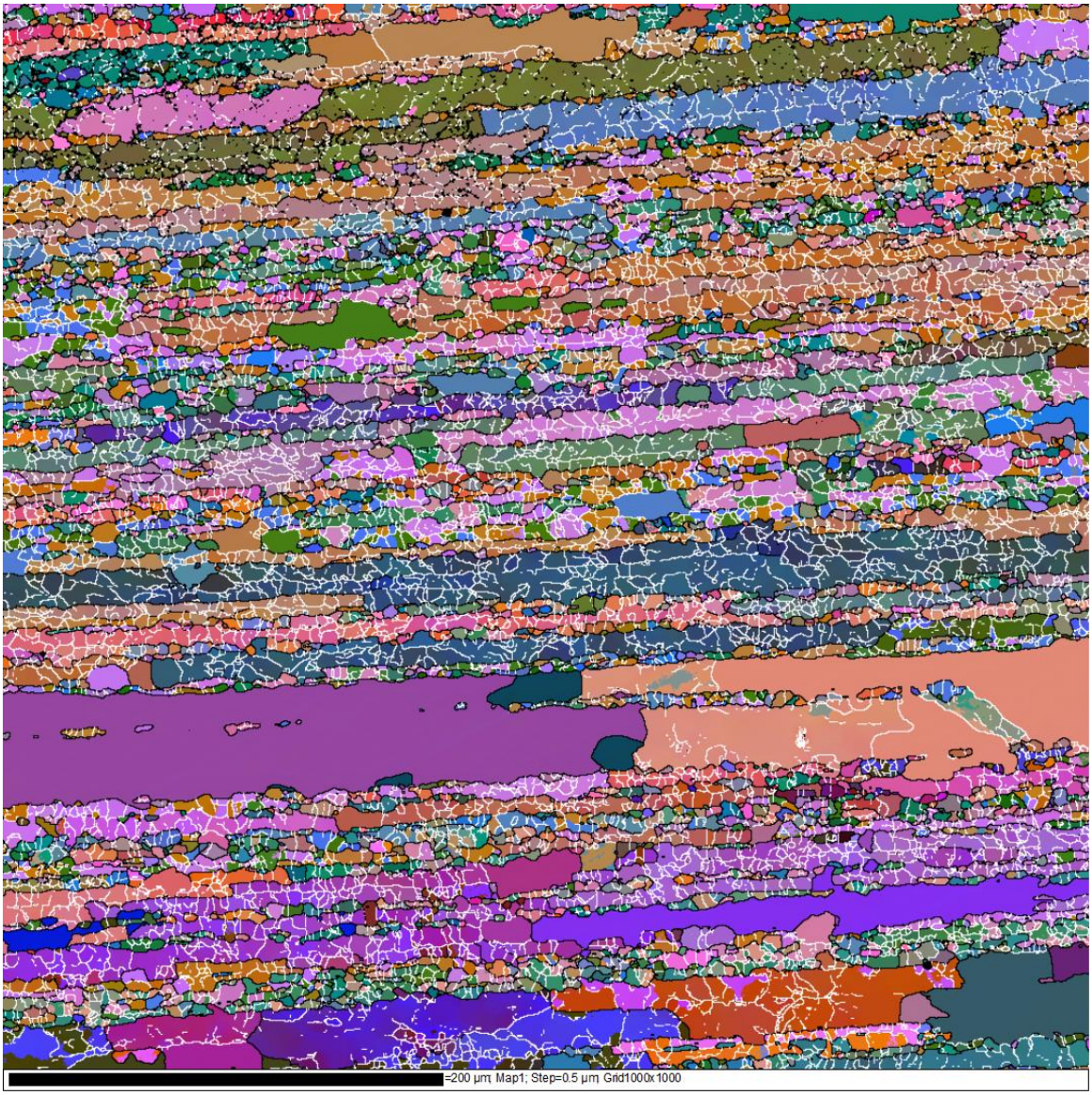

Figure C.11: EBSD Euler map of heat A deformed at third pass strain rate of $80s^{-1}$ and continuous phase transformation annealing heat treatment at 800˚C for 30 minutes.

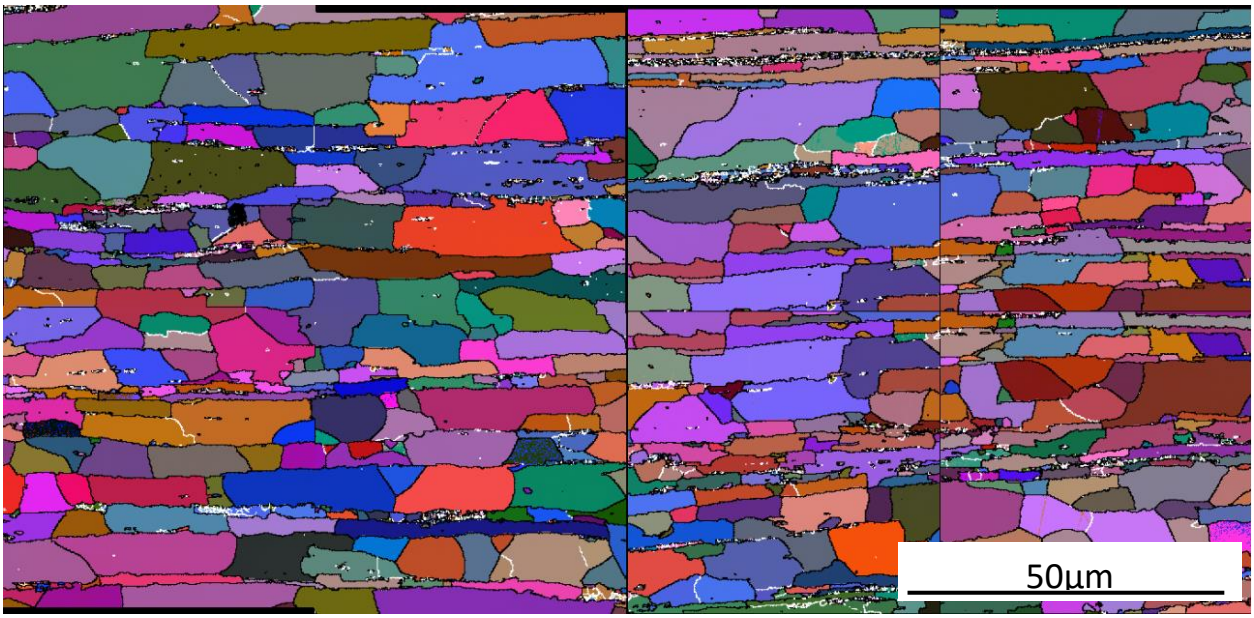

Figure C.12: EBSD Euler map of heat B deformed at third pass strain rate of $80s^{-1}$ and continuous phase transformation annealing heat treatment at 700˚C for 15minutes.

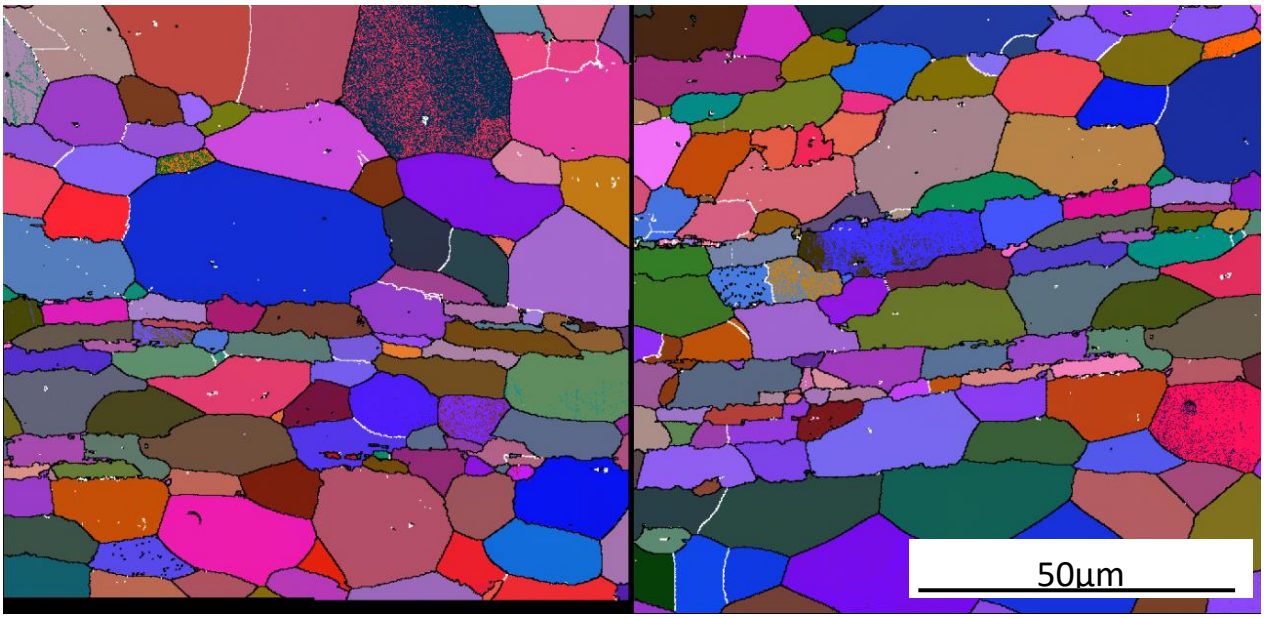

Figure C.13: : EBSD Euler map of heat B deformed at third pass strain rate of $80s^{-1}$ and continuous phase transformation annealing heat treatment at 700˚C for 30 minutes.

Appendix D: martensite tempering heat treatments

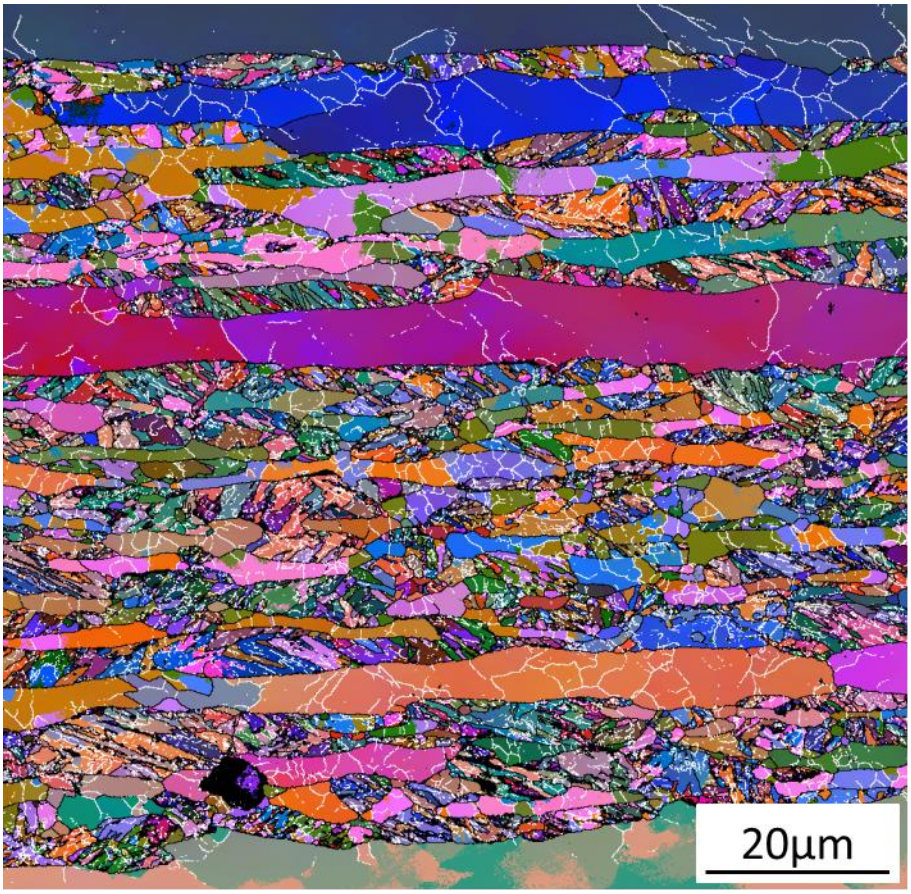

Figure D.0.1: EBSD Euler map of heat A deformed at third pass strain rate of $80s^{-1}$ and martensite tempering heat treatment at 700˚C for 30 minutes.

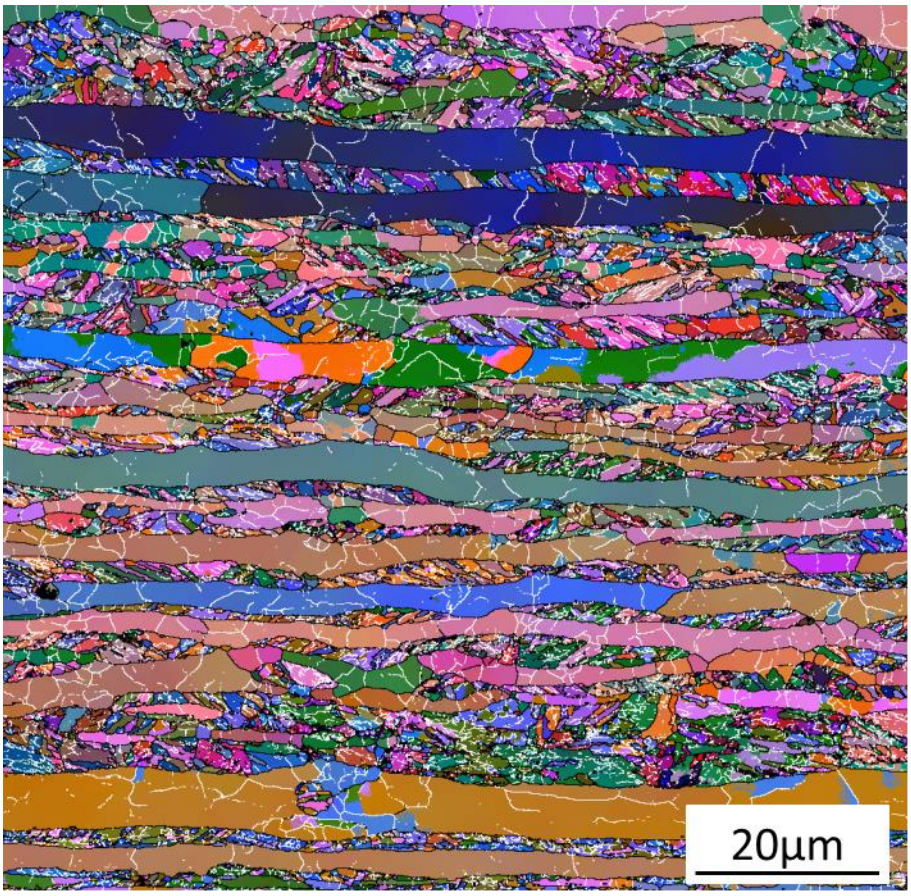

Figure D.0.2: EBSD Euler map of heat A deformed at third pass strain rate of $80s^{-1}$ and martensite tempering heat treatment at 700˚C for 60 minutes.

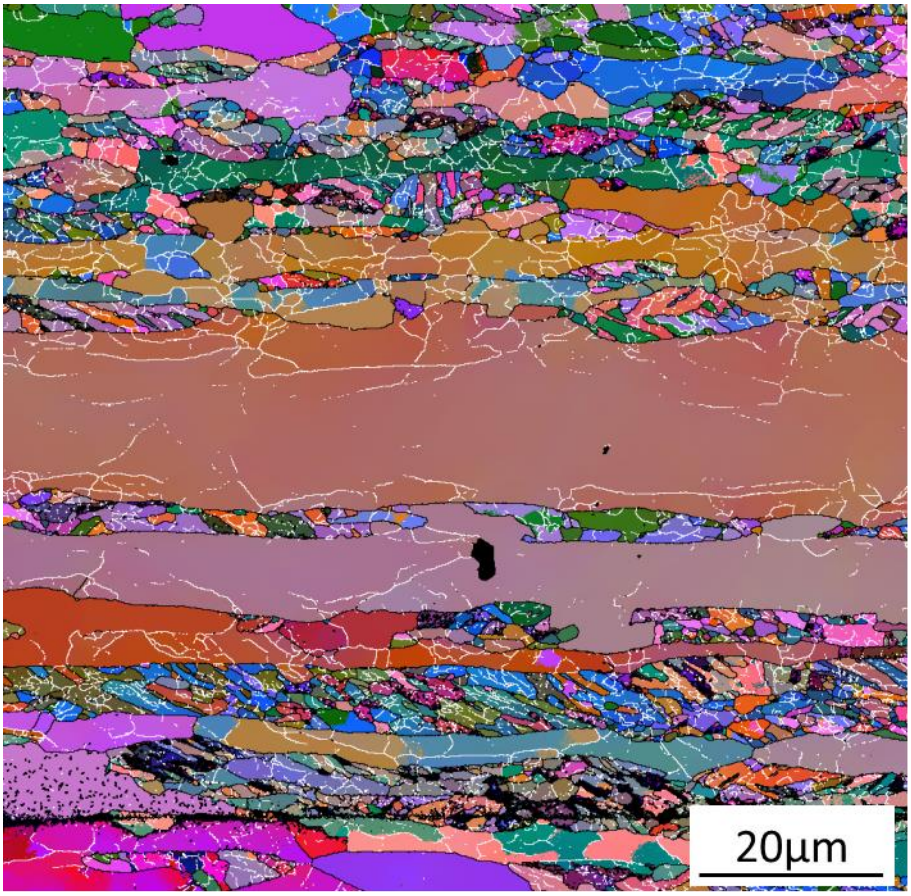

Figure D.0.3: EBSD Euler map of heat A deformed at third pass strain rate of $80s^{-1}$ and martensite tempering heat treatment at 800˚C for 30 minutes.

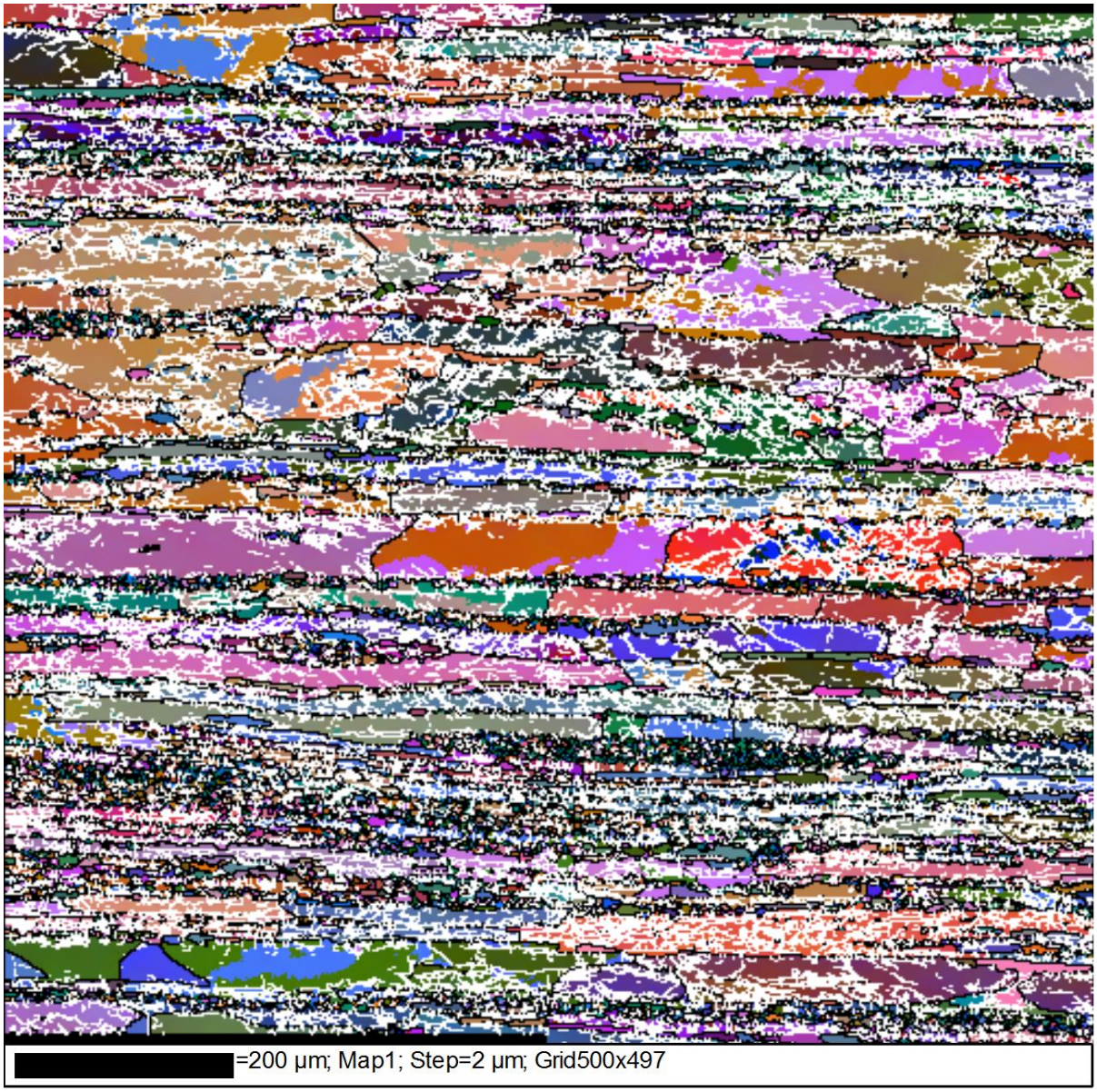

Figure D.0.4: EBSD Euler map of heat A deformed at third pass strain rate of $80s^{-1}$ and martensite tempering heat treatment at 800˚C for 30 minutes.

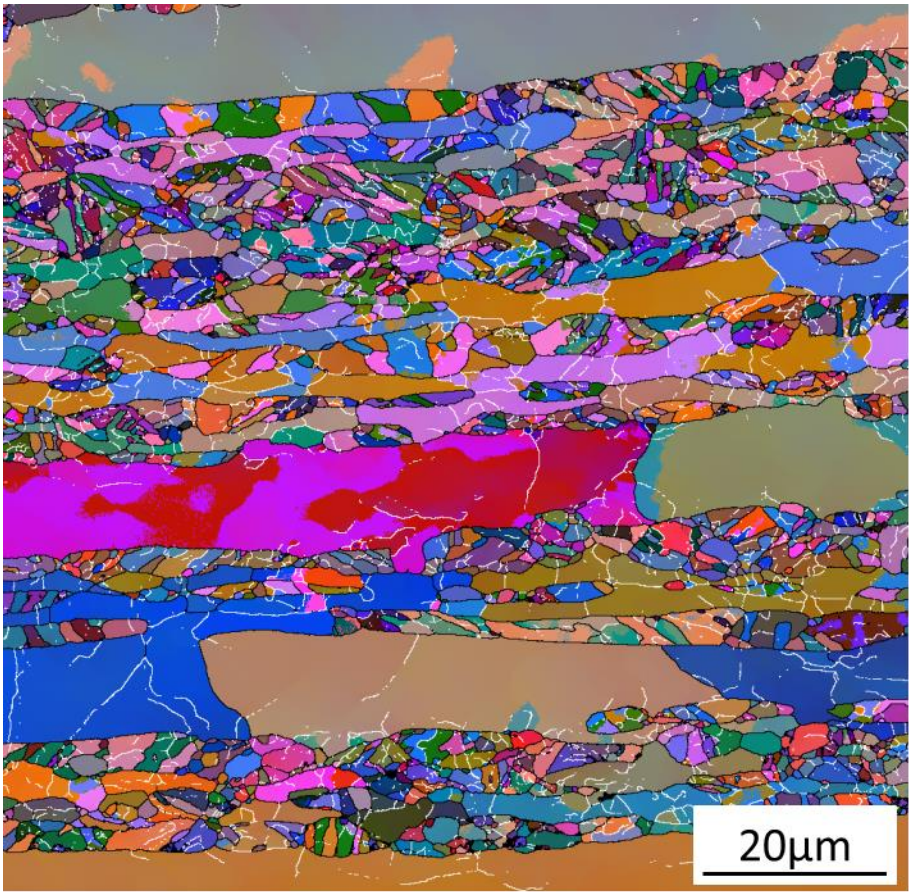

Figure D.0.5: EBSD Euler map of heat A deformed at third pass strain rate of $80s^{-1}$ and martensite tempering heat treatment at 800˚C for 60 minutes.

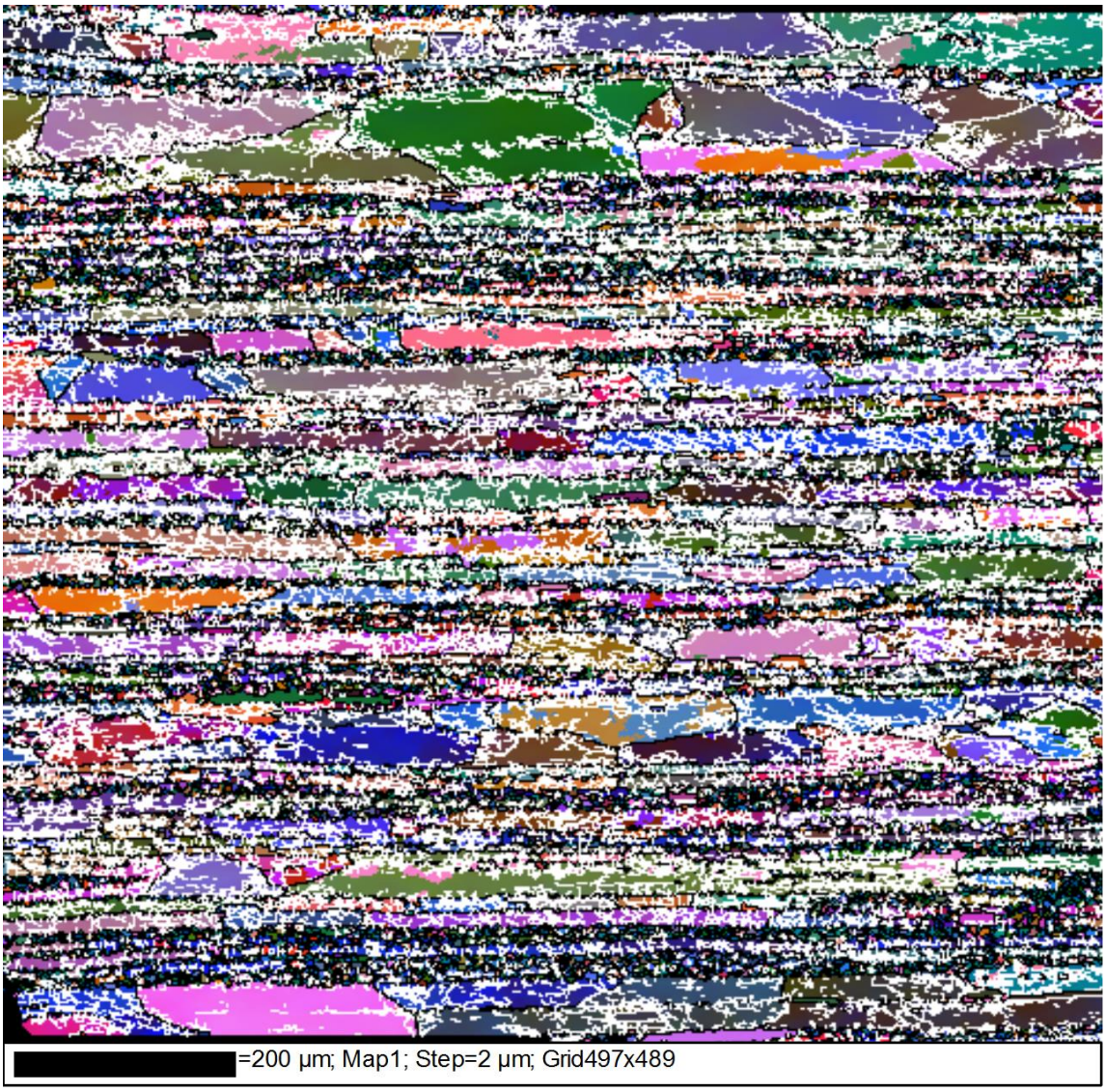

Figure D.0.6: EBSD Euler map of heat A deformed at third pass strain rate of $80s^{-1}$ and martensite tempering heat treatment at 800˚C for 60 minutes.